SEISMIC ATTRIBUTES AND PETROPHYSICAL MODELLING OF THE ARADEIBA-D MEMBER, MUGLAD RIFT BASIN, SUDAN

BY

MIGDAD EL-KHEIR SHUAIB

A Thesis Presented to the
DEANSHIP OF GRADUATE STUDIES

KING FAHD UNIVERSITY OF PETROLEUM & MINERALS

DHAHRAN, SAUDI ARABIA

In Partial Fulfillment of the
Requirements for the Degree of

MASTER OF SCIENCE

In

GEOPHYSICS

May, 2013

KING FAHD UNIVERSITY OF PETROLEUM & MINERALS

DHAHRAN- 31261, SAUDI ARABIA

DEANSHIP OF GRADUATE STUDIES

This thesis, written by **MIGDAD EL-KHEIR SHUAIB** under the direction of his thesis advisor and approved by his Thesis Committee, has been presented and accepted by the Dean of Graduate Studies, in partial fulfillment of the requirements for the degree of **MASTER OF SCIENCE IN GEOPHYSICS**.

8/5/13

Dr. Gabor Korvin
(Advisor)

Dr. Abdulaziz Al-Shaibani
Department Chairman

may 8, 2013

Dr. Osman M. Abdullatif
(Member)

Dr. Salam A. Zummo
Dean of Graduate Studies

May 08, 2013

Dr. Sanlinn Ismail Kaka
(Member)

19/5/13

Date

ACKNOWLEDGMENTS

Acknowledgments are due to King Fahd University of Petroleum and Minerals for supporting this research and Ministry of Petroleum-Republic of Sudan for permission to publish this thesis. Data center manager Dr. Mohammed Al Amin, Mr. Mohammed Adam and their staff, and Mr. Mohammed Kabashi, senior geophysicist in BPC are all acknowledged for providing data and support.

I wish to express my appreciation to Professor Gabor Korvin for his supervision and for his critical review of the manuscript. Thanks are also due to other thesis committee members Dr. Osman M. Abdullatif and Dr. Sanlinn Ismail Kaka for their guidance and help. Also, thanks and appreciations are due to Dr. Aldo Vesnaver for his help.

I would also like to express my sincere gratitude to the Department of Earth Sciences faculty members and staff for their support, assistance, teaching, and guidance during my studies.

Of these, the names of my friends Hassan A. Altom, Mohammed A. Yassin, and Ammar Adam have to be mentioned for their assistance and help. Acknowledgements are extended to my Sudanese friends at King Fahd University of Petroleum and Minerals.

Word of appreciation and gratitude is due to my mother, wife, brothers and sisters for their great moral support, help, and prayers.

Above all, my greatest gratitude is due to Allah for granting me the patience and knowledge to successfully pass through this stage of my academic career.

TABLE OF CONTENTS

LIST OF TABLES

LIST OF FIGURES

LIST OF ABBREVIATIONS

ANN	:	Artificial Neural Network
PSTM	:	Post Stack Time Migration
RLA5	:	Deep Laterolog
RLA3	:	Shallow Laterolog
RXOZ	:	Micro-Laterolog
DT	:	Acoustic Log
RHOZ	:	Density Log
NPHI	:	Neutron Log
GR	:	Natural Gamma Ray Log
SP	:	Spontaneous Potential
HCAL	:	Caliper Log
GRAS	:	The Geological Research Authority of the Sudan
CASZ	:	The Central African Shear Zone
CEC	:	Cation Exchange Capacity
CNPC	:	China National Petroleum Company
CNL	:	Compensated Neutron Log
Vsh	:	Shale Volume
Sw	:	Water Saturation

ABSTRACT

Full Name : Migdad El-Kheir Shuaib

Thesis Title : Seismic Attributes and Petrophysical Modeling of the Aradeiba-D Member, Muglad Rift Basin, Sudan

Major Field : Geophysics

Date of Degree : May 2013

The Aradeiba Formation of Muglad basin, Sudan, attains a major significance for providing seal to stratigraphic and structural traps of mudstone in the Upper Cretaceous in the area. Aradeiba Formation is also a major oil bearing sandstone reservoir in the Muglad rift basin of interior Sudan. Oil in Aradeiba Formation is mainly in Aradeiba-D. Heterogeneity and geometry of sandstone bodies and the siltstone/mudstone units vary more within Aradeiba due to changes in depositional environment from lacustrine facies to fluvio-deltaic facies.

In the study I derived lithological and petrophysical reservoir models of the Aradeiba-D member to enhance the reservoir description and characterization of the reservoir between sparse well data, and improved the integration process to predict and map the less understood reservoir rock properties using a multidisciplinary approach involving geostatistical and seismic attributes analysis through the application of multi-variate regression analysis.

Integrated methods used to calculate the petrophysical parameters included shale volume from different shale indicator tools, porosity determined from sonic, density, neutron combinations, permeability estimated from core-derived relationships, and the "Indonesia" equation used to calculate water saturation. Artificial Neural Networks

provide powerful tools for facies classification which was applied on the basis of gamma ray, sonic, neutron porosity, bulk density, and deep resistivity logs.

After obtaining the digital logs for lithology, porosity, permeability and water saturation and establishing proper well-to-seismic tie, the attributes which had been defined as sample-based transforms of the seismic data were visually examined to select the best candidates for multivariate regression. Based on the stepwise linear regression and cross validation error analysis the best number of attributes and length of the convolutional operator were chosen. The whole process is applied to a targeted time window. The derived transforms were then applied to the 3-D seismic volume. For each model from the four two cross sections across the model have been created which correspond to the in-line 253 and x-line 232 and intersects the X-9 and X-1 wells. The resulting final time sections, time slices and cubes provide a geologically realistic facies and petrophysical distribution and help in understanding the subsurface image.

According to the logging and multi-attributes results, the sand bodies of Aradeiba-D reservoir are of small size, we can explain the sand body relation and define the boundary of sand bodies based on the result of multi-attributes analysis which suggests a composite of single sand bodies. The total sand-thickness is small, the thickest part achieves nearly 20 meters, average thickness is about 7 meters, it is distributed as belts from Northwest to Southeast.

ملخص الرسالة

الاسم الكامل: **مقداد الخير شعيب محمد**

عنوان الرسالة: السمات السيزمية والنمذجة البتروفيزيائية لعضو عرديبة - د الرسوبي، حوض المجلد الأخدودي، السودان

التخصص: جيوفيزياء

تاريخ الدرجة العلمية: : مايو ٢٠١٣م

يعتبر تكوين عرديبه - حوض المجلد – السودان ذا اهمية كبيره لتوفيره لسد ومصائد تركيبية طبقية نفطية والذي يتكون غالبا من الحجر الطيني من العمر الطبشيري العلوي. و يعتبر ايضا تكوين عرديبه خزان رملي رئيسي حاوي للنفط في حوض المجلد المتصدع حيث يتواجد النفط في العضو عرديبه – د. هنالك عدم تجانس واختلاف كبير في ابعاد اجسام الحجر الرملي ووحدات الحجر الطيني/الغريني داخل تكوين عرديبه بسبب التغيرات في البيئات الترسيبية من نهرية الي دلتية.

من خلال الدراسة تم اشتقاق نماذج صخرية وبتروفيزائية لخزان العضو عرديبه – د لتحسين وصف الخزان بين معلومات الآبار المتفرقة وتحسين عملية تكامل المعلومات للتنبؤ ورسم خرائط لخصائص صخور المكمن بإستخدام نهج متعدد التخصصات الذي تتضمن تحاليل جيوإحصائية والسمات السيزمية من خلال تطبيق تحليل الإنحدار متعدد المتغيرات.

تم استخدام طرق تكاملية لحساب الخصائص البتروفيزيائية التي تشمل (أ) حجم الطين بإستخدام قراءات ادوات سبر مختلفة تعتبر مؤشر للطين، (ب) المسامية من التسجيلات الصوتية ، والكثافه ، والنيترون،(ج) النفاذية من العلاقات المستنتجة من تحليل صخور المكمن، و(د) التشبع المائي الذي تم حسابه بإستخدام معادلة "إندونيسيا". يعتبر الذكاء الإصطناعي اداه قوية لتصنيف السحنات الصخرية والذي تم استخدامه علي اساس قياسات اشعه جاما، القياسات الصوتية، وقياسات مسامية النيترون، وقياسات الكثافة الظاهرية وقياسات المقاومية العميقة.

بعد الحصول علي التسجيلات في صوره رقمية لتصنيف السحنات، المسامية، النفاذية، والتشبع المائي وربط الآبار بالمعلومات السيزمية تم تعريف السمات السيزمية المستنده علي التحويلات عينه بعينه وفحصها بصريا لتحديد افضل المرشحين في عمليه تحليل الإنحدار متعدد المتغيرات. استنادا علي الإنحدار الخطي التدريجي و تحليل خطأ التحقق

من الصحة تم اختيار افضل عدد من السمات وطول مشغل الإلتفاف. تم تطبيق العلاقات المستنتجة من عملية تحليل الإنحدار متعدد المتغيرات في المعلومات السيزمية ثلاثية الأبعاد. حيث تم عمل قطاعين لكل نموذج من النماذج الأربعه واللذين يتوافقان مع خط ٢٥٣ (شمال شرق – جنوب غرب) وخط ٢٣٢ (شمال غرب – جنوب شرق) وتتقاطع مع الأبار X-9 و X-1 . وتوفر القطاعات الناتجة النهائية والشرائح الزمنيه والنماذج ثلاثية الأبعاد توزيعات حقيقية للسحنات الرسوبيه والبتروفيزيائية وتساعد في فهم الصوره التحت سطحية.

وفقا لنتائج السبر البئري والسمات السيزمية تعتبر اجسام الحجر الرملي لخزان عرديبه – د صغيره الحجم ويمكن تحديد ابعادها وحدودها حيث وجد أن السمك الكلي للحجر الرملي صغير ، والجزء الأكثر سمكا يمكن ان يصل الي حوالي 20 متر ومتوسط السمك حوالي 7 امتار و يتوزع في شكل احزمه متخذه اتجاه الشمال الغربي الي الجنوب الشرقي.

CHAPTER 1

INTRODUCTION

1.1 Introduction

Muglad rift basin in Sudan which is regionally linked to the Central African Rift System and located in Darfur province - south Sudan, (Figure 1.1). It strikes NW-SE and occupies an area greater than 11×10^4 km^2 and is considered as one of the major oil basins in Sudan.

The basin contains a thick interbedded sequence of claystone and sandstone above the basement which is deposited in three rifting phases, each phase composed of lacustrine facies at the bottom, fluvial and fluvio-deltaic facies at the top. The source rock is the lower part of Abu Gabra Formation which is characterized by deep lacustrine shale of early Cretaceous. The reservoir rock belongs to the first rifting phase characterized by braided-stream sandstones of the Bentiu Formation. The top seal is the mudstone of Aradeiba Formation in the Upper Cretaceous (Schull, 1988).

Aradeiba Formation is also a major oil bearing sandstone reservoir in the Muglad rift basin of interior Sudan. Oil in Aradeiba Formation is mainly in Aradeiba- D Member which is the interval of interest in this study.

In this study I attempt to derive and develop geological and petrophysical reservoir models of Aradeiba-D Member to enhance the reservoir description and characterization of the reservoir between sparse well data and improve the integration process to predict and map the less understood reservoir rock properties using multidisciplinary approach involving geostatistical, artificial intelligence, and seismic attributes analysis through the application of multi-variate regression analysis (linear mode), Hampson et al. (2001).

Moreover, this study may help in improving reservoir management strategies, and consequently maximize hydrocarbon recovery and added profits. In addition it is expected to provide a detailed (high-resolution) geological and petrophysical model that integrates various types of data for efficient development and production of the field.

The attempt to predict and map the lateral reservoir property changes within the reservoir (porosity, permeability, lithology, reservoir thickness, etc.) by integrating optimally selected seismic attributes with well-log data, i.e., by investigating the relationships between multiple seismic parameters (or attributes) and reservoir properties at all well locations is an important factor in the development of the hydrocarbon reservoirs.

These types of reservoir studies generally use 3-D seismic parameters as their secondary source of data, and geological and/or petrophysical parameters as their primary source of data honoring the true values at well locations. One utilizes the relationships between different properties to "predict" or estimate the log property at all locations of the seismic volume.

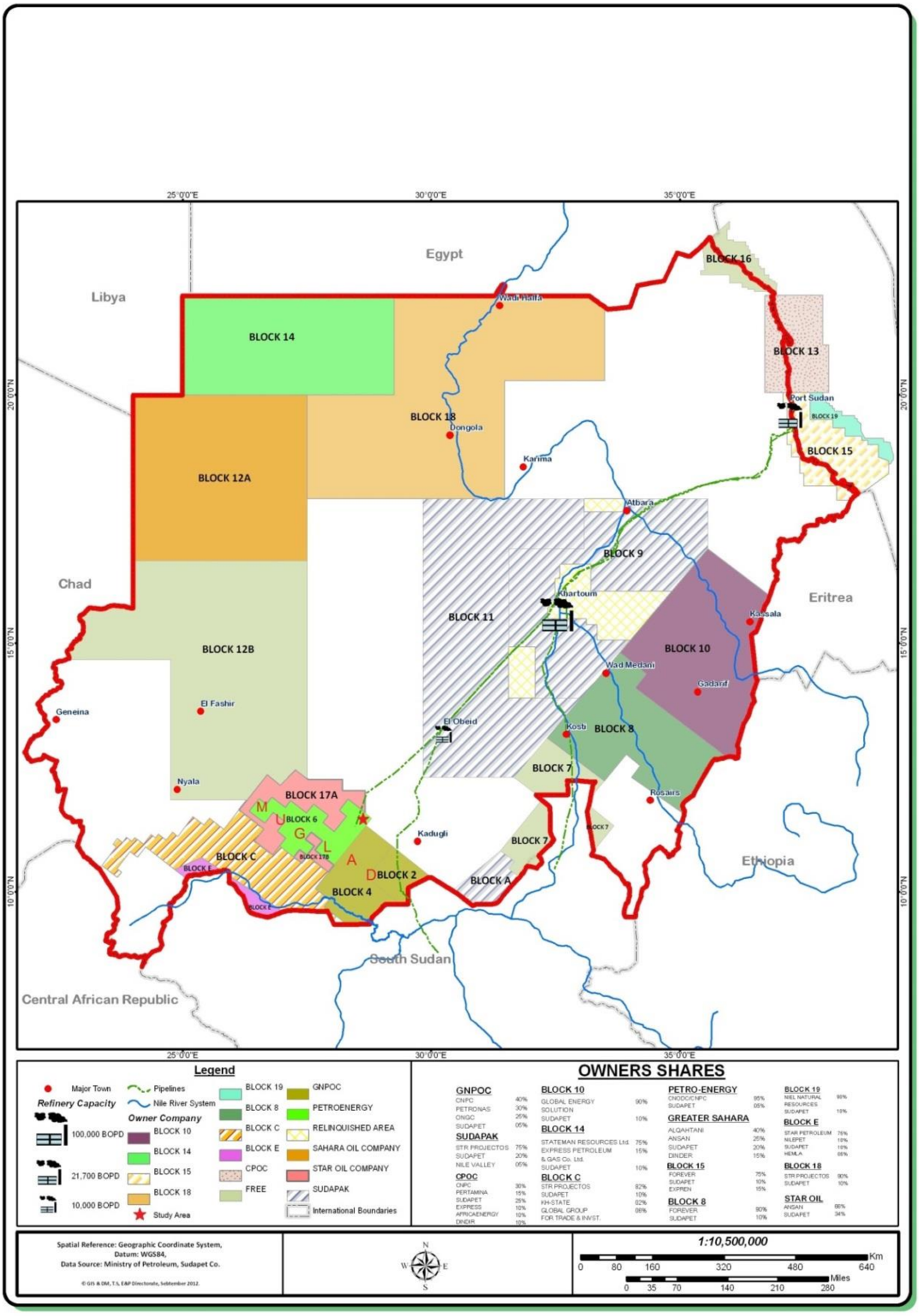

Figure 1.1 Location of the study area in Muglad rift basin (Sudapet Co., 2012)

1.2 The Study Area

The Muglad basin is a rift related basin located in Darfur Province - south Sudan, striking NW-SE which occupies an area greater than 11×10^4 km^2. The Muglad basin is regionally linked to the Central African Rift System (Schull, 1988).The basin is divided into several blocks, block 6 in the north and block 1, 2, 4 in the southern part of the basin, (Figure 1.1).

The northern part of the basin (block 6) is structurally subdivided into several sub-basins, (Figure 1.2), one of them is Fula sub-basin which lies in the northeast part which is further subdivided to several sub-basins and generally consists of a Precambrian metamorphosed rock system in the basement covered by sediment strata of Cretaceous, Tertiary and Quaternary age (Schull, 1988).

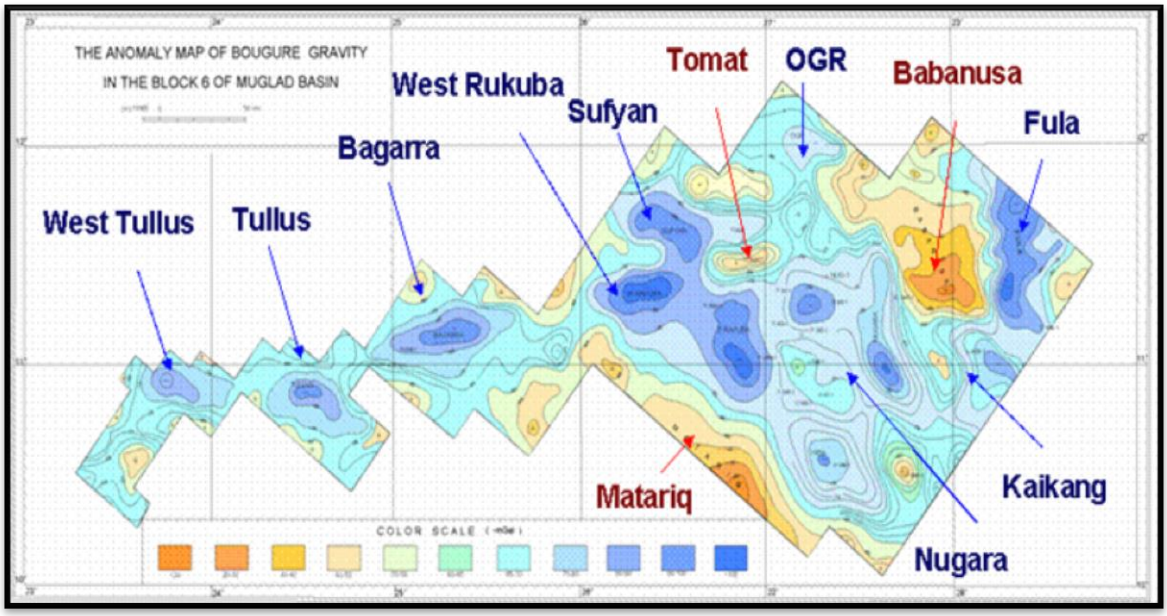

Figure 1.2 Block 6 depressions Bouguer anomaly map located Fula sub basin – Muglad Basin – Sudan (Schull, 1988)

1.3 Problem Statement

The Aradeiba Formation of Muglad basin attains major significance for providing seal to stratigraphy and structural traps in the area. Aradeiba Formation is also a major oil bearing sandstone reservoir in the Muglad rift basin of interior Sudan. The oil in Aradeiba Formation is mainly located in the Aradeiba-D Member.

Heterogeneity and geometries of sandstone bodies and the siltstone/mudstone units show larger variation within Aradeiba due to changes in depositional environment from lacustrine facies to fluvial to fluvio-deltaic facies. Thus, knowing the spatial distribution of petrophysical parameters between wells has an important role for predicting the optimal production possibilities.

In this study I will develop geological and petrophysical reservoir models of Aradeiba-D Member to enhance the reservoir description and characterization of the reservoir between sparse wells and improve the integration process in predicting and mapping reservoir rock properties

I hope that this study will help to improve reservoir developing, management strategies, and consequently maximize hydrocarbon recovery and added profits. In addition, it is expected to provide geological and petrophysical models that integrate various types of data and may provide a better understanding of facies architecture, estimation of geometry of sandstone/shale bodies within the reservoir for efficient development and production of the field.

1.4 Objectives

The main objective for this research is to delineate the spatial distribution of the lithology, porosity, permeability and water saturation of Aradeiba-D Member by integrating different types of geological and geophysical information using multi attribute analysis, artificial intelligence, and geostatistics to get more confident geological and petrophysical models. To achieve this, the following tasks are set out:

1. Estimation of petrophysical parameters (shale content, porosity, permeability, fluid saturation).
2. Characterization of facies types and assign to each facies its petrophysical properties (i.e. make a geological model).
3. Combining well logs (calculated petrophysical parameters) and seismic data for predicting well log properties through the seismic cube by employing multi attribute transforms to predict the rock properties between wells.

1.5 Dataset Description

Data set used in this study, (Figure 1.3), were obtained from the Ministry of Energy, Republic of Sudan, and consist of:

1. Seismic Data: 3D Post Stack Time Migration (PSTM) cropped seismic cube, from the northeast of Fula depression, representing an area of about 40.24 km^2 (4.08 km × 9.86 km) with a bin size of 12.5m × 25.0m and 1-s two-way travel time (TWT) record length.

2. Well Log: 18 wells combined log information which include: deep laterolog (RLA5), shallow laterolog (RLA3), micro-laterolog (RXOZ), acoustic log (DT), density log (RHOZ), neutron log (NPHI), natural gamma ray log (GR), spontaneous potential (SP), caliper log (HCAL).
3. Other Data:
    a) Master Logs and Formation tops.
    b) FulaNE 3D seismic interpretation (Bentiu and Aradeiba-D interpreted horizons).

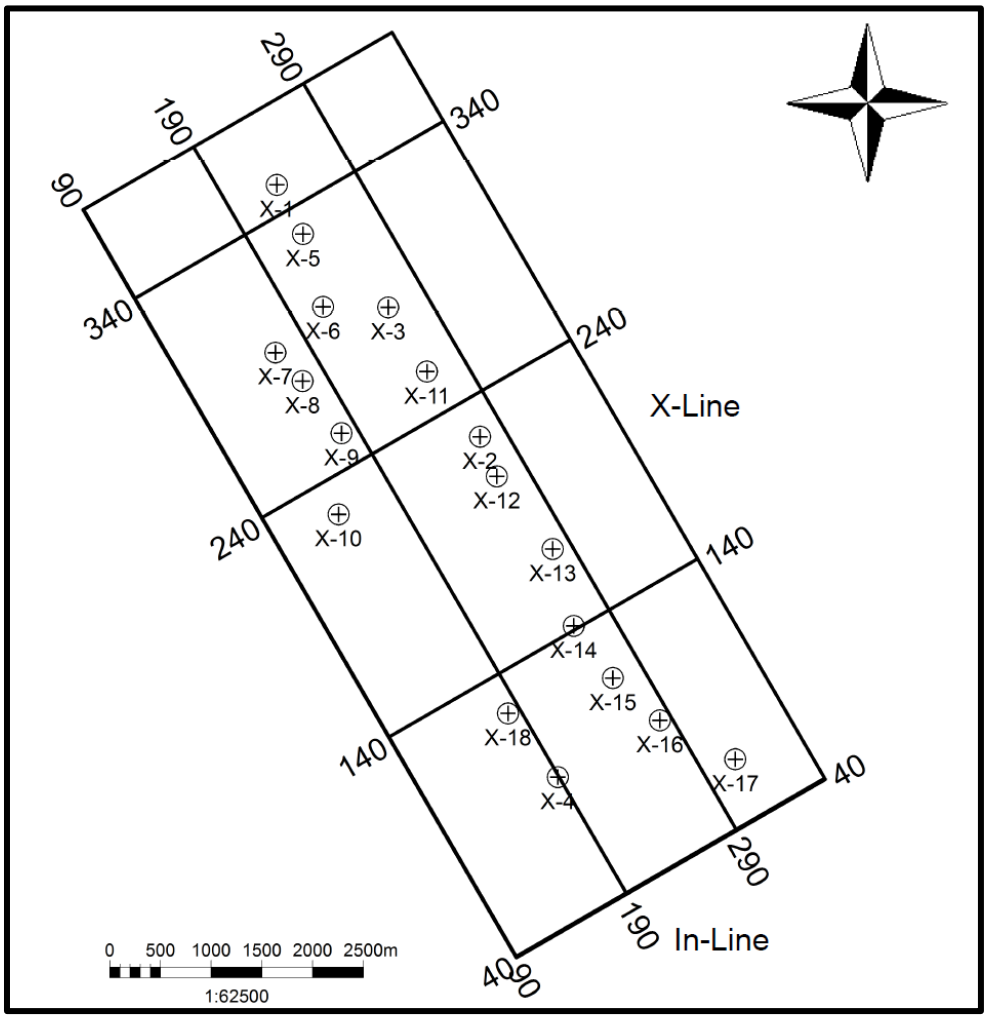

Figure 1.3 Representation of the available data as boreholes location inside the 3D seismic cube

1.6 Methodology

This study includes two main parts: petrophysical/facies analysis, and multi-attribute transforms. A summary of the individual parts is outlined in the flow chart, (Figure 1.4), and discussed in section 1.6.1 and 1.6.2.

1.6.1 Petrophysical and Facies Analysis

The aim of the petrophysical study is to get interpreted petrophysical datasets (porosity, permeability, water saturation logs) for all 18 wells which will be then used as inputs in multi-attribute transforms for modeling. This part was done as follows:

a) Both Larionov (1969) equation which is valid for older rocks, Schlumberger (1987), and the density-neutron method used to determine shale content (Vsh) in Aradeiba-D Member.
b) Porosity obtained based on sonic (DT), neutron (NPHI), density (RHOZ) logs and density-neutron combination.
c) The "Indonesia" equation (because the formation is clayey) used to determine water saturation (Sw).
d) Core analysis results from unpublished reports used to estimate formation permeability.

On the basis of gamma ray (GR), sonic (DT), neutron porosity (NPHI), bulk density (RHOZ), and deep resistivity (RLA5) logs, neural networks were applied for facies classification.

1.6.2 Multi-attribute Transforms

The most popular method is the calculation of seismic attributes which are all extracted information from seismic data, either by direct or indirect measurements, and establishing their correlation with well data.

The general objective for the seismic attributes study is to predict lateral changes in reservoir properties (lithology, porosity, permeability, water saturation) by integrating optimally selected seismic attributes with well-log data, i.e., by investigating the relationships between multiple seismic parameters (or attributes) and reservoir properties at all well locations. To achieve this goal:

a) Well-logs were tied to the seismic and converted from their original depth domain to time domain to match the calibrated seismic traces using sample-based approach.
b) Proper statistical relationships were established, at all well locations, between reservoir parameters and several seismic attributes.
c) The reservoir property was predicted from an established statistical empirical function (data-driven) which combines various seismic attributes through the application of multi-variate regression analysis (linear mode) (Hampson et al., 2001).
d) The reliability of the derived relationship was determined by cross-validation.

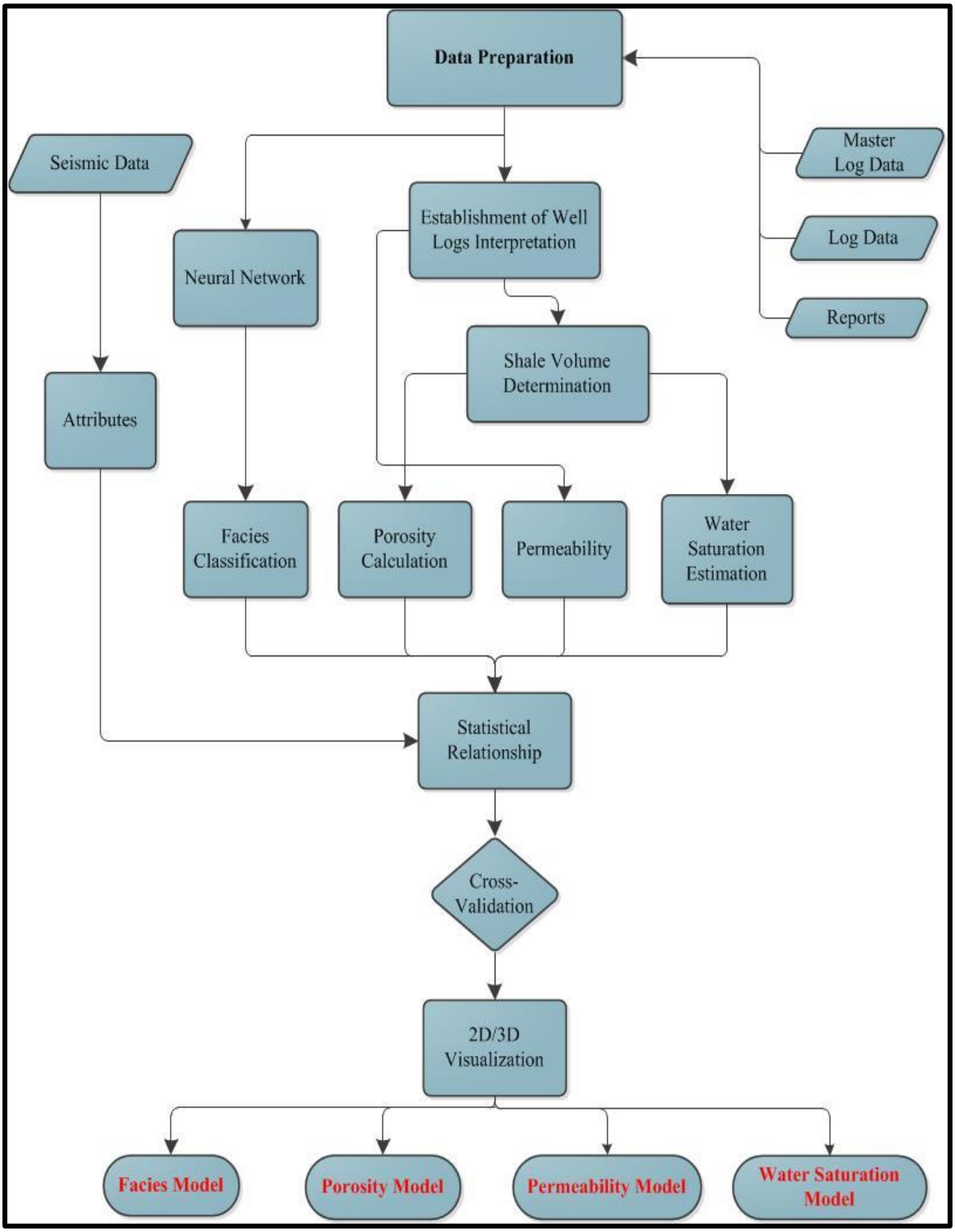

Figure 1.4 Flow chart showing the study procedure and methodology

1.7 Facilities

I used *Hampson*-Russell and *Petrel* software. With the help of Hampson-Russell (the *eLog* package), the well logs were manually correlated to the seismic data. The *Emerge* package (Hampson-Russell software) was used to integrate the well log and seismic data in order to estimate reservoir properties using multi attribute analysis. *Petrel* software was used for petrophysical analysis and its neural network routine for facies classification.

1.8 Previous Works

In early 1975 to1985 Chevron Overseas Petroleum Inc. explored the rift basins of the interior Sudan. Their extensive work resulted in the first discovery (Unity -1) in 1978 which was recovered from a thick fluvial deposit and sourced from lacustrine deposit in Muglad rift basin.

Most published work in the Muglad Basin are regional, relating to the petroleum geology of the interior Sudan basins. Browne and Fairhead (1983) used gravity data to reveal main features of the Muglad rift Basin, estimating its depth, and the maximum amount of crustal extension. Schull (1988) divided the tectonic development in the Muglad basin into three rifting phases and established a stratigraphic column which was affected by the rifting. Giedt (1990) published an Atlas of the Unity field in which he discussed the geological concept and methods leading to the discovery of (Unity -1). Kaska (1989) subdivided the fluvial lacustrine in the Muglad basin by means of biostratigraphy into five palynological zones. McHargue et al. (1993) focused on the basin development and

tectonostratigraphy. They indicated that the forming of the sedimentary sequence was a resultant of three rifting phases and each phase was followed by a thermal subsidence period. Hwang et al. (1994) determined the geological and geochemical processes responsible for the variations in oil composition associated with heterogeneous reservoirs. Abdullatif (1999) used sedimentological, mineralogical and chemical methods to evaluate the Muglad rift basin of interior Sudan.

These previous works help to recognize the stratigraphic column, to study the effect of rifting, paleogeography, paleoclimate, depositional environment, and the classification of the sandstone in the Muglad basin. Several other publications focus on the structural style in the Muglad basin like Mann (1989) who studied the thick-skin and thin-skin detachment faults in rift related basins in Sudan. His extensive work resulted in a model that illustrates the relationship between thick-skin (including basement) and thin-skin (excluding basement) detachment faults in half-graben rift-basins developed in Sudan. According to Mann (1989) the Muglad rift basin developed due to low-angle listric normal faulting, and originated within the deep crust or mantle (thick-skin). Mohammed et al. (2001) established a simplified structural model in the Unity-Kaikang area in the Muglad Basin to get a better estimation of crustal extension.

Several unpublished reports and thesis works were conducted on the Muglad basin focusing on sedimentology, tectonic evolution and paleoclimate, such as Ibrahim (2003), who studied the depositional environment, source area, sandstone composition, digenetic properties, reservoir quality and paleogeography of the Middle–Upper Cretaceous strata including subsurface facies analysis, conventional cores description, wire line logs and three seismic section analyses, petrographic analyses, scanning electron microscopic

investigations, clay mineral as well as geochemical analyses at the Unity and Heglig Fields in the SE Muglad Rift Basin. Ahmed et al. (2006) studied the spatial-temporal facies distribution applying sequence stratigraphy to understand, delineate and map the facies variation in Aradeiba formation fluvio deltaic succession in Muglad basin. Eltom (2007) characterized the facies, depositional environments and the sequence stratigraphy of Abu Gabra and Bentiu formations in the Muglad rift basin.

The period after the flourishing of the petroleum industry witnessed more publications on the formation evaluation, petroleum generation, reservoir characteristic, and petroleum system. Mohamed et al. (1999) modeled the maturity and petroleum generation in the Southern Muglad basin. Mohamed et al. (2000) studied the burial and saturation history in Heglig area, Muglad basin. Abdullatif (2002) compared and evaluated the burial digenesis, organic maturity, and oil generation of the northwest Muglad rift. Ayad and Abdullatif (2002) studied the reservoir heterogeneity and depositional environment of Bentiu formation. Idris (2002) carried out basin modeling and studied the effect of the faulting process on oil linkage in Aradeiba formation in the Muglad rift basin. Mohamed et al. (2002) estimated hydrocarbon generation in the northwest part of the Muglad basin on the basis of thermal history. Mustafa and Tyson (2002) analyzed the lacustrine source rocks of Muglad basin using a combination of organic geochemistry and palynofacies. Saida and Abdullatif (2002) studied the facies and reservoir characteristics of Zarqa Formation in the Heglig and Unity fields, Muglad rift basin. Mohamed & Mohamed (2004) analyzed oil samples from blocks 1, 2, 4, & 6 in Muglad basin using gas chromatography (GC) and gas chromatographic mass spectrometry (GCMS) and classified these oils depending on the variations in their biological markers distribution.

Idris (2005) studied the integrated petroleum system in Aradeiba and Bentiu plays of the Muglad rift basin. Mohammed (2006) built a 3D reservoir Geological Model incorporating petrophysical and geological layering for El Toor oil field Block 1A, Muglad basin. Mohammed (2008) discussed the reliability of 3D geological modeling and how it helped in the enhancement of OOIP using Toma South field in Muglad basin as a case study. Yamin and Qin (2011) studied the characteristics of the Fula depression in the Central African fault zone in terms of petroleum system.

CHAPTER 2

GEOLOGICAL AND TECTONIC SETTINGS

2.1 Introduction

Sudan's geological study was focused on the surface geology mainly for surface mapping and limited shallow mining activities. With the recent discovery of commercial hydrocarbon, extensive subsurface data have been acquired both offshore and onshore. These data revealed existence of several sedimentary basins offshore in the Red Sea and onshore in interior Sudan. These basins are all rift basins, owing their existence to the rifting activities of the Western, Central and East African Rift Systems.

Figure 2.1, shows the geological and lithological rock units distribution of southwestern part of Sudan including Muglad basin. Acquired data from these basins such as surface geology, regional gravity and magnetics show that the basins were deep and filled with continental sediments during Paleozoic and Mesozoic times. Basin depth in the central Sudan reaches to more than 10,000 m of clastic sediments. Lithofacies changes primarily reflect the variations in the subsidence rates and depositional environments of various sub-basins. This chapter, concisely, reviews some regional aspects of rifting processes, structural style, sedimentary processes and stratigraphy of the study area.

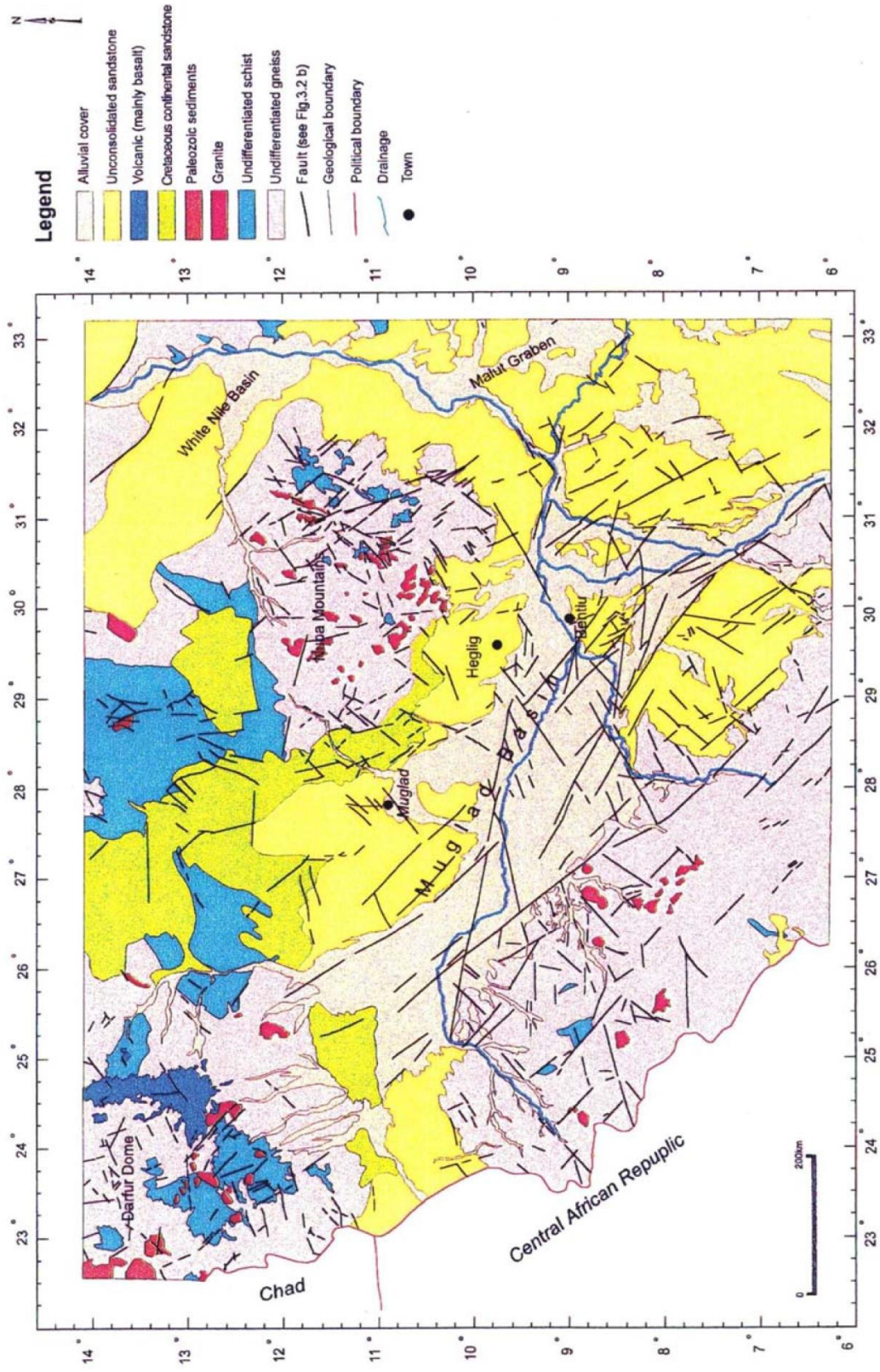

Figure 2.1 Geological map of the southwestern part of the Sudan (GRAS, 1981)

2.2 Lithostratigraphic Units of Muglad Rift Basin

All sedimentary rocks in Muglad basin are of non-marine origin. Correlations and age assignments have been established by palynomorph assemblages of fossils. Different environmental conditions have been concluded from lithological, mineralogical and paleontological information. The depositional environments, (Figure 2.2), can be grouped as alluvial fan, fluvial-braided stream, fluvial floodplain, and lacustrine determined from integrating data from wells, seismic facies mapping, and basin geometry (Schull, 1988).

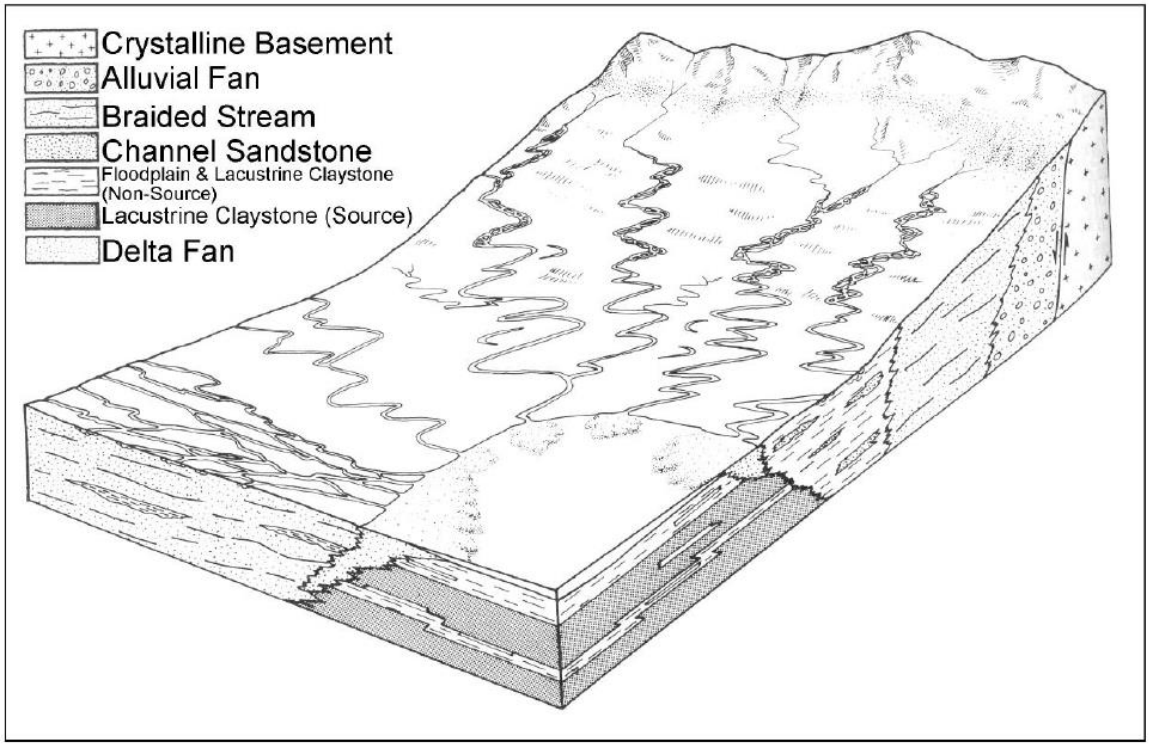

Figure 2.2 Generalized depositional model depicting the environments operative during the filling of the southern Sudan rift basin (Schull, 1988).

Based on the stratigraphic column, (Figure 2.3), the main stratigraphic units in the Muglad area are:

(1) The Precambrian - Jurassic Basement Complex.
(2) The Cretaceous strata.
(3) The Tertiary Strata.
(4) Quaternary sediments.

2.2.1 The Precambrian – Jurassic Basement Complex

The Basement Complex term is generally stratigraphically used in Sudan to include all the Precambrian and Cambrian crystalline rocks (Vail, 1978). In the study area the Basement Complex is cropping out at the SW, NW, and NE edges of the Muglad basin, (Figure 2.1). At these localities granitic as well as granodioritic gneisses were encountered and have been dated as 540 ±40 Ma (Schull, 1988).

2.2.2 The Cretaceous Strata

A few Nubian sandstone outcrops neighboring to the Muglad block, in which the rocks are non-marine, massively bedded, highly weathered, medium to coarse-grained sandstones.

In the subsurface, a thick sequence of Cretaceous sediment has been recorded. Cretaceous-Paleocene sediments reflect two cycles of deposition, each represented by a coarsening-upward sequence. These cycles are correlatable basin-wide and are directly related to rifting and basin infilling. The first cycle is represented by the Sharaf, Abu Gabra, and Bentiu Formations. The second cycle is present in the Cretaceous Darfur Group and the Paleocene Amal Formation (Schull, 1988; Kaska, 1989).

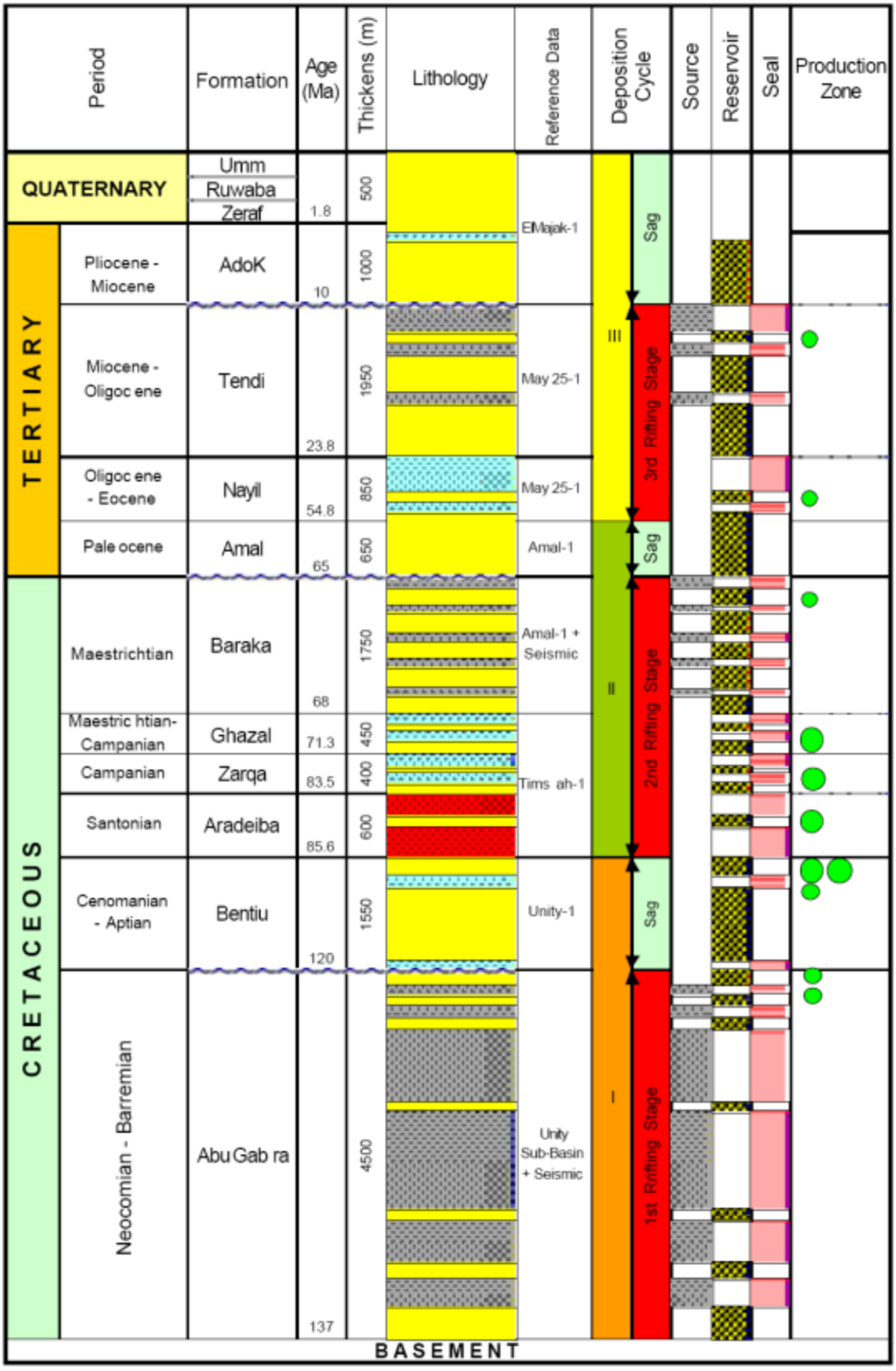

Figure 2.3 Generalized Stratigraphic column of Muglad Basin, Sudan (Idris, 2002)

The lower strata in the Muglad Basin are non-marine sediments deposited in lakes, deltas, alluvial fans and fluvial environments, (Figure 2.2). The stratigraphy and sedimentology of Cretaceous strata have been classified and summarized after Schull (1988) and Kaska (1989), (Figure 2.3) as follows:

(1) First Cycle Strata:

The early graben-fill clastics are first-cycle sediments derived from the gneissic basement complex during Early Cretaceous to Albian time which corresponding to first rifting phase. The Sharaf Formation is early syn-rift sediments of this first cycle deposited in lacustrine and floodplain environments during the Neocomian – Barremian which consists mainly of claystones and shales deposit. The Aptian-early Albian Abu Gabra Formations represent the period of greatest lacustrine development, which consists mainly of thick shales and claystones. This first cycle ends with the Late Albian – Cenomanian deposits of the Bentiu Formation, which consists predominantly of thick sandstone beds, deposits of braided and meandering streams, intercalated with thin claystone beds. The Bentiu Formation represents a change in the depositional style from an internal to an external drainage system (Figures 2.2 and 2.3).

(2) Second Cycle Strata (Darfur Group):

This second cycle occurred during the Turonian – Late Senonian second rifting phase. It represents a coarsening-upward cycle and starts with the deposition of the Darfur Group (Figure 2.3). This Group was subdivided into four formations which are from bottom to top Aradeiba, Zarga, Ghazal and Baraka Formations (Figure 2.3).

Aradeiba Formation was first assigned by Chevron to include mainly the thick sandstone-claystone strata which lie over the thick sandstone sequences of the Bentiu Formation and underlie the Zarga Formation. In lithofacies criteria, the boundary between Aradeiba and Bentiu Formations is seen as an upward passage from predominantly fluvial sandstone at the top of the Bentiu Formation to very thick mudstone – shale sequences at the base of the Aradeiba Formation. The formation consists of mudstone, sub-fissile shale, siltstone and moderately thick interbeds of fine to medium grained sandstone (Figure 2.3). This formation (Aradeiba) acts as a major reservoir horizon and as a seal as well. Palynological studies by RRI (1991) suggest a lacustrine depositional environment with fluvial – deltaic channels and assigned a Turonian – Cretaceous age for this formation. The Cretaceous ended with the deposition of increasingly coarser grained sediments, reflected in the higher sand percentage of the Ghazal and Baraka Formations, (Figure 2.3). This second cycle ended with the deposition of Amal Formation which consists of thick massive sandstones of the Paleocene, deposited in alluvial fans and in braided streams (Figure 2.3), and composed dominantly of coarse- to medium-grained quartz arenites

2.2.3 The Tertiary Strata

In outcrop, the Tertiary is represented by sequences of unconsolidated sands, gravels, silts, and clays deposited in alluvial, fluvial, and shallow lacustrine environments (Vail, 1978). These sedimentary rocks are difficult to distinguish from the overlying Pleistocene and Holocene alluvium. Few fossils have been found, and no firm age dates have been established for these units.

In the subsurface, a thick sequence of Tertiary sediments has been penetrated, (Figure 2.3). The initial deposits of the Tertiary were medium to coarse-grained clastics, followed by a single cycle of fine- to coarse-grained sedimentation associated with the final rifting phase.

(3) Third Cycle Strata

During Late Eocene – Oligocene time the third rifting phase was created by the reactivation of extensional tectonism (Schull, 1988). The lower portion of this cycle, the Nayil and Tendi Formations which represent the middle part of the Kordofan Group, (Figure 2.3), is characterized by fine-grained sediment related to the final rifting phase. These formations are dominated by claystones deposited in fluvial/ floodplain and lacustrine environments (Figure 2.3). The third cycle ended the deposition of the Adok and Zeraf Formations, during Late Oligocene to Middle Miocene/ Recent which is generally characterized by interbedded sandstone and claystone with an increasing sand content. Deposition happened mainly in braided stream environments (Figures. 2.2 and 2.3).

2.2.4 The Quaternary Strata

Quaternary Strata represent the latest cover of the study area, which consists of Umm-Rawaba and Zaraf formations composed of unconsolidated to semi-consolidated continental gravels, sands, clayey sands and clays of fluvial and lacustrine environments (Vail, 1978).

2.3 Tectonic Evolution of the Muglad Rift Basin

Rift related basins in Sudan developed in the late Jurassic as a result of separation of west and east Gondwana. These rift basins are regionally linked to the Central African Shear Zone (CASZ) which began in late Jurassic (?) and consists of Benue trough in Nigeria, Chad basin in Chad and Muglad basin in Sudan. Muglad basin is part of the trend of Cretaceous sedimentary basins of apparent rift origin related to the global phenomenon of plate tectonics, Figure (2.4).The southern Sudan interior rift basins are defined by extensive NW–SE, NNW–SSE, N–S, NE–SW, and E–W rifts that started to develop during the late Jurassic to Early Cretaceous time (Schull, 1988). The split-up of the super-continent Pangea resulted in the formation of the Central African Shear Zone (CASZ), which controlled the orientation of the faults within the basin. The majority of the faults are deep-seated normal faults trending in a NNW-SSE direction perpendicular to the CASZ (Browne and Fairhead 1983; Schull 1988).

Browne and Fairhead (1983) suggested three periods of rifting which occurred in response to crustal extension, this provided the isostatic mechanisms of subsidence accomplished by normal faulting parallel and sub-parallel to the basinal axes and margins. Schull (1988) suggested from the drilled wells that the initial strongest rifting phase have begun in the Jurassic (?) - Early Cretaceous (130-160 Ma) and lasted until near the end of the Albian.

According to Schull (1988) the tectonic evolution of Muglad basin can be divided into a pre-rifting phase, three rifting phases, and a sag phase which are well documented by geophysical data, well information, and regional geology as follows:

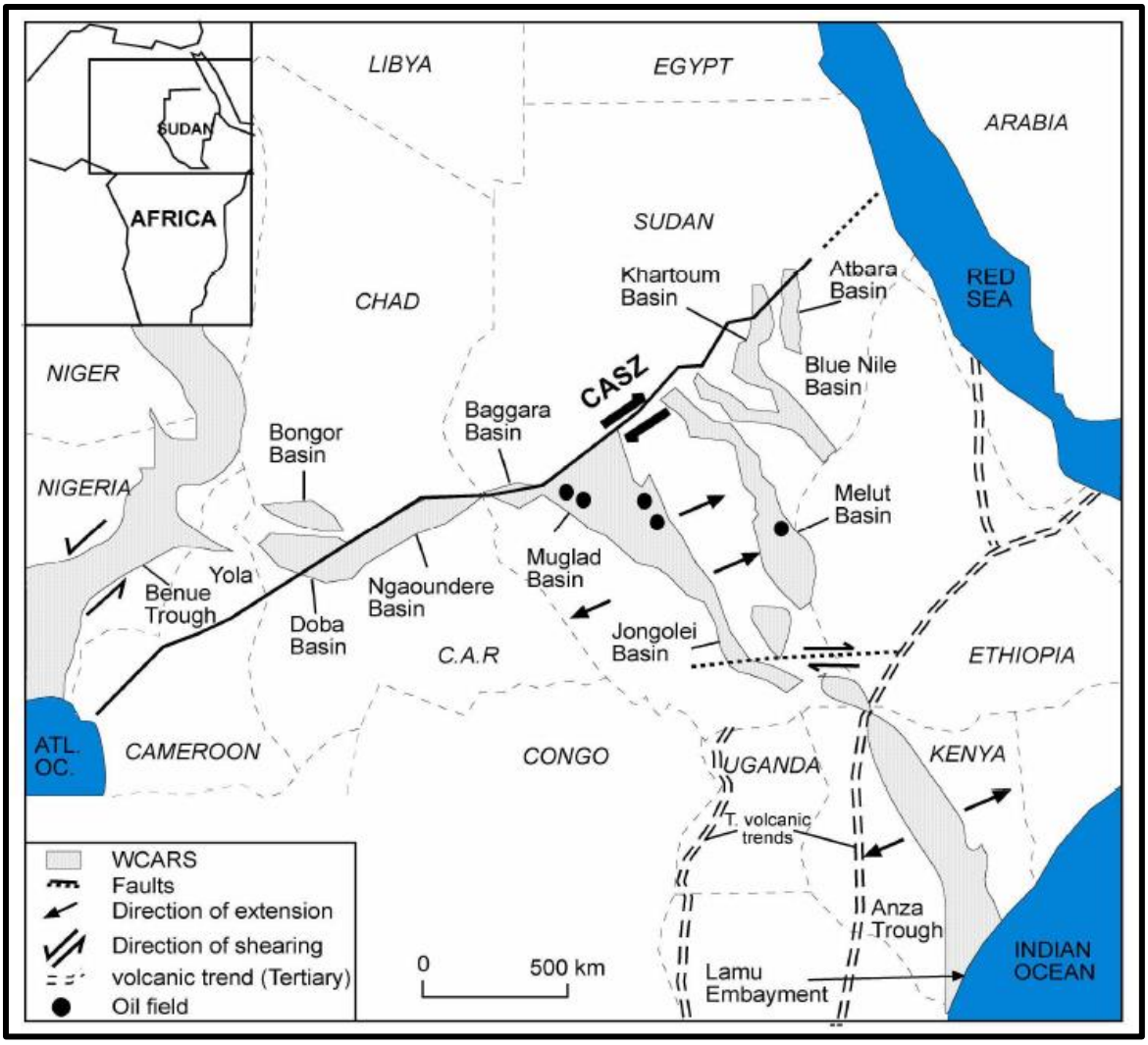

Figure 2.4 Schematic map showing the relationship between the Central African Shear Zone, the Muglad Rift Basin, Sudan and associated rift basins, (from Fairhead, 1988)

2.3.1 Pre- rifting Phase

By the end of the Pan-African orogeny (550 Ma ± 100m.y.), this region had become a consolidated platform.

During the remainder of the Paleozoic and early Mesozoic, this highland platform provided sediment to adjacent subsiding areas (Vail 1985; Schandelmeier et al., 1993). The nearest preserved Paleozoic rocks are continental sediments in northwestern Sudan

near the Chad and Libyan borders. The general lack of lithic fragments in the oldest rift sediments further suggests that no significant amount of sedimentary section existed in the Muglad basin area prior to rifting (Schull, 1988).

2.3.2 Rifting Phase

Three distinct periods of rifting have occurred in response to crustal extension, which provided the isostatic mechanism for subsidence (Browne and Fairhead 1983; Schull 1988). Subsidence was accomplished by normal faulting parallel and sub-parallel to the basinal axes and margins. Based on wells and seismic data, rifting is divided into three phases:

2.3.2.1 First Rifting Phase

This phase is thought to have begun in the Jurassic (?)-Early Cretaceous (130-160 Ma). The basement is overlain by Neocomian-Barremian lacustrine siltstones and claystones. Well control and seismic data indicate that this initial and strongest rifting phase lasted until near the end of the Albian. In the Sudan, no volcanism is known to be associated with this early rifting phase. The termination of the initial rifting is stratigraphically marked by basin-wide deposition of the thick sandstones of the Bentiu Formation (Schull, 1988).

2.3.2.2 Second Rifting Phase

It occurred during the Turonian-late Senonian. Stratigraphically, this phase is seen in the widespread deposition of lacustrine and floodplain claystones and siltstones, which abruptly terminated the deposition of the Bentiu Formation (Schull, 1988). The end of

this phase is marked by the deposition of an increasingly sand-rich sequence that concluded with thick Paleocene sandstone, the Amal Formation (Schull, 1988).

2.3.2.3 Third Rifting Phase

It began in the late Eocene-Oligocene. This final phase is reflected in the sediments by a thick sequence of lacustrine and floodplain claystones and siltstones. After this period of rifting, deposition became more sand-rich throughout the late Oligocene-Miocene (Schull, 1988).

2.3.3 Sag Phase

In the middle Miocene, the basinal areas entered an intracratonic sag phase which was first identified by Schull (1988), of very gentle subsidence accompanied by little or no faulting. Limited outcrops of volcanic rock in the area southeast of Muglad dated at 5.6 Ma ± 0.6 m.y. and 2.7 Ma ± 0.8 m.y. indicate that minor volcanism occurred locally (Schull, 1988). During this time, however, extensive volcanism did occur in some adjoining areas to the north (e.g., Jebel Marra, and in the East African rift system to the east and southeast). Currently, the area is stable with little earthquake or volcanic activity (Browne et al, 1985).

2.4 Structural Style of Muglad Rift Basin

The split-up (dextral strike slip fault) of the super-continent Pangea resulted in the formation of the Central African Shear Zone (CASZ) in the Early Cretaceous, which controlled the orientation of the faults within the basin, led to the creation of a series of passive rifts, such as the Muglad basin and others (Genik, 1993; Schandelmeier and Pudlo, 1990).

Structural studies on the Muglad rift basin by Schull (1988), Mann (1989) and Mc Hargue et al.(1993) emphasized that the Muglad rift basin is a half graben formed as a result of extensional forces in early Cretaceous. The Muglad basin is considered as an extensional fault basin which consists of a half-graben, half-horst structure with a northwest trend. Regionally from north to south, the basin looks like an asymmetrical half-graben - graben comprising of rolling anticlines, drape anticlines, reversal anticlines, and tilt blocks as the main structural types, which are also important for hydrocarbon accumulation (Zhang, 2007).

The three rifting phases resulted in a long complex history of horst and graben development and the formation of a highly complicated fault system. The predominant fault orientation is parallel or sub-parallel to the strike of the primary grabens and basin margins. In the central and southern Muglad basin, an apparently older north-northwest trend also exists (Schull, 1988).

Mann (1989) studied the thick-skin and thin-skin detachment faults in rift related basins in Sudan. His extensive work resulted in a model that illustrates the relationship between thick-skin (including basement) and thin-skin (excluding basement) detachment faults in

half-graben rift-basins developed in Sudan. According to Mann (1989) the Muglad rift basin developed due to low-angle listric normal faulting, and originated within the deep crust or mantle (thick-skin).

Structurally, the Fula depression (northeastern part of Block 6) subdivided into a southern fault zone, a southern sub-depression, a central faulted uplift, a northern sub-depression, and a northern fault zone. The depression has north-south and north-northeast trending faults (Yamin and Qin, 2011). The general structures of the Muglad basin are shown in Figure (2.5). The productive and prospective structures resulting from this complex extensional history have been categorized as rotated fault blocks, drape folds, and reverse drag folds.

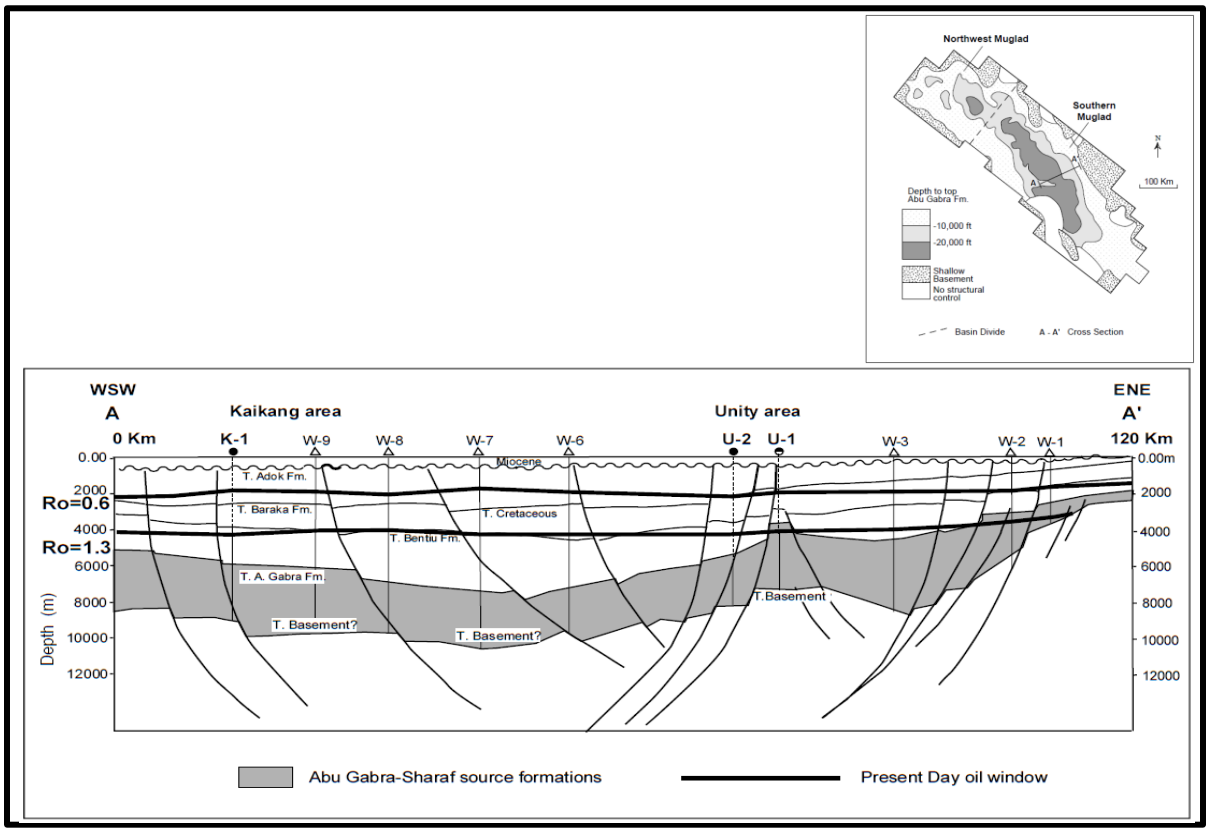

Figure 2.5 Generalized structure map and cross-section of Muglad basin indicating the general structures in the basin, main source rock, and the productive zone from Mohamed et al. (1999)

2.5 Petroleum System

The hydrocarbon system has an ideal combination of source, reservoir and top seal rocks which are all Cretaceous in age. In Fula depression the source rock is the lower part of Abu Gabra Formation which is characterized by deep lacustrine shale of early Cretaceous. The reservoir rock belongs to the first rifting phase characterized by braided-stream sandstones of the Bentiu Formation. The top seal is the mudstone of Darfur Group in the Upper Cretaceous. The combination of source, reservoir and top seal with the tectonics created different patterns of structural hydrocarbon traps such as Y-shaped, fan-shaped as well as step-wise patterns giving rise to good oil-trapping tilted blocks. The main types of hydrocarbon traps according to Gibbs (1990) are reverse faulted blocks, reverse faulted anticlines, and reverse faulted noses.

The source rock (lacustrine shale) is characteristic only in the first rifting phase sequence which took place in early Cretaceous while the reservoir sandstones are characteristic in all rift sequences, but the productive zones were found in Bentiu and Aradeiba Formations.

Oil in Aradeiba Formation is mainly in Aradeiba-D Member. Aradeiba-D Member was deposited in lacustrine-fluvial environment, but the sand ranges and grain size is generally smaller than that of Bentiu. Heterogeneity and dimensions of sandstone bodies and the siltstone/mudstone barrier/baffle units vary more greatly within Aradeiba-D than that in Bentiu.

CHAPTER 3

PETROPHYSICAL AND FACIES ANALYSIS

3.1 Introduction

Selecting reasonable petrophysical parameters are critical for well log interpretation and are also the key step in reservoir evaluation. In this chapter 18 well logs analyzed to estimate four petrophysical parameters, namely shale content (Vsh), porosity, permeability, and fluid saturation for Aradeiba-D Member. Also, neural network applied for facies classification. These parameters are the base upon which the reservoir modeling through multi-attribute transforms is being done.

The presence of shale in reservoir rocks affects the calculated values of water saturation and porosity from well logs. The effect of shale on logs varies from subtle to dramatic, depending on the measurement and the type of shale. Resistivity logs are seriously affected by thin layers of low resistivity shale in a high resistivity hydrocarbon reservoir zone which results in miscalculation of saturation. The resistivity variations are due to the extra conductive layer in the formation and not to a simple addition as with porosity.

Shale can be distributed through the reservoir rock in three ways (structural, laminar, and dispersed), (Figure 3.1). Structural shale consists of the shale grains replacing some of the sand grains. In this case the matrix density changes but the porosity is not altered. Laminar shale consists of thin layers of shale in the matrix, replacing both matrix and

porosity. There are hence changes both in matrix density and the porosity. Dispersed shale is the clay mineral that fills in the intergranular space that is it changes the porosity, leaving the matrix density unchanged, Poupon et al. (1970).

Thus, in shaly sand reservoir evaluation (mainly in effective porosity and water saturation determination) shale volume must be accurately calculated. In addition, water saturation determination cannot be accurately obtained by the use of a classical water saturation equation (i.e. Archie's equation). Therefore, one of the modifications of Archie's equation (e.g. Indonesia equation, Nigeria Equation, Simandoux or Venezuela) should be used to relate rock resistivity to water saturation.

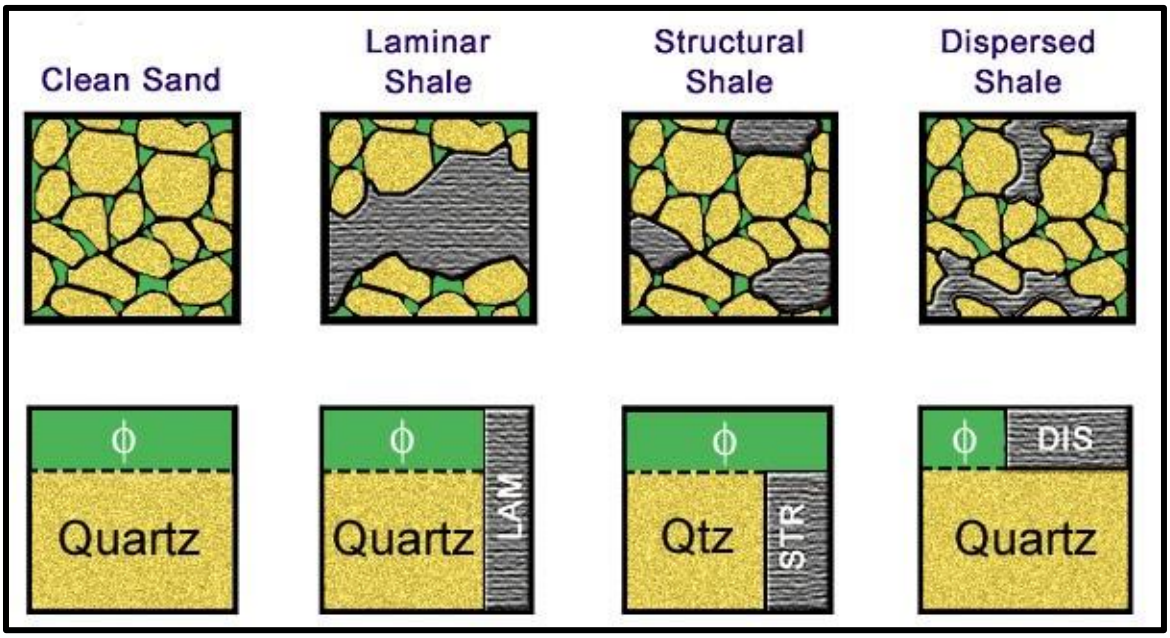

Figure 3.1 Different shale distributions in a formation (after Schlumberger, 1987)

3.2 Shale Volume Determination

The shale volume (Vsh) is an important lithological parameter of a reservoir, and it affects the petrophysical properties to a great extent. Shale minerals generate characteristic responses on several logs such as LLD, SP, GR, RHOB, NPHI, etc. These logs are often called 'shale indicators' (Poupon and Gaymard, 1970), and they are commonly used to estimate the amount of shale present in a given shaly-sand formation. Shales can be divided into two, effective and passive shales. We can differentiate between the two types by the CEC (cation exchange capacity). Effective shale (Montmorillonite and Bentonite) has considerable CEC, while passive shale (Kaolinite and Chlorite) has essentially zero CEC, Kurniawan (2005). In addition effective shale can be identified by the shale indicator logs while passive shale is noticed by the neutron tool. In this study, two techniques will be used in shale volume calculation. In order to minimize errors due to the possible existence of passive shales and radioactive sands the lowest value of shale volume will be used in the calculation of porosity and water saturation.

3.2.1 Gamma Ray Shale Volume

Shale content evaluation using gamma ray log assumes that there are no radioactive minerals other than clays. The gamma ray shale index (GR_{Index}) is defined as, Schlumberger (1987):

$$\mathrm{GR_{Index}} = \frac{GR_{log} - \mathrm{GR_{min}}}{\mathrm{GR_{max}} - \mathrm{GR_{min}}} \tag{3.1}$$

where:

GR_{log} is Gamma ray value from log,

GR_{max} is Gamma ray value from log at shale line,

GR_{min} is Gamma ray value from log at sand line.

Shale line and sand line values are illustrated in Table 3.1 for each well. The GR_{Index} has been empirically correlated to fractional volumes of shale by a number of researchers which resulted in linear and nonlinear relations depending on formation age or other local information. In this study, Larionov (1969) equation valid for older rocks was used for shale volume (V_{sh}) calculation, Schlumberger (1987).

$$V_{Sh} = 0.33 \times (2^{GR_{Index}} - 1) \tag{3.2}$$

3.2.2 Density- Neutron Shale Volume

Volume of shale calculated from the separation between the density and neutron logs is arrived at somewhat differently than when calculating Vsh from the gamma ray log. If the proper grain density and neutron matrix density are chosen, the density and neutron curves should overlay in a clean sand zone. Maximum separation will be observed in shale. This separation can be used to establish the shale end-point. Linear interpolation can then be performed between the two endpoints of maximum and minimum separation, Schlumberger (1987).

$$V_{Sh} = \frac{(\varphi_N - \varphi_D)}{(\varphi_{N\_Sh} - \varphi_{D\_Sh})} \tag{3.3}$$

The terms in the numerator are the values of neutron density reading (φ_N) and density porosity reading (φ_D) equation (3.10) in the zone of interest while the denominator is the

difference between the neutron and density porosity readings in the zone believed to be 100% shale.

Well Name	GR_{min} (API)	GR_{max} (API)	Φ_{N_SH} (fraction)	Φ_{D_SH} (fraction)	Δt_{sh} (µsec/ft)	R_{sh} (Ohm.m)
X-1	65	130	0.43	0.33	152.32	2.82
X-2	55	115	0.47	0.31	148.18	2.85
X-3	70	140	0.49	0.32	137.64	2.45
X-4	65	150	0.43	0.32	133.92	2.79
X-5	50	110	0.41	0.287	142.8	2.89
X-6	40	90	0.43	0.297	145.42	2.91
X-7	50	140	0.43	0.327	140.48	2.67
X-8	50	110	0.43	0.293	140.43	2.55
X-9	55	95	0.47	0.298	143.74	2.94
X-10	45	120	0.41	0.259	141.18	2.96
X-11	55	110	0.47	0.314	146.46	2.86
X-12	50	90	0.46	0.277	150.60	2.37
X-13	65	110	0.40	0.275	141.83	3.00
X-14	40	110	0.47	0.326	148.19	2.85
X-15	50	130	0.45	0.288	140.22	3.11
X-16	40	110	0.40	0.298	147.56	2.54
X-17	40	90	0.46	0.343	143.93	2.74
X-18	40	130	0.47	0.289	143.36	2.51

Table 3.1 Sand (GR_{min}), Shale (GR_{max}) base lines, compressional transit time (Δt_{sh}) in shale, neutron porosity (Φ_{N_SH}) in shale, density porosity (Φ_{D_SH}) in shale and shale resistivity (R_{sh}) values for each individual well used for the petrophysical parameters calculation.

The shale percentage map (Figure 3.2) shows an increase of shale content along the eastern part and northwestern part of the area which reaches its highest value of 44% at the X-13 well in the central south east of the studied area while it decreases to 13% at the X-18 well locality in the southwestern part. Table 3.2 presents the average parameter values of shale volume, porosity, permeability, and water saturation in Aradeiba-D sand zone.

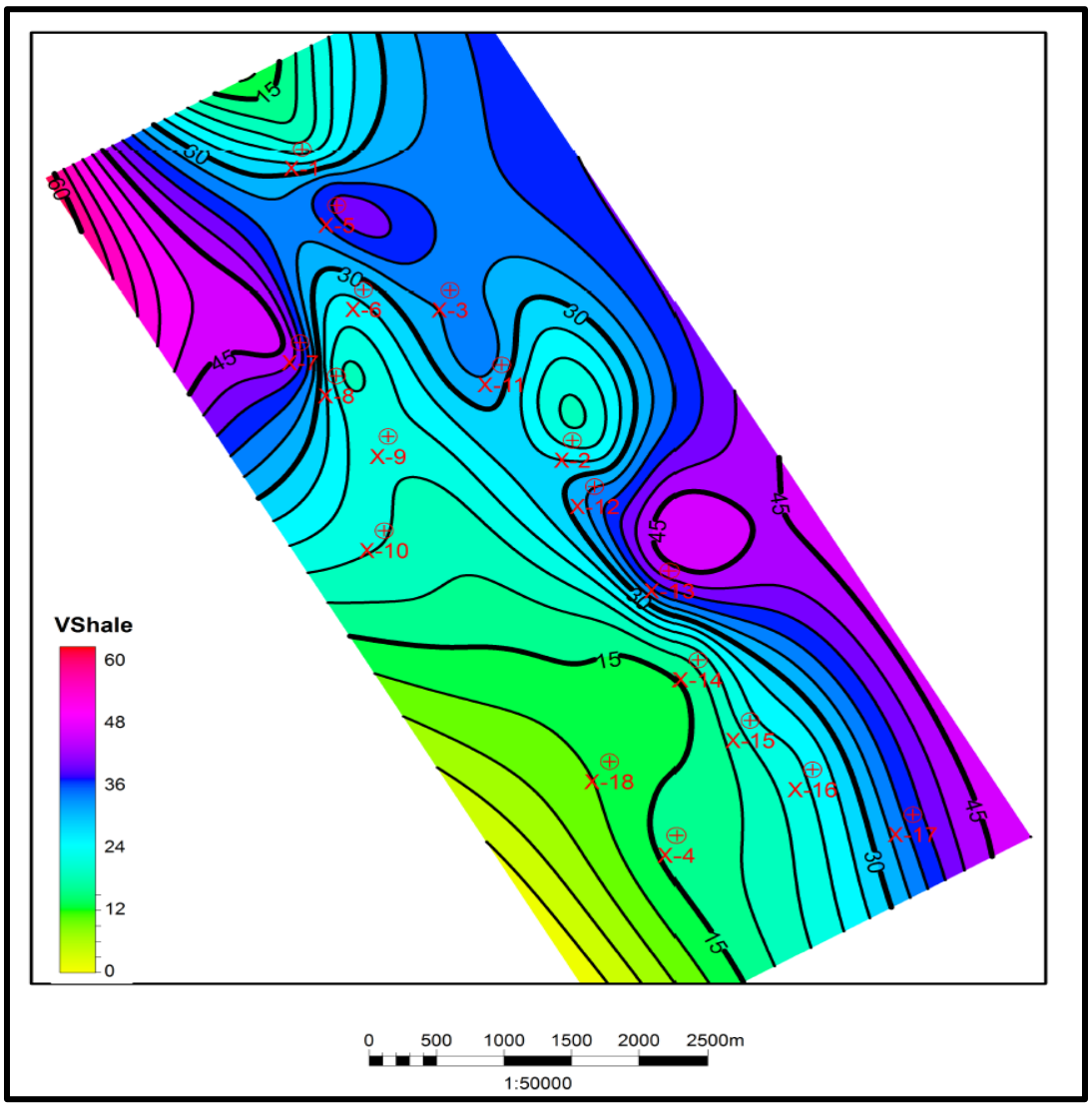

Figure 3.2 Shale distribution map for Aradeiba-D sand zone in the study area. The color scale is in percentage.

Well Name	V_{Sh} (%)	Porosity (%)	Permeability (Darcy)	Water Saturation (%)
X-1	22.5	34.1	2.852	12.8
X-2	22.7	37.0	6.994	26.2
X-3	33.7	24.9	0.633	51.4
X-4	16.0	35.6	5.607	11.0
X-5	39.4	38.1	10.096	20.2
X-6	28.6	33.3	9.246	15.5
X-7	39.0	23.6	0.217	22.3
X-8	22.7	33.4	10.871	16.3
X-9	22.7	30.8	6.565	12.9
X-10	21.2	33.9	6.134	27.4
X-11	31.9	24.5	0.396	43.1
X-12	32.8	36.5	9.637	29.7
X-13	43.5	25.2	0.462	28.0
X-14	19.5	36.7	8.741	4.9
X-15	23.1	35.3	11.195	15.3
X-16	25.0	32.6	11.984	18.0
X-17	37.6	24.4	2.046	45.8
X-18	13.3	30.5	0.480	10.1

Table 3.2 Average parameters (Shale volume, porosity, permeability, and water saturation) values for the Aradeiba-D sand zone in all well logs

3.3 Porosity Determination

Porosity is defined as the ratio of pore volume to bulk volume. Primary porosity is the porosity developed during the original sedimentation process by which the rock is created. Secondary porosity is formed after sedimentary deposition and compaction through diagenesis, Schlumberger (1987).

In most cases, secondary porosity results in higher permeability than primary granular porosity. However, the porosity derived directly from logs without correction for shale content is termed apparent or total porosity. In a zone of no shales, the total porosity equals the effective porosity.

Porosity can be determined from a variety of wireline tools, density, neutron, and acoustic. When determining porosity from the wireline tools, an understanding of the relationship between pore volume and the physics of the measurement technique is necessary since porosity is based on an indirect measurement and the different log measurements used to derive porosity have advantages and limitations. Porosity is a very important parameter for oil saturation, oil reserve, and productivity. Porosity models are as follows:

3.3.1 Sonic Porosity

Sonic porosity is derived from the measurement of the interval transit time of a compressional wave traveling through the formation. The following equation is used to calculate sonic porosity:

In shale-free formations, the total porosity is determined by Wyllie's et al. (1958) formula as:

$$\varphi_S = \frac{\Delta t_{log} - \Delta t_{ma}}{\Delta t_f - \Delta t_{ma}} \tag{3.4}$$

If the compaction factor (C_p) is included, then:

$$\varphi_S = \frac{\Delta t_{log} - \Delta t_{ma}}{\Delta t_f - \Delta t_{ma}} \times \frac{1}{C_p} \tag{3.5}$$

In such case: $C_p = \frac{\Delta t_{sh} \times C}{100}$ (3.6)

where: C is a constant which normally equals 1.0 (Hilchie, 1978).

In shaly formations, the total porosity is determined using the formula of Dresser Atlas (1979):

$$\varphi_S = \left[\frac{\Delta t_{log} - \Delta t_{ma}}{\Delta t_f - \Delta t_{ma}} \times \frac{1}{C_p}\right] - V_{Sh}\left[\frac{\Delta t_{Sh} - \Delta t_{ma}}{\Delta t_f - \Delta t_{ma}}\right] \quad (3.7)$$

where: φ_S is sonic porosity,

Δt_{log} is measured compressional transit time,

Δt_{ma} is the rock matrix transit time [for sandstone it is usually (55.5 - 51.0) µsec/ft],

Δt_f is pore fluid transit time usually 189 (µsec/ft),

Δt_{Sh} is the compressional transit time in adjacent shale (Table 3.1).

3.3.2 Neutron Porosity

Neutron logs give directly the porosity values on the log track in clean formations. Correction of the log data for the different factors affecting it must be taken into consideration. These factors include borehole size, mud cake thickness, borehole and formation water salinities, pressure and temperature. However, the compensated neutron log (CNL) is designed to minimize the effect of the borehole parameters (Schlumberger, 1987). If shales intervene, their effect must be corrected through the following equation:

$$\varphi_{N\_c} = \varphi_{N\_log} - V_{Sh}\varphi_{N_{Sh}} \quad (3.8)$$

where: φ_{N_c} is corrected neutron porosity,

$\varphi_{N_{Sh}}$ is the neutron porosity in adjacent shale (Table 3.1),

φ_{N_log} is measured neutron porosity.

3.3.3 Density Porosity

The proportionality of mass and porosity provides a direct method for determining reservoir rock porosity, but the matrix density must be known. Density tools are considered the most reliable porosity-sensitive devices; their measurements are more sensitive to porosity than to lithology. Neutron logs respond more to lithology change. The basic equation for calculating porosity from measured bulk density is, Schlumberger, (1987):

$$\rho_b = \rho_{ma}(1-\varphi) + \rho_f\varphi \tag{3.9}$$

Solving for φ the shale free formation porosity (Wyllie, 1963):

$$\varphi_D = \frac{\rho_{ma} - \rho_b}{\rho_{ma} - \rho_f} \tag{3.10}$$

In shaly formations, the density porosity is determined from the formula of Dresser Atlas (1979) as:

$$\varphi_{D\_C} = \left[\frac{\rho_{ma} - \rho_b}{\rho_{ma} - \rho_f}\right] - V_{Sh}\left[\frac{\rho_{ma} - \rho_{sh}}{\rho_{ma} - \rho_f}\right] \tag{3.11}$$

or: $$\varphi_{D\_C} = \varphi_D - V_{Sh}\varphi_{D_{Sh}} \tag{3.12}$$

where: φ_D is the density porosity,

φ_{D_C} is the corrected density porosity from shale,

ρ_b is density log reading,

ρ_{ma} is matrix density, commonly used value for quartz is 2.648 g/cc,

ρ_f is fluid average density usually 1.0 g/cc (fresh water filtrates),

ρ_{sh} is the shale zone density (Table 3.1).

3.3.4 Density-Neutron Combination Porosity

The combination of neutron and density is considered as a good approach for calculating porosity in clean and shaly zones.

- In clean zones :

$$\varphi_{(D-N)} = \frac{\varphi_D + \varphi_N}{2} \tag{3.13}$$

- In shaly zones:

$$\varphi_{(D-N)} = \sqrt{\frac{\varphi_{D\_C}^2 + \varphi_{N\_C}^2}{2}} \tag{3.13}$$

The porosity values obtained from sonic, density, neutron logs and the combined density-neutron are termed Φ_S, Φ_D, Φ_N and $\Phi_{(D\text{-}N)}$ respectively for clean and shaly zones, and their average (Φ_{average}) is calculated for each zone to get the optimum total corrected porosity value.

Generally, the porosity distribution of Aradeiba-D sand decreases gradually southeastern, northeastern, and northwestern-ward, (Figure 3.3). The minimum porosity value is (24%) is represented at X-17 and X-11 wells in the southeast and northeast part till reaches its maximum value (38%) at X-5 well. The porosity distribution follows the same trend of the shale volume as in Figure 3.2, (i.e. high porosities with low shale content). Table 3.4

presents the average parameter values of shale volume, porosity, permeability, and water saturation in the Aradeiba-D sand zone.

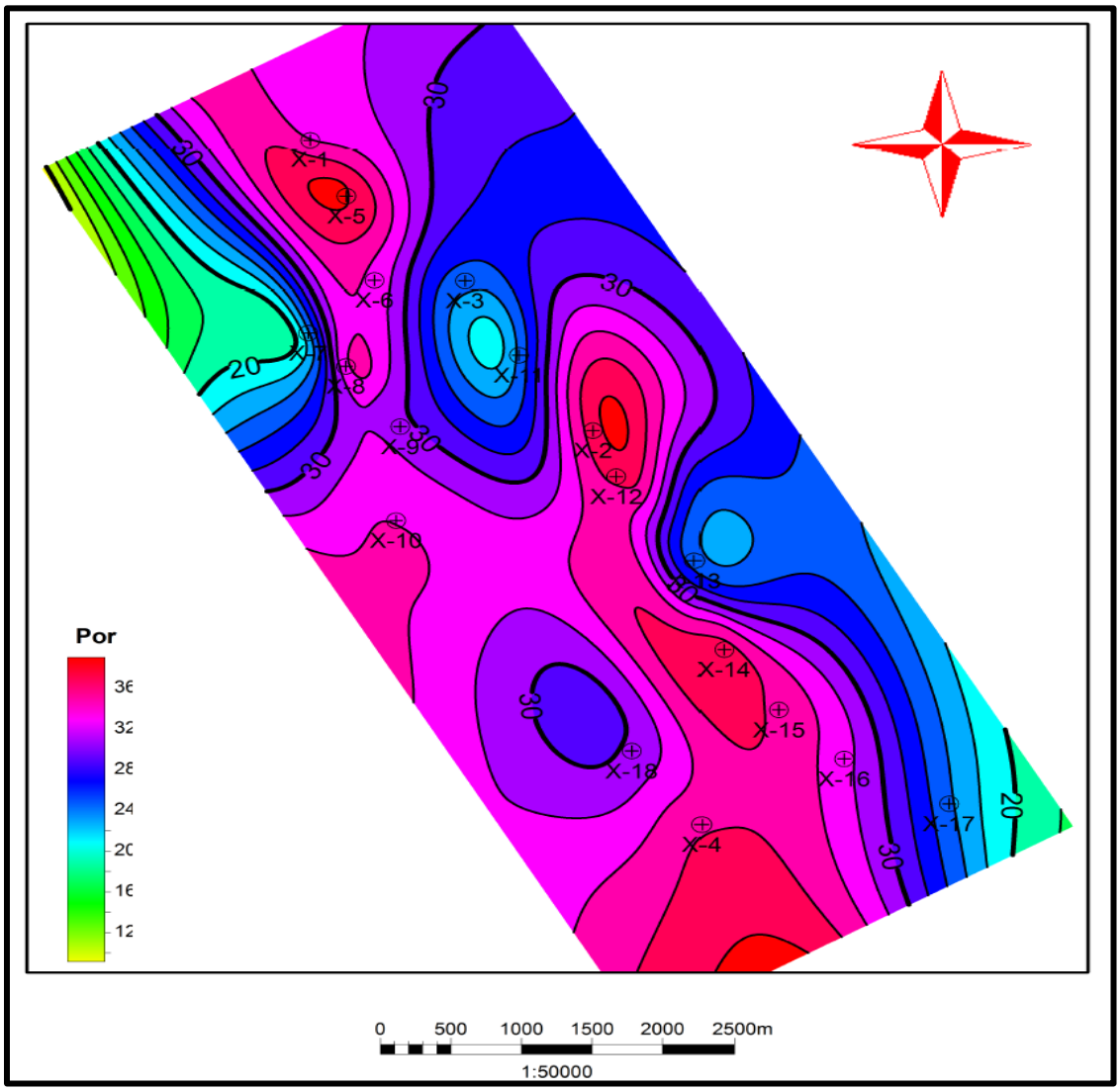

Figure 3.3 Porosity distribution map for Aradeiba-D sand zone in the study area. The color scale is in percentage.

3.4 Permeability Determination

Permeability is one of the most important parameters of reservoir; it describes the ability of fluid to flow through the rock and is one of the main controlling factors of hydrocarbon productivity. Up to now, however, none of the current well logging techniques can be used to measure it directly. In this study, core analysis results from reports were used to estimate formation permeability.

For sandstones with intergranular pores, which are the main channels for fluid, their core porosity and permeability data obey the permeability model established for the Aradeiba formation (CNPC, 2007) as:

$$K = 0.0012 \times e^{0.4093\varphi} \tag{3.14}$$

where: K is the permeability in mD (milli Darcy),

φ is the porosity in percentage (average porosity was used).

The permeability distribution, (Figure 3.4), of the Aradeiba-D sand follows the shale volume and porosity distribution. Its maximum value is 11Darcy at X-16 well and the minimum value is 0.216 Darcy at X-7 well. Table 3.4 presents the average parameter values of shale volume, porosity, permeability, and water saturation in the Aradeiba-D sand zone.

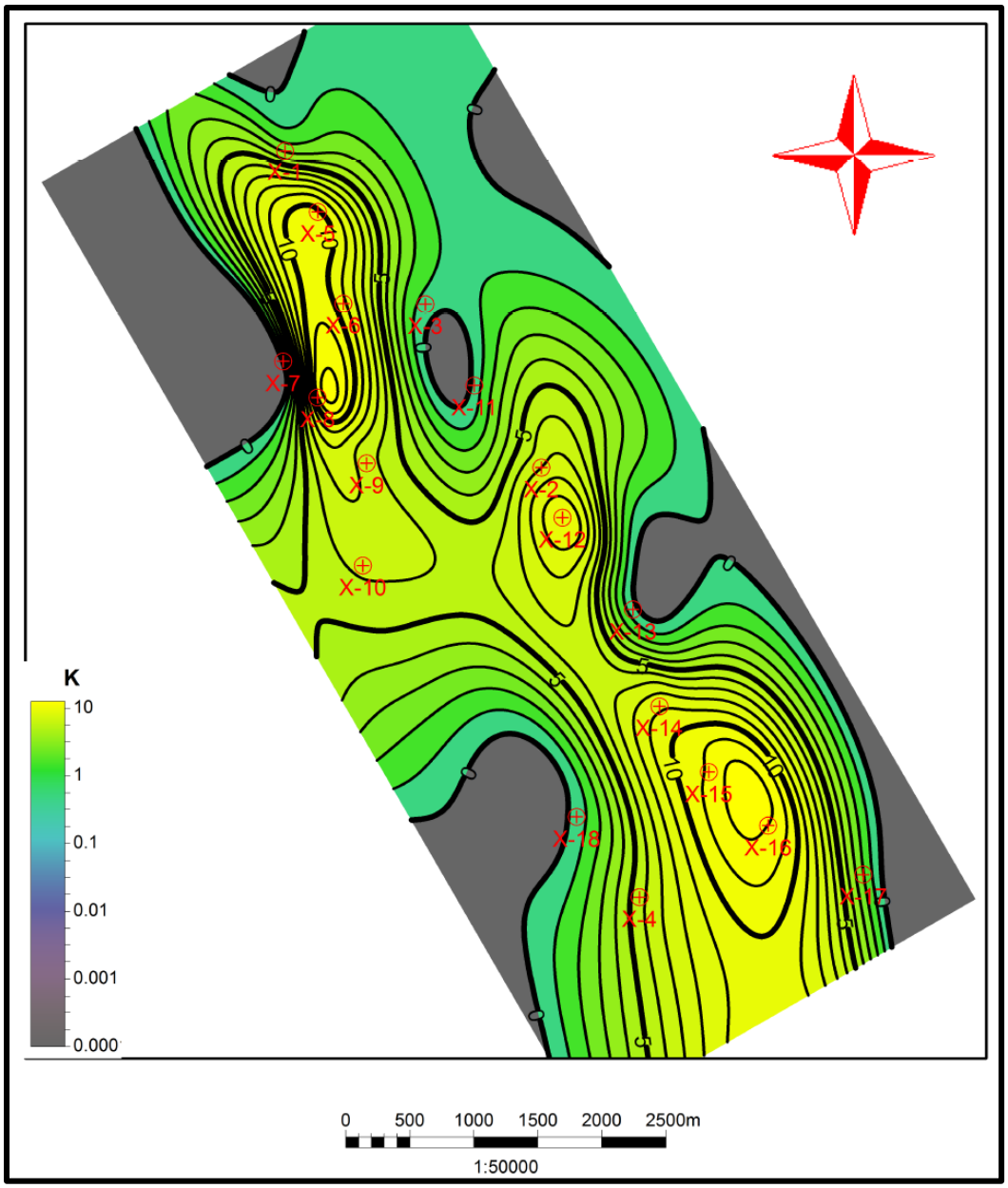

Figure 3.4 Permeability distribution map for Aradeiba-D sand zone in the study area. The color scale is in Darcy unit.

3.5 Water Saturation Determination

Water saturation, S_w, is the fraction of the pore volume of the reservoir rock that is filled with water. It is assumed that the pore volume not filled with water is filled with hydrocarbon. Determining S_w is one of the basic objectives of well logging. Although S_w can be determined by a number of methods, specific circumstances affect or limit the accuracy of each method and it is crucial to use the appropriate one Schlumberger, (1987).

Several measurements and petrophysical parameters are essential in deriving accurate saturation values. We need precise determination of true resistivity (R_t), connate water resistivity (R_w), and shale resistivity (R_{sh}); reliable and accurate porosity information; adequate formation factor to porosity relation; adequate saturation exponent for saturation determination; and accurate shale volume (Vsh) to eliminate shale effects.

Numerous methods are available to calculate water saturation, but in this study the Indonesia equation (1971) was used.

The Indonesia equation is an empirical model introduced by Poupon and Leveaux (1971). This equation was developed based on the typical characteristics of fresh formation waters and high degrees of shaliness that are present in many oil reservoirs in Indonesia. In this model the conductivity relationship between (R_t) and (S_w) is a result of conductivities of the clay, formation water and an additional conductivity arising through the interaction between them. The Indonesia model is:

$$S_w = \frac{1}{R_t}\left[\left[\frac{V_{Sh}^{(5V_{Sh})}}{\sqrt{R_{Sh}}}\right] + \left[\frac{\varphi^{\frac{m}{2}}}{\sqrt{aR_w}}\right]\right]^{-\frac{2}{n}} \quad (3.15)$$

where: S_w is water saturation in fraction,

a is Archie's coefficient (tortuosity factor)=1,

m is Archie's exponent (cementation exponent)=1.79,

n is saturation exponent = 1.83,

φ is porosity in fraction (average porosity was used),

V_{Sh} is shale volume in fraction,

R_w is formation water resistivity = 0.58 ohm.m,

R_{Sh} is shale resistivity in ohm.m (Table 3.1),

R_t is true formation resistivity in ohm.m.

Based on core data analysis and water samples, (CNPC, 2007), m, n, and R_w were determined for Aradeiba-D as 1.79, 1.83, and 0.58 ohm.m respectively. The water saturation map, (Figure 3.5), shows that, the maximum value of the water proportion is 51% at the X-3 well and the minimum value of 5% occurs at the X-14 well localities. Also, water saturation distribution follows the same trend as shale volume, porosity, and permeability. Table 3.4 presents the average parameter values of shale volume, porosity, permeability, and water saturation in the Aradeiba-D sand zone.

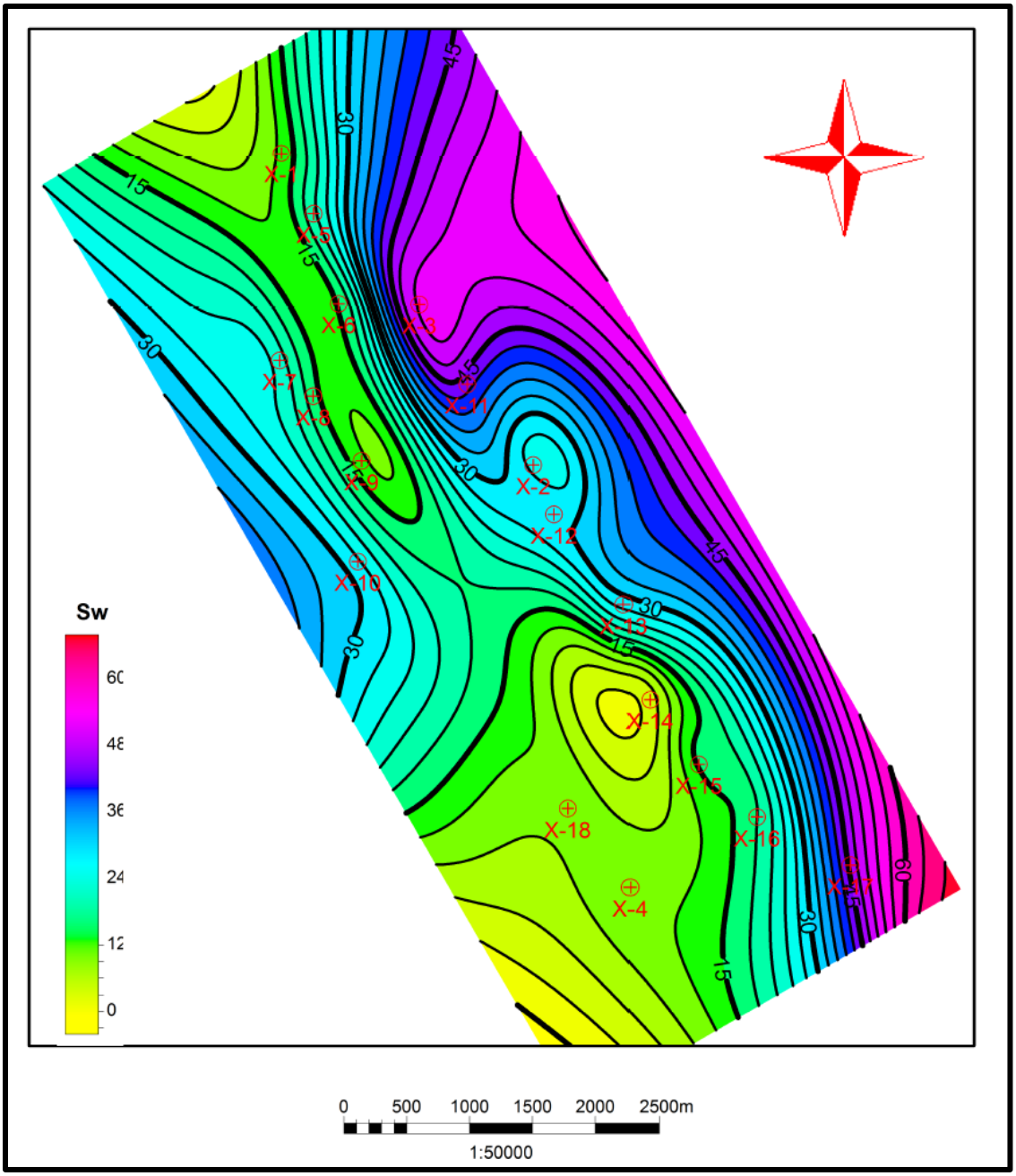

Figure 3.5 Water saturation distribution map for Aradeiba-D sand zone in the study area. The color scale is in percentage.

3.6 Facies Analysis

The Artificial Neural Network (ANN) is a tool for automatically finding relationships between multiple known parameters and a single unknown parameter. It is a computational model imitating biological neural networks which consists of an interconnected group (network) of artificial neurons (nodes) (Figure 3.6). It processes information by using interconnecting networks of simple units. A neural network is a non-linear statistical modeling tool, able to model complex relationships between inputs and outputs or to find patterns in the data.

On the basis of gamma ray (GR), sonic (DT), neutron porosity (NPHI), bulk density (RHOZ), and deep resistivity (RLA5) logs, the ANN was applied for facies classification. Table 3.3 shows correlation analysis of the selected input data. Note that the correlation coefficient should not be too close to "one" as that would indicate the data might come from the same source. However, if the correlation is too low, there is no relationship at all between the data and it will be difficult to achieve a good mathematical model that can be used for prediction.

Three main lithological facies were identified from well cuttings, (i) the first is thick massive grey to dark grey and purplish red shale, (ii) the second is fine- to medium grained sandstone of mainly feldspathic and subfeldspathic quartz and minor argillaceous matrix, with grains sub-rounded to sub-angular, medium to poorly sorted, (iii) the third sandstone consists of mainly feldspathic and subfeldspathic quartz and minor argillaceous matrix and its grains are sub-rounded to sub-angular, medium to poorly sorted.

Accordingly, the ANN was trained to classify the facies into three groups: shale, shaly sand, and sandstone. The last row (Total) in (Table 3.3) shows the correlation coefficient between the input data (gamma ray, sonic, neutron porosity, bulk density, and deep resistivity logs) and the final estimated facies model. Comparing the results from the ANN with the well cuttings (master logs) a very good match was found as seen in Figure 3.7 and Appendix.

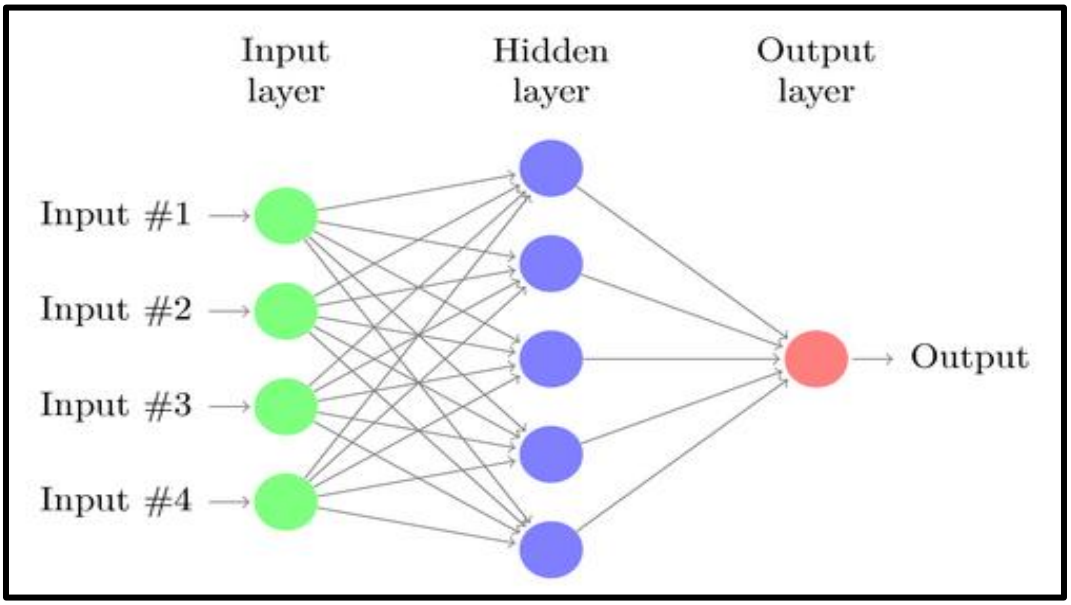

Figure 3.6 An artificial neural network is an interconnected group of nodes

	GR	DT	RHOZ	NPHI	RLA5
GR	1.0000	0.2741	0.2321	0.0870	0.0164
DT	0.2741	1.0000	0.4654	0.5622	0.5670
RHOZ	0.2321	0.4654	1.0000	0.1586	0.0517
NPHI	0.0870	0.5622	0.1586	1.0000	0.6479
RLA5	0.0164	0.5670	0.0517	0.6479	1.0000
Total	0.3298	0.7559	0.5359	0.6897	0.7229

Table 3.3 The correlation analysis of the selected input data (gamma ray (GR), sonic (DT), density (RHOZ), neutron porosity (NPHI), and deep resistivity (RLA5) logs)

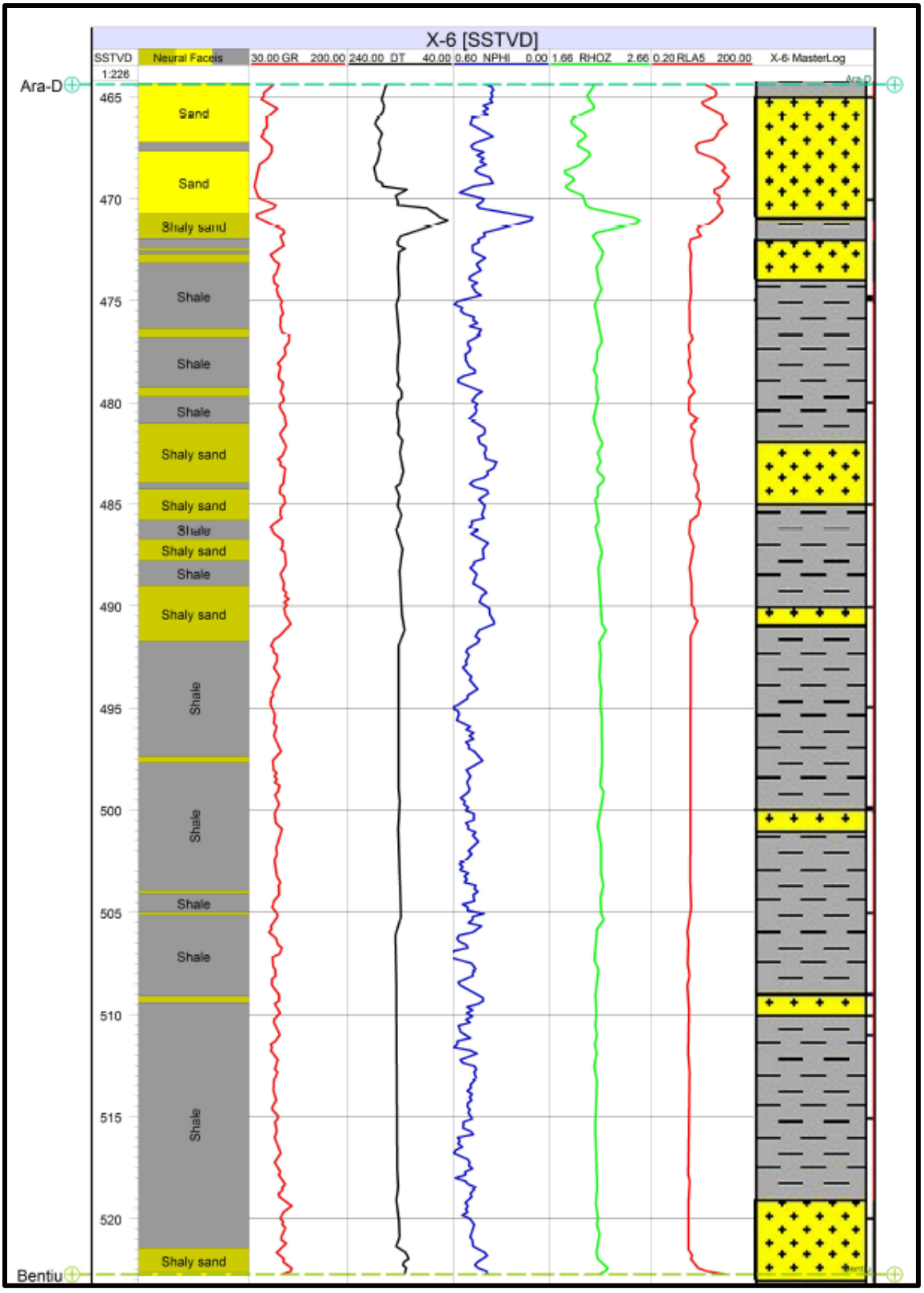

Figure 3.7 Neural network results (on the left) for lithology identification on the basis of gamma ray (GR), sonic (DT), neutron porosity (NPHI), bulk density (RHOZ), and deep resistivity (RLA5) logs. There is a very good fitting with the well cutting description from master logs (on the right).

3.7 Univariate Analysis

Univariate analysis of single observed helps us to explore and interpret the available data and provides an overall picture of their reliability.

This analysis provides statistics such as mean, median, and mode which measure central tendency of a variable, and variance, standard deviation which measures dispersion. Typically, the analyzed data may be plotted as histograms to see their distribution.

For example, let (Z) represent a collection of N amplitude values, Z= (z_1, z_2,…, z_N). If we sort the values from smallest to largest we can estimate the central value or the median.

The statistic most commonly used to summarize where the centre of a distribution lies is the mean, which is simply the arithmetic average of the data values:

$$Mean = m = \frac{1}{N}\sum_{i=1}^{N} z_i \tag{3.16}$$

Though the mean is the traditional measure of the center of a distribution, it is strongly influenced by erratic high values and may not correspond to our intuitive sense of the "centre" of the distribution. Taken together, the mean and the median provide an indication of the influence of extreme values in a data set. If these two measures are close to each other, then extreme values do not play much of a role.

The statistics that are used to describe the location of other parts of the distribution can all be calculated easily from a sorted list of the data values. The minimum is the first on the sorted list and the maximum is the last value on the sorted list. The “quartiles” provide

two other useful measures of location. In the same way that the median splits the data set into halves, the quartiles split it into quarters. 25% of the data values are below the lower (or first) quartile and 25% of them are above the upper (or third) quartile.

In addition to describing where the centre of the distribution lies, a complete statistical description should also report how the data values are spread around the center (are they all tightly grouped close to the center or are they scattered far away from the centre?). The statistics that are commonly used to describe the spread of the distribution are the variance (σ^2) and the standard deviation (σ). The sample variance is the average squared difference of the data values from their mean:

$$Variance = \sigma^2 = \frac{1}{N}\sum_{i=1}^{N}(z_i - m)^2 \qquad (3.17)$$

The standard deviation is the positive square root of the variance.

In this study I conducted univariate statistical analysis for porosity, permeability, and water saturation logs, (Figures 3.8 - 3.11). Table 3.4 shows the porosity, permeability, and water saturation statistical parameters for Aradeiba-D zone.

Statistical Parameters	**Porosity**	**Permeability**	**Water Sat.**
Mean	0.0779	762	0.6793
Minimum	0.00	0.00	0.004
Maximum	0.6400	12000	1.00
Standard Deviation	0.0934	3660	0.2286
Variance	0.0087	13393108	0.0523

Table 3.4 The porosity, permeability, and water saturation statistical parameters for the Aradeiba-D zone

Figure 3.8 shows that the shale facies have the highest percentage (about 55%) among the other facies in the Aradeiba-D Member. Figure 3.9 shows the porosity distribution of the raw well log data which is skewed to the left with low mean porosity. Permeability distribution, (Figure 3.10), is the same as porosity distribution. Figure 3.11 shows the water saturation which is skewed to the right with high mean water saturation.

By comparing porosity, permeability, and water saturation, (Figure 3.12), distributions with each facies distribution, a clear relationship among them and depositional facies appear. For example, in sand facies, porosity distribution tends to have normal distribution with high mean. In shaly sand facies, the porosity distribution tends to be skewed with moderate mean porosity. In the dominated facies, shale, the porosity tends to be skewed with very low mean porosity. The same behavior is noticed in the permeability and water saturation distribution.

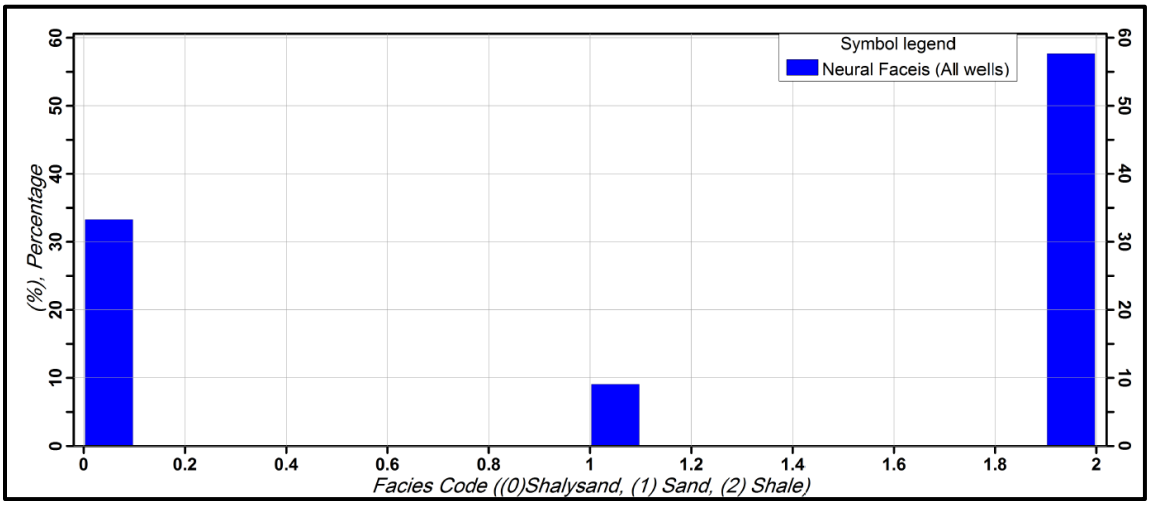

Figure 3.8 Facies distribution within the Aradeiba-D zone from well logs

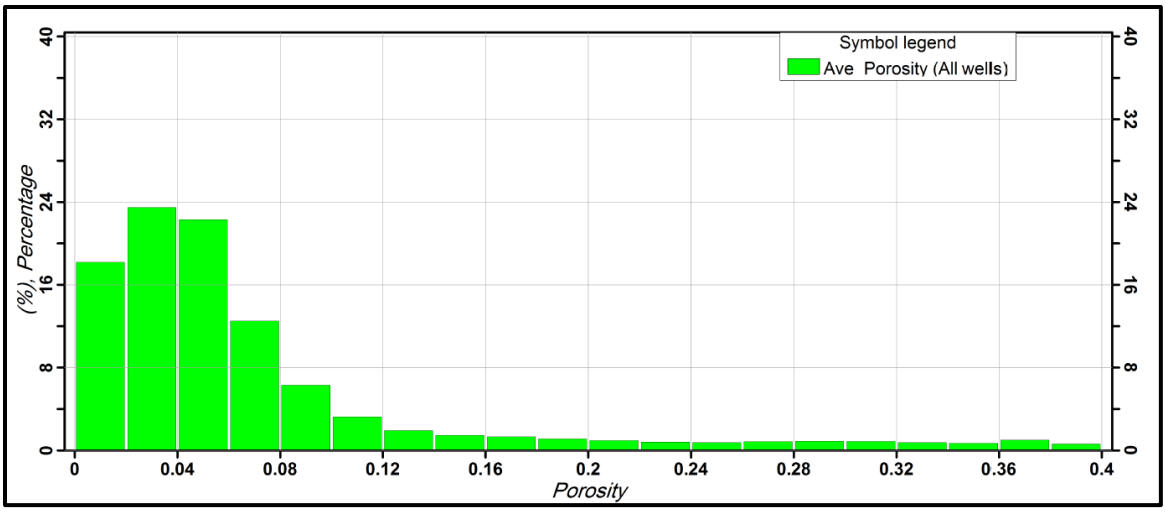

Figure 3.9 Porosity distribution within the Aradeiba-D zone from well logs

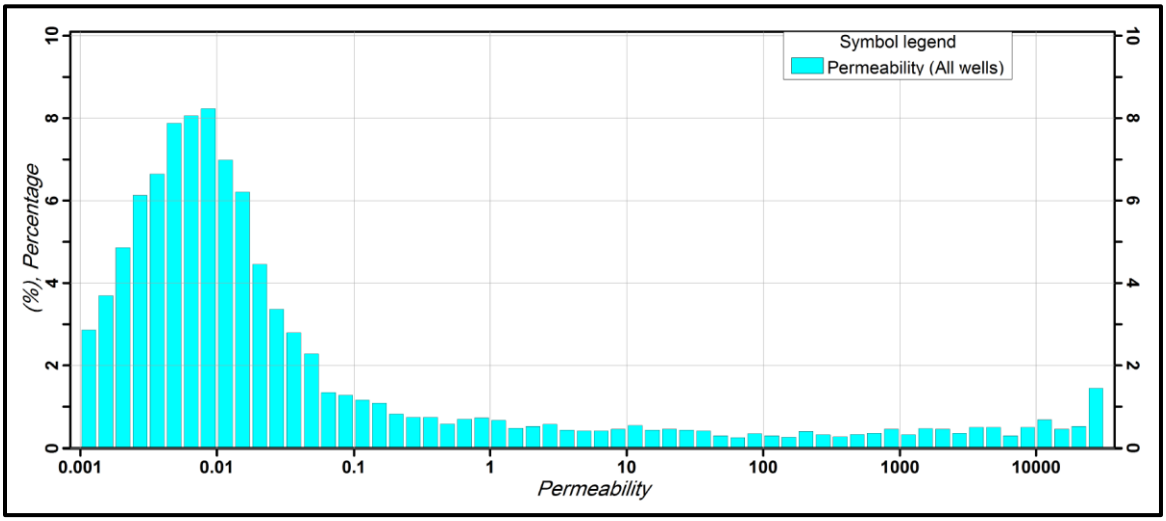

Figure 3.10 Permeability distribution within the Aradeiba-D zone from well log

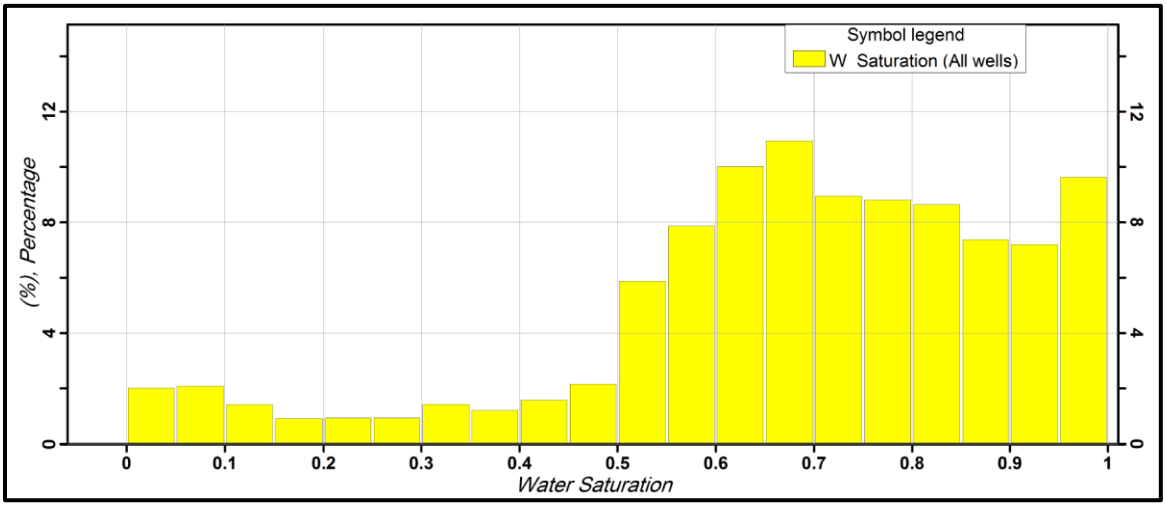

Figure 3.11 Water saturation distribution within the Aradeiba-D zone from well logs

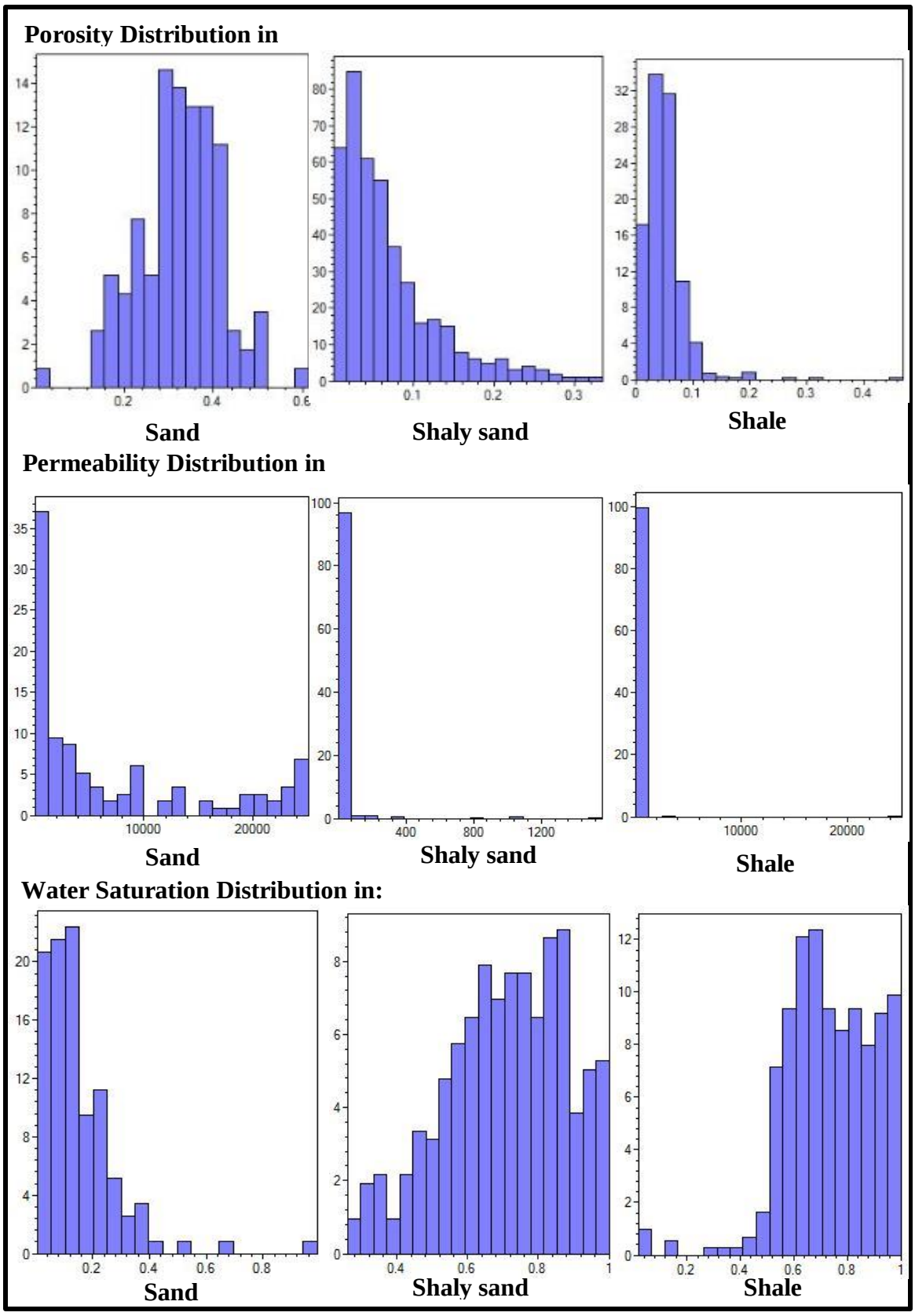

Figure 3.12 Porosity, Permeability, and Water Saturation distribution histograms for each facies in the Aradeiba-D

CHAPTER 4

MULTI-ATTRIBUTE TRANSFORMS

4.1 Introduction

Petroleum reservoir characterization is, in general, the process of describing the variations of reservoir rock properties in different dimensions using various geological, geophysical, petrophysical, and petroleum engineering information. This variation in reservoir parameters may provide us with the amount and degree of heterogeneity in 2-dimensions (2-D) and 3-dimensions (3-D), Chopra and Michelena (2011).

A number of research papers and textbooks focusing on reservoir geophysics have appeared in the literature since early 1990s. Sheriff (1992) compiled and edited a series of reservoir geophysics studies using worldwide datasets, which illustrated the potential contributions in helping to make better development and production decisions. In most general terms, seismic attributes are defined as mathematical transformations of seismic data. Taner et al. (1979) defined seismic attributes as “all the information obtained from seismic data, either by direct measurements or by logical or experience based reasoning”. Since then seismic attributes have become one of the most commonly used and powerful qualitative interpretation techniques. Since the early 1990s, the quantitative analysis of seismic attributes has become widely used and applied through calibration with well-bore measurements {Doyen (1988); Schultz et al. (1994); Taner et al. (1994); Trappe and

Hellmich, (1998)}. Since then, attributes have played an important role in reservoir evaluation studies, or reservoir property mapping, through the extraction of the maximum information from 3D seismic data, where the derived seismic attributes are linked (or correlated) to reservoir properties to obtain useful geological maps.

Many examples are found in the literature related to seismic attributes and their applications to reservoir development and exploration such as Brown (1996; 2001); Taner et al. (1979);), Gastaldi et al. (1997), Hampson et al. (2001), Walker et al. (2005), Sukmono (2007), Pavanel et al. (2009) , Sattar et al. (2010) , Eftekharifar and Han (2011).

In this chapter I report how I have used the multi-attributes analysis technique to generate pseudo-log cubes of facies, porosity, permeability, and water saturation which were then utilized to map the sands and shales of the Aradeiba-D Member and relate the sand and the shale to their porosities, permeabilities, and water saturations. The main tools and steps involved in the study are discussed below.

4.2 Multi-Attribute Background

4.2.1 Seismic Attributes

Seismic Attributes are mathematical transforms, generally non-linear, of a seismic trace. The methodology is aimed to derive statistical, rather than deterministic, relationships between seismic attributes and reservoir parameters at well locations and apply this relationship to whole 2D or 3D seismic cube. Because of the non-linear relationship the predictive power between attributes and the reservoir parameter will be increased. The idea of using multiple seismic attributes to predict log properties was first proposed by Schultz et al. in a series of three articles (1994). Seismic attributes were divided into two categories by Chen and Sidney (1997):

1. Horizon-based attributes, where the average properties of the seismic trace is computed between two geologic boundaries generally defined by picked horizons (e.g., average porosity between two horizons).
2. Sample-based attributes, where input seismic traces are transformed in such a way as to produce another output trace with the same number of samples as the input, i.e. calculated from the trace on a sample-by sample basis, (e.g., amplitude envelope). Only sample-based attributes are considered in this study.

In this study I used a multi-attribute program (*EMERGE*) which groups the internal attributes into six categories, instantaneous attributes, windowed frequency attributes, filter slice, derivative attributes, integrated attributes and time (linear ramp):

❖ **Instantaneous Attributes:**

Seismic attributes have different mathematical representations. The most well-known set of attributes in seismic analysis (based on the *complex trace*) were first discussed by Taner et al. (1979), where they provided the initial formulation of seismic attributes as applied to seismic data interpretation. Instantaneous Attributes were introduced by Taner et al. (1979). They are computed from the complex trace, C(t), which is composed of the seismic trace, s(t) and its Hilbert transform, h(t), which is like a 90° phase shifted trace. Writing the complex trace in polar form, as shown below, gives us the two basic attributes: the amplitude envelope, $A(t)$ and instantaneous phase, $\varphi(t)$. (Note that the term instantaneous amplitude is used synonymously with amplitude envelope.)

$$C(t) = s(t) + ih(t) \tag{4.1}$$

$$= A(t)\exp\big(i\varphi(t)\big)$$

$$= A(t)\cos\varphi(t) + iA(t)\sin\varphi(t)$$

$where: i = \sqrt{-1}$

$$A(t) = \sqrt{s(t)^2 + h(t)^2} \tag{4.2}$$

$and:$ $$\varphi(t) = \tan^{-1}\left[\frac{h(t)}{s(t)}\right] \tag{4.3}$$

A third basic attribute is the instantaneous frequency, which is the time derivative of the instantaneous phase.

$$\omega(t) = \frac{d\varphi(t)}{dt} = The\ instantaneous\ frequency \tag{4.4}$$

The above three instantaneous attributes (amplitude, phase, and frequency) are the primary seismic attributes. The other instantaneous attributes in EMERGE are combinations of these three basic attributes, as shown below:

$$\cos\varphi(t) = cosine\ instantaneous\ phase,$$

$$A(t)cos\varphi(t) = amplitude\ weighted\ cosine\ phase,$$

$$A(t)\varphi(t) = amplitude\ weighted\ phase,$$

$$A(t)\omega(t) = amplitude\ weighted\ frequency.$$

Finally, the apparent polarity attribute is the amplitude envelope multiplied by the sign of the seismic sample at its peak value, applied in a segment between the troughs on either side of this peak. Positive or negative sign is assigned assuming a zero-phase wavelet and a positive or negative reflection coefficient, respectively.

❖ **Windowed Frequency Attributes**

In this process, the Fourier transform of each seismic trace is taken over a 64 sample window (the default). From this window, either the average frequency amplitude or the dominant frequency amplitude is chosen and this value is placed at the centre of the window. A new window is then chosen 32 samples later (the default) and the new frequency attribute is calculated and so on.

❖ **Filter Slice Attributes**

A third set of attributes is comprised of narrow band filter slices of the seismic traces. The following 6 slices are used:

- ✓ 5/10 – 15/20 Hz
- ✓ 15/20 – 25/30 Hz
- ✓ 25/30 – 35/40 Hz
- ✓ 35/40 – 45/50 Hz
- ✓ 45/50 – 55/60 Hz
- ✓ 55/60 – 65/70 Hz

❖ **Derivative Attributes**

Derivative attributes are based on the first and the second derivative of the input seismic trace or its amplitude envelope. The derivatives are calculated numerically:

$$d1_i = \frac{S_i - S_{i-1}}{\Delta t}, \tag{4.5}$$

$$d2_i = \frac{d_i - d_{i-1}}{\Delta t} = \frac{S_i - 2S_{i-1} - S_{i-2}}{\Delta t^2} \tag{4.6}$$

where S_i = the ith seismic or amplitude envelope sample, $d1_i$ = the ith first derivative, $d2_i$ = the ith second derivative and Δt = the sample rate.

❖ **Integrated Attributes**

Integrated attributes are based on the integrated seismic trace or its amplitude envelope. The integrated values are calculated using the following equation:

$$I_i = S_i + I_{i-1} \tag{4.7}$$

where S_i = the ith seismic or amplitude envelope sample, I_i = the integrated value.

This seismic attribute is derived by computing first the running sum of the input trace. At the end of the running sum the integrated seismic trace is filtered by running a default 50 point smoother along it and removing the resulting low frequency trend. The integrated amplitude envelope is normalized by dividing by the difference between the minimum and maximum samples over the total number of samples.

❖ **Time Attribute**

The last attribute is the time attribute. This is simply the time value of the seismic trace and thus forms a "ramp" function that can add a trend to the computed reservoir parameter.

In addition to the above attributes, other external attributes (computed outside the *EMERGE* statistical multi-attribute program, such as the seismic inversion or acoustic impedance attribute) are integrated and combined to improve the resolution power of the predicted reservoir property models. However in this study, I only used the internal attributes.

4.2.2 Conventional Crossplotting (Single Attribute)

The methodology aims to find a relationship between the target log (in my case facies, porosity, permeability, or water saturation logs) and a combination of attributes of the seismic trace. Thus the simplest procedure for deriving the desired relationship between target data and seismic attribute is to crossplot the two. The simple linear relationship between the target log and the seismic attribute uses the linear regression fit in the form of linear equation (equation (4.8)) where the correlation coefficient parameter and conventional cross-plotting are introduced.

$$y = a + bx \tag{4.8}$$

where b is the gradient (or slope) and a is the intercept of the line plotted in a graphical cross-plot analysis. These parameters may be derived by minimizing the mean-squared prediction error:

$$E^2 = \frac{1}{N}\sum_{i=1}^{N}(y_i - a - bx_i)^2 \tag{4.9}$$

where the sum is over all points in the crossplot.

The calculated prediction error E is a measure of the goodness-of-fit for the regression line defined by equation (4.8) between the actual target log and the predicted target log. An alternative measure is the normalized correlation coefficient, defined by

$$\rho = \frac{\sigma_{xy}}{\sigma_x \sigma_y} = \text{The correlation coefficient} \tag{4.10}$$

where

$$\sigma_{xy} = \frac{1}{N}\sum_{i=1}^{N}(x_i - m_x)\left(y_i - m_y\right) = \text{ Covariance function} \tag{4.11}$$

$$\sigma_x = \frac{1}{N}\sum_{i=1}^{N}(x_i - m_x)^2 = \text{Standard Deviation} \tag{4.12}$$

$$\sigma_y = \frac{1}{N}\sum_{i=1}^{N}\left(y_i - m_y\right)^2 = \text{Standard Deviation} \tag{4.13}$$

$$m_x = \frac{1}{N}\sum_{i=1}^{N} x_i = \text{Arithmetic Average} \tag{4.14}$$

$$m_y = \frac{1}{N}\sum_{i=1}^{N} y_i = \text{ Arithmetic Average} \tag{4.15}$$

4.2.3 Multivariate Linear Regression (Multi-Attributes)

An extension of the conventional cross plot is to use multiple attributes (multivariate linear regression) which was discussed and derived mathematically by Hampson et al. (2001). If there are (M) attributes, $A_1, A_2, \cdots, A_M$, to predict the log (L), one must determine the M +1 weights, $w_0, w_1, \cdots, w_M$, which, when multiplied by the particular set of attribute values, gives the closest agreement with the log in a least-squared sense. For simplicity, assume that M =3 as shown in (Figure 4.1a). At each time sample, the target log (reservoir property) is modeled as a linear combination of several attributes defined by the following linear equation:

$$L(t) = w_0 + w_1 A_1(t) + w_2 A_2(t) + w_3 A_3(t) \tag{4.16}$$

If we have N samples in our log, we can then write the following set of equations:

$$\begin{aligned} L_1 &= w_0 + w_1 A_{11} + w_2 A_{21} + w_3 A_{31} \\ L_2 &= w_0 + w_1 A_{12} + w_2 A_{22} + w_3 A_{32} \\ &\vdots \\ L_N &= w_0 + w_1 A_{1N} + w_2 A_{2N} + w_3 A_{3N} \end{aligned} \tag{4.17}$$

where A_{ij} is the jth sample of the ith attribute.

Equation (4.17) may be rewritten in matrix form as

$$L = A\,W \tag{4.18}$$

Where (**L**) is an (N×1) matrix containing the known well-log values, **A** is an (N×4) matrix containing the seismic attribute values; and **W** is a (4×1) matrix with unknown weights. Multiplying both sides of equation (4.18) by the matrix transpose (A^T), equation (4.18) may be rewritten as

$$A^T L = A^T A W \tag{4.19}$$

Equation (4.19) is a very powerful equation that is used throughout geophysical analysis. This can be solved by least-squares minimization to give

$$W = (A^T A)^{-1} A^T L \tag{4.20}$$

The mean-squared prediction error is computed using the derived weights as follows

$$E^2 = \frac{1}{N}\sum_{i=1}^{N}(L_i - w_0 - w_1 A_{1i} - w_2 A_{2i} - w_3 A_{3i})^2 \tag{4.21}$$

The mean squared error (4.21) calculated using the derived weights constitutes a measure of goodness-of-fit for the derived transform, as does the normalized statistical correlation coefficient.

4.2.4 Convolutional Operator

The Multi-attribute analysis correlates each target sample with the corresponding samples of the seismic attributes. This approach is limited because it ignores the fact that there is a big difference in frequency content between logs and seismic data. The convolutional operator extends the cross plot regression to include neighboring samples. Each target sample is predicted using a weighted average of a group of samples on each attribute as shown in (Figure 4.1b). The weighted average is convolution. Equation (4.16) is now replaced by:

$$L = w_0 + w_1 * A_1 + w_2 * A_2 + w_3 * A_3 \tag{4.22}$$

where * represents convolution by an operator. Note that the number of coefficients has now increased to (number of attributes times operator length)+1.

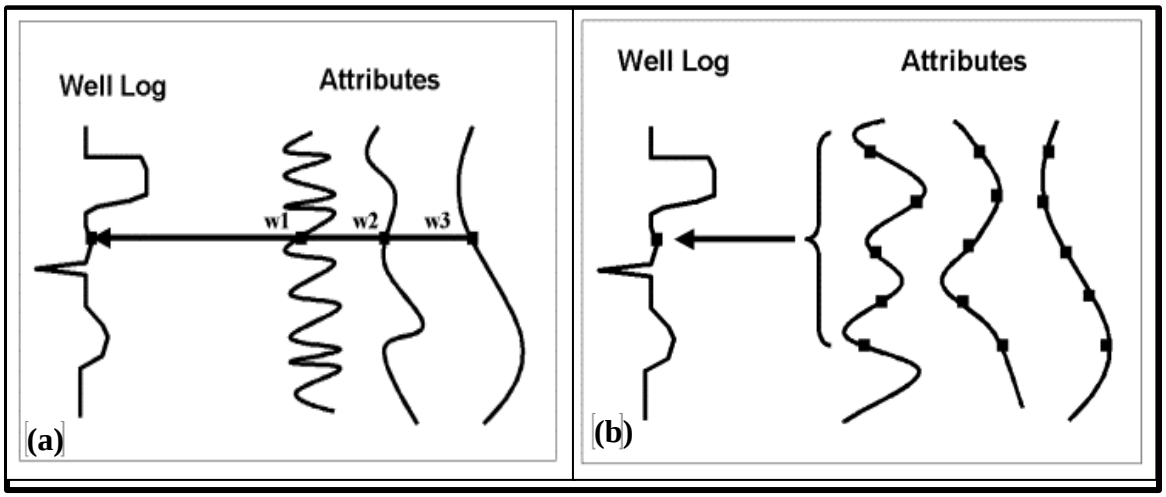

Figure 4.1 (a) Three seismic attributes case, each target log sample is modeled as a linear combination of attribute samples at the same time. (b) Using a five-point convolutional operator to relate the seismic attributes to the target log, Hampson et al. (2001)

Once again, the operator coefficients may be derived by minimizing the mean-squared prediction error:

$$E^2 = \frac{1}{N}\sum_{i=1}^{N}(L_i - w_0 - w_1 * A_{1i} - w_2 * A_{2i} - w_{3*}A_{3i})^2 \qquad (4.23)$$

Using the convolutional operator is like adding more attributes. It always improve the prediction error, but the validation error may not improve (the danger of over-training is increased) which will be discussed in the following paragraphs.

4.2.5 Stepwise Regression

The process of step-wise regression (Draper and Smith, 1966) implemented in the Hampson-Russell *EMERGE* program finds a combination of an optimal number of seismic attributes best predicting the target reservoir property. This process is as follows:

Step 1: First, the single best attribute is found by exhaustive search through a trial and error process by computing the prediction error for each attribute and ranking them from best (lowest error) to worse (highest error). Suppose the best attribute that is the one with lowest prediction error is attribute$_1$.

Step 2: Find the best pair of attributes, assuming that the first member is attribute$_1$. Again, we solve for the optimal coefficients and calculate the prediction error. The best pair is the one with the lowest prediction error. Call this second attribute attribute$_2$.

Step 3: The best triplet of attributes is then derived, assuming that the first two members are attribute$_1$ and attribute$_2$, represented by the lowest prediction error. The best triplet is the one with the lowest prediction error. Call the corresponding third attribute attribute$_3$. This process can be carried on as long as desired.

The prediction error, E_N, for N attributes is always less than or equal to the prediction error, E_{N-1}, for N-1 attributes, no matter which attributes are used.

4.2.6 Validation of Attributes (Cross-Validation Test)

Adding attributes is similar to fitting a curve through a set of points, using polynomials of increasing order. For each polynomial, the prediction error can be calculated, as the root mean square difference between the actual and predicted values.

By increasing the order of the polynomial, the prediction error will always decrease. The problem is that although the higher-order polynomial has better prediction of the training data, but it is worse at interpolating or extrapolating beyond the limits of the data, (Figure 4.2), in other words it is "over-trained", Kalkomey (1997). As shown in (Figure 4.2), a high order polynomial which fits the training data well may still fit the validation data poorly. This indicates that the order of the polynomial is too high.

Thus, to determine the validity of attributes, *EMERGE* uses the following validation procedure:

1. Divide the entire data set into two groups:
   - Training data set
   - Validation data set
2. When determining coefficients by regression, use the training data set.
3. When measuring the prediction error, use the validation data set.

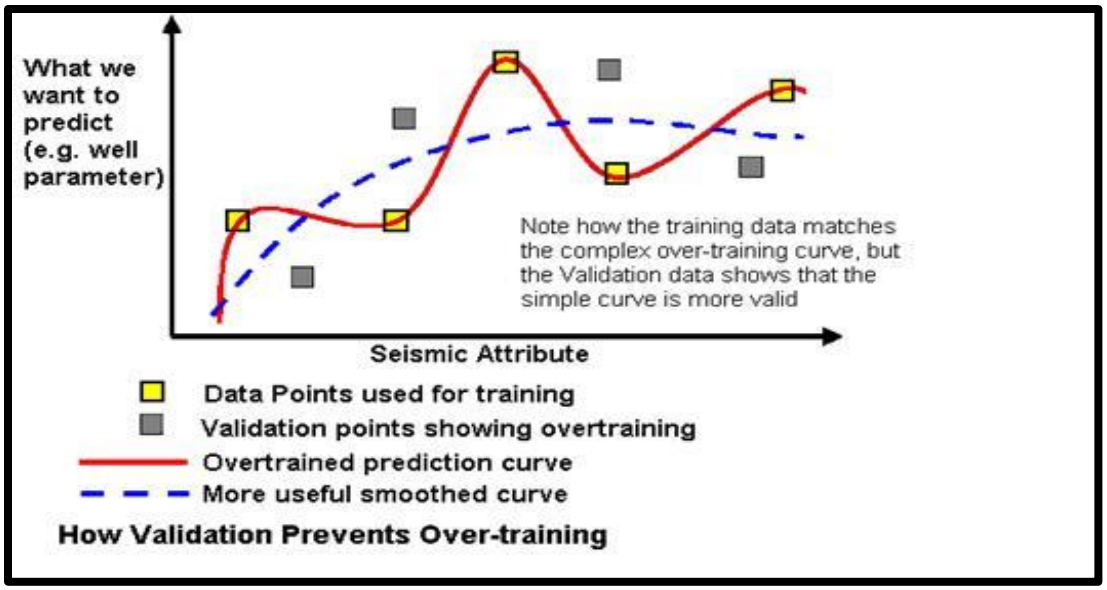

Figure 4.2 How validation prevents over-training, Hampson et al. (2001)

Assume that there are five wells [$Well_1$, $Well_2$, $Well_3$, $Well_4$, and $Well_5$] and three attributes [Impedance, Envelope, Frequency], validation is performed by systematically leaving out wells as follows:

1. Leave out $Well_1$. Solve for the regression coefficients using only data from [$Well_2$, $Well_3$, $Well_4$, and $Well_5$]. This means solving the system of equations in (4.17), where the rows contain no data from $Well_1$.
2. With the derived coefficients, calculate the prediction error for $Well_1$ using equation (4.23) where only data points for $Well_1$ are used. This gives us the validation error for $Well_1$, E_1.
3. Repeat this process for $Well_2$, $Well_3$, etc., each time leaving the selected well out in the calculation of regression coefficients, but using only that well for the error calculation.
4. Calculate the average validation error for all wells:

$$E_A = \frac{1}{N}\sum_{i=1}^{N} E_i = \frac{E_1 + E_2 + E_3 + E_4 + E_5}{5} \quad (4.24)$$

4.3 Multi-Attributes Transforms Analysis and Validation

The database used in this study consisted of a cropped post-stack time-migrated 3-D seismic and wireline logs from 18 wells. The cropped seismic data cover an area about 40.24 km^2 with a bin size of 12.5m × 25.0m and 1-s two-way travel time (TWT) record length. The analyzed digital logs for lithology, porosity, permeability and water saturation were obtained in the early stage of this study (Chapter 3). Sonic logs were available for the 18 wells which were used beside formation tops from seismic and well to tie the well logs to seismic data.

To determine the best seismic material for delineating and mapping facies and petrophysical parameters for the Aradeiba-D Member, I cross-plotted both raw seismic and acoustic impedance (AI) against the porosity, permeability, and water saturation using available well data (See Appendix), but I found either no or very poor relationships. Thus, I used the seismic multi-attribute technique to overcome the problem.

In this chapter, I described how I used the Hampson-Russell *EMERGE* program for building facies and petrophysical models by integrating the analyzed digital logs and 3-D seismic data to directly predict lateral reservoir properties (lithology, porosity, permeability, water saturation) changes within the reservoir. I investigated the relationships between multiple seismic parameters (or attributes) and reservoir properties at all well locations for the Aradeiba-D Member.

Firstly, for each of the 18 wells, a single composite trace has been extracted from the corresponding trace in the 3-D volumes. An example of the training data for four wells is shown in (Figure 4.3). The target (facies, porosity, permeability, and water saturation) logs were converted from depth to time and sampled at the same 1-ms sample rate as the seismic data. The depth to time conversion is critical for this process because the correlations were done over a time window. The analysis window is between the horizontal red lines, it is less than 60-ms.

Then, the target (porosity, permeability, and water saturation) logs were filtered to the seismic frequency bandwidth to improve matching results. Figure 4.4 shows the maximum useful frequency is between 60 and 70 Hz., which was used in filtering of the logs. It was necessary that the target log is usually much higher frequency than the seismic or attributes. Figure 4.5 shows an example of the filtered porosity logs superimposed over the original logs after the highest frequencies have been removed.

For each model from the four, I created two cross sections across the model. Figure 4.6 shows their locations. Also a time slice for the top of the Aradeiba-D has been generated for each model.

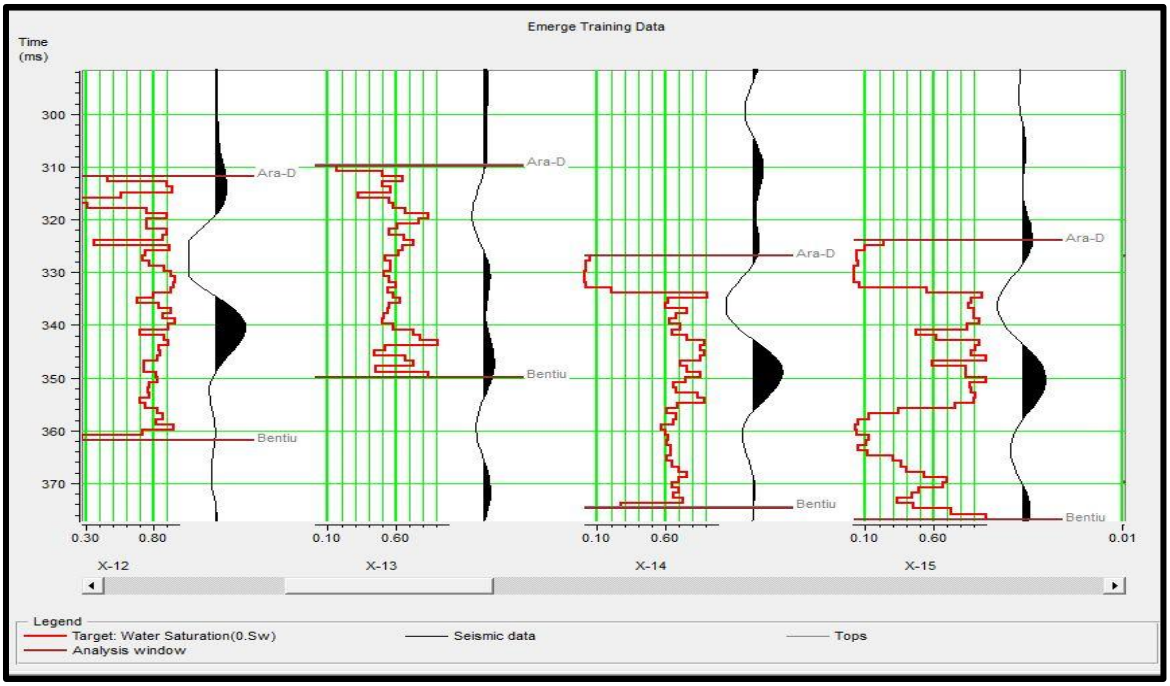

Figure 4.3 An example for water saturation training data from four wells and their corresponding extracted trace. For each well the curve on the left is the water saturation log and on the right is the composite seismic trace from the 3-D volume at the well location. The red lines show the analysis window.

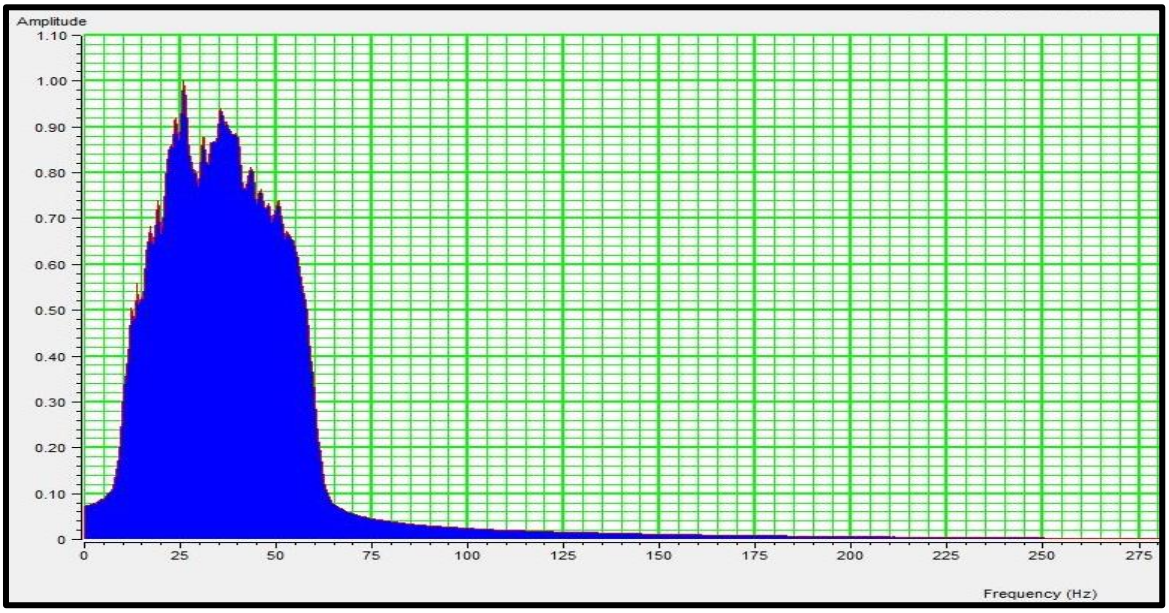

Figure 4.4 The resulting frequency spectrum shows that the maximum useable frequency is between 60 and 70 Hz.

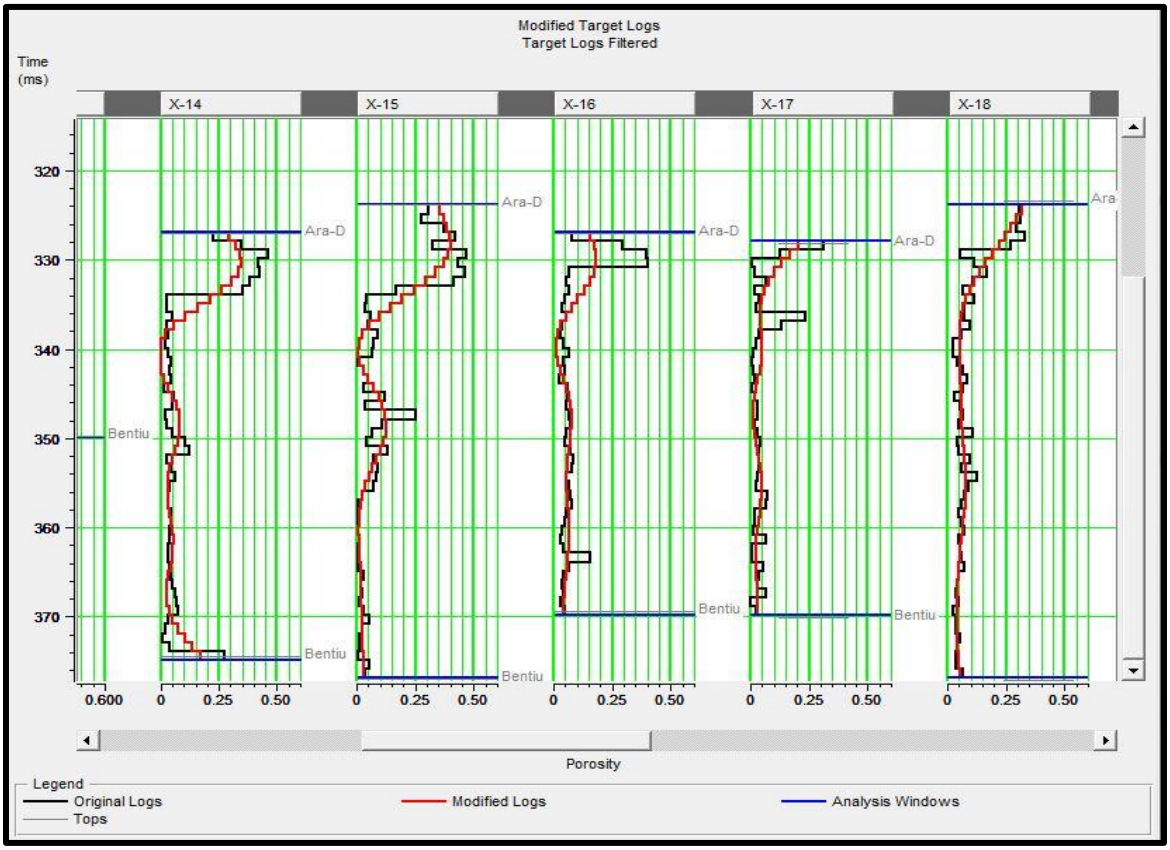

Figure 4.5 An example of filtered porosity logs (in red) over the original logs (in black)

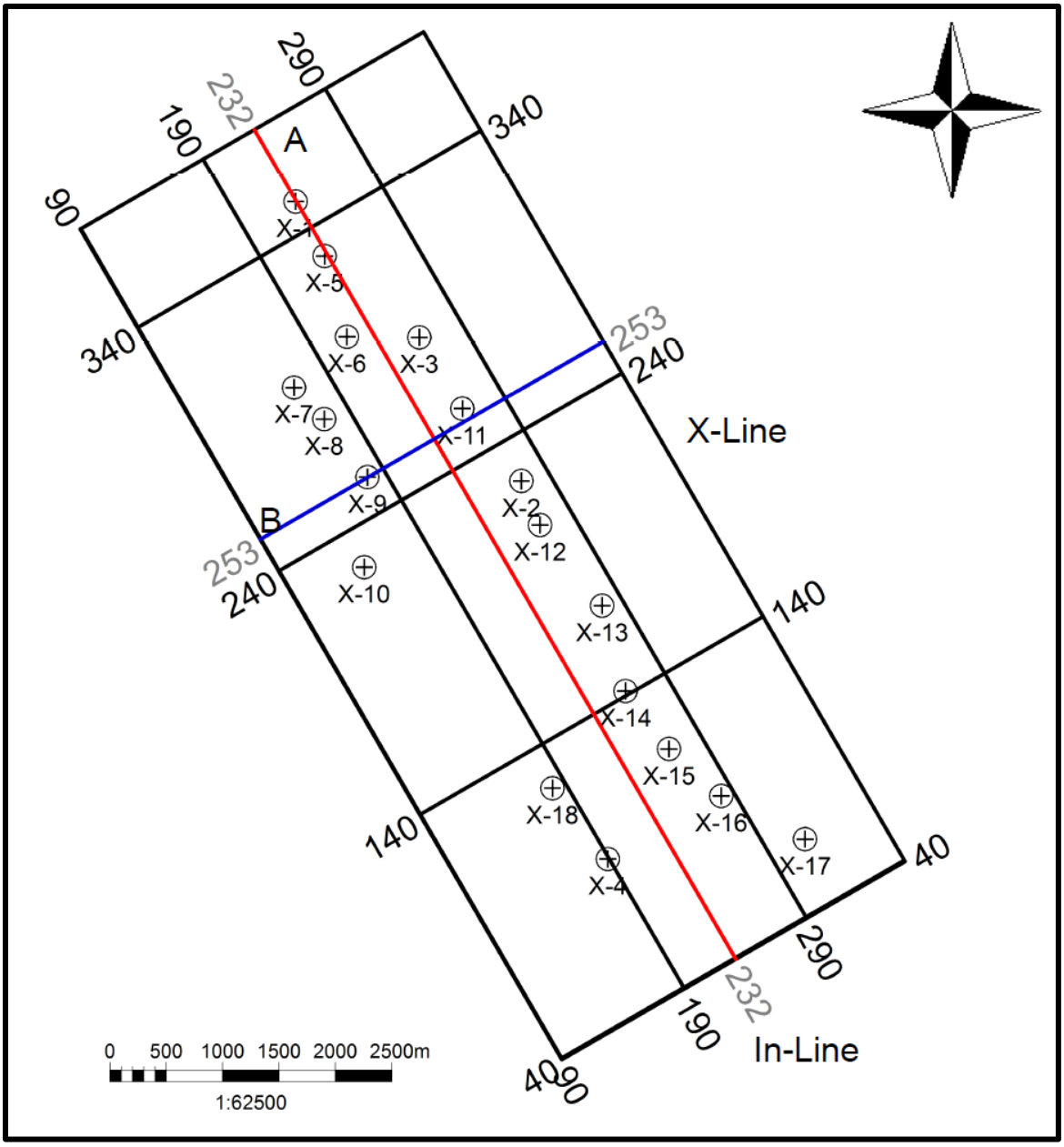

Figure 4.6 Location of cross sections A and B across the study area corresponding to X-line232 and In-Line253, respectively

4.3.1 Facies Modeling

The stepwise regression described earlier (in section 4.2.5) is the first step for the facies analysis. Four attributes were chosen with nine-point convolutional operator as shown in (Figure 4.7-a). These attributes are given in (Table 4.1), each line shows a different multi-attribute transform with the number of attributes listed in the first column. The multi-attribute transform for each line includes all attributes above it. The prediction error for is shown in the last two columns and in (Figure 4.8-a) in the units of the target log (e.g., fractional porosity). The same information is displayed graphically in (Figure 4.7-a), which also shows the training and validation results. The lower curve (in black) is the prediction error when all wells are used in the analysis, which decreases as attributes are added. The upper curve (in red) shows the average validation error, as defined earlier in equation (4.24). I interpret this curve to mean that adding attributes after the fourth over-trains the system.

The methodology checks the validation error of every attribute combination by leaving out one well from the training data set. Then it predicts the excluded one using the rest of the training data and compares the predicted one with the original log and the validation error is computed. Figure 4.8-a, shows the distribution of prediction errors over the 18 wells. The average normalized correlation for all of the wells is 0.39 while validation result for multivariate linear regression is 0.29. The low correlation is interpreted to be related to the high-frequency component in the facies log besides the fact that the facies log is a discrete-valued log, not a continuous one, which led to a poor correlation.

The derived transforms were then applied to the 3-D seismic volume. Figure 4.9 shows the in-line 253 and x-line 232 cross sections for the Aradeiba-D Member. The sand bodies are clearly identified within the shale volume which is the major facies percentage of the Aradeiba-D.

Finally, (Figure 4.14-a) shows a data slice through the computed facies volume. It displays the sand facies value from a 10-ms window centered at the Aradeiba-D marker. We can see clearly the sand bodies trending northwest–southeast and north-south through the volume forming a belt.

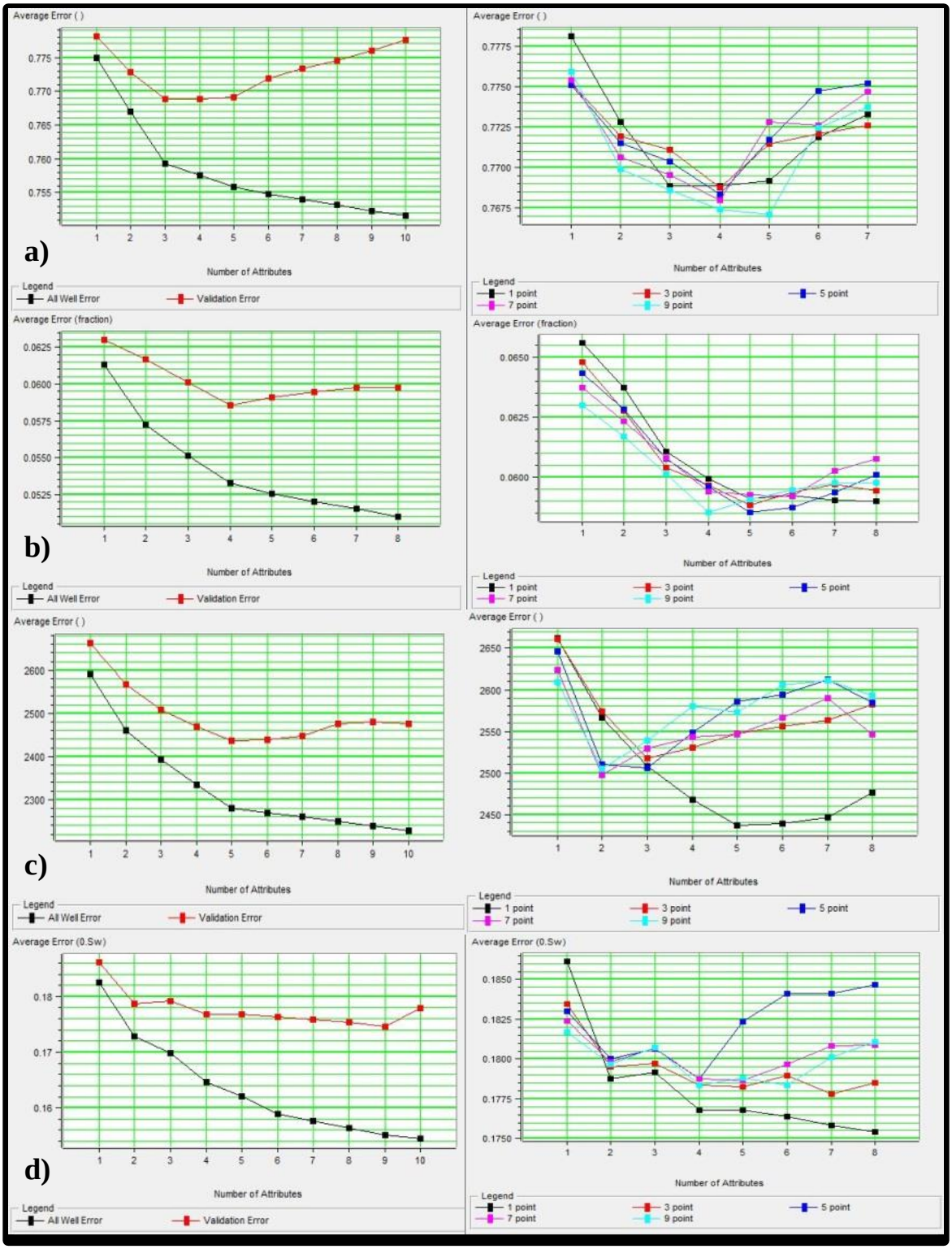

Figure 4.7 Stepwise regression and convolutional operator test results, on the right the validation error plot for 5 different operator lengths and on the left validation and training errors plot for the best combination of convolutional operator points for a) Facies Model b) Porosity Model c) Permeability Model d) Water Saturation Model

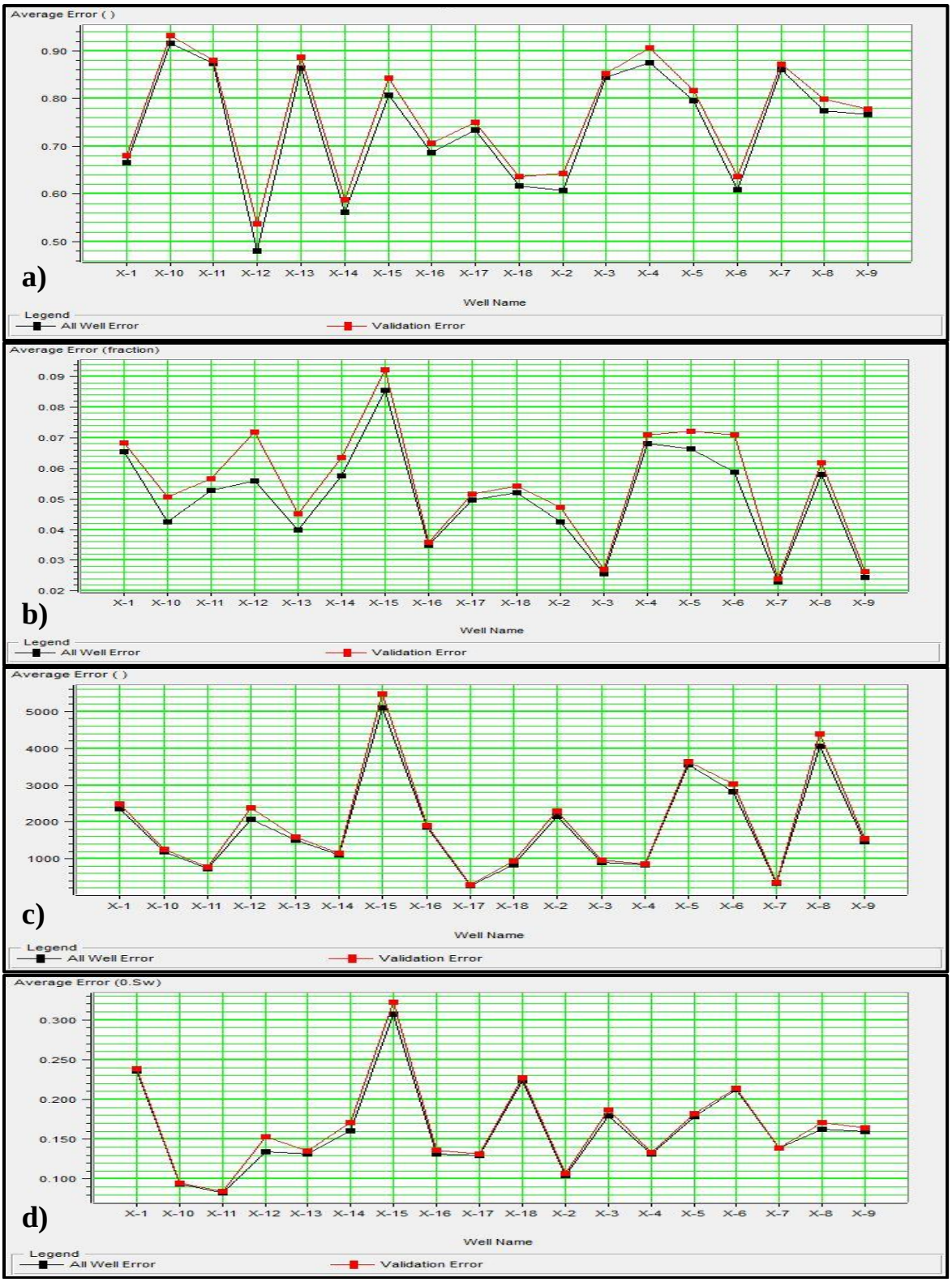

Figure 4.8 The cross-validation results for each of the 18 wells. The lower curve (in black) shows the prediction error when the specified well is used in the analysis. The upper curve (in red) shows the validation error when the well is not used in the analysis. a) Facies Model b) Porosity Model c) Permeability Model d) Water Saturation Model

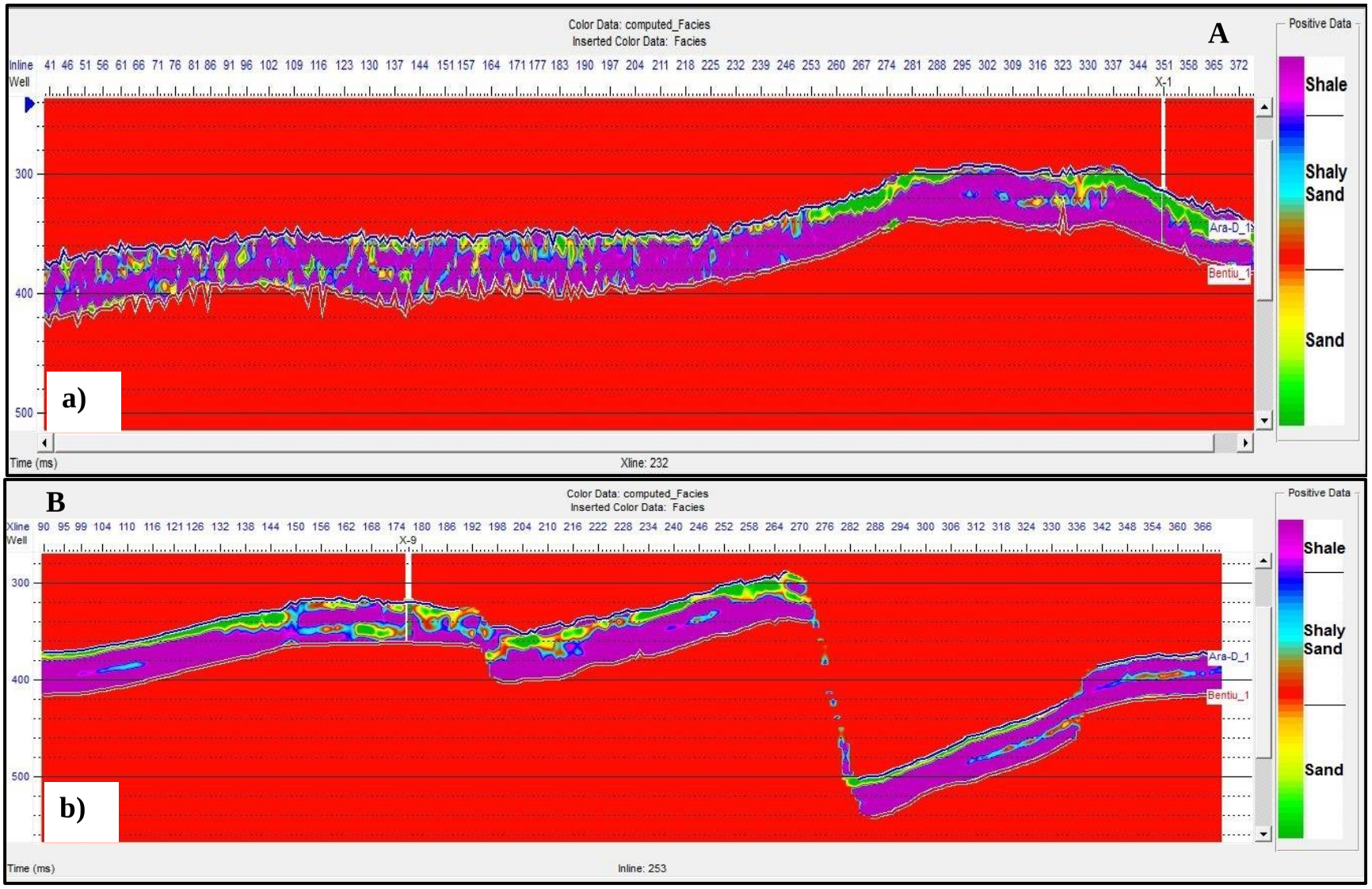

Figure 4.9 The facies distribution cross-sections in time domain a) cross section A along x-line 232 b) cross section B along in-line253. The inserted color log is the target facies log at this location.

4.3.2 Porosity Modeling

I extracted 20 attributes from the seismic volume, then I narrowed that list down to four based on the stepwise linear regression and cross validation error analysis.

These attributes are given in (Table 4.1), along with the associated application (training) error (the average error using 18 wells with average porosity logs that could be accurately tied to the seismic data) and validation error (the average error leaving out one well at a time) which is shown at (Figure 4.8-b). A nine-point convolutional operator was used as shown in Figure 4.7-b.

The coefficient of determination for the linear regression model is R^2 =0.76, with an average error (the root mean squares (RMS) difference between the target log values and the predicted values) of 0.053 (porosity units in fraction), Figure 4.10-a. The validation testing yielded an R^2 of 0.696 with an error of 0.058 (porosity units in fraction).

The derived transforms were then applied to the 3-D seismic volume. Figure 4.11, shows the in-line 253 and x-line 232 cross sections for the Aradeiba-D Member and there is a good match between the inserted wells and the model. The high-porosity zones are clearly identified and correspond to sand bodies, low porosity corresponds to shales.

Finally, to enhance the linear features seen in (Figure 4.14-a), I created an average predicted porosity map of the Aradeiba-D top; Figure 4.14-b. As expected, the linear features are in the same trend as Figure 4.14-a. We can clearly see the good match between sand bodies and the high porosity trending northwest– southeast and north-south through the volume forming a belt like shape while they randomly dispersed in the western and eastern regions.

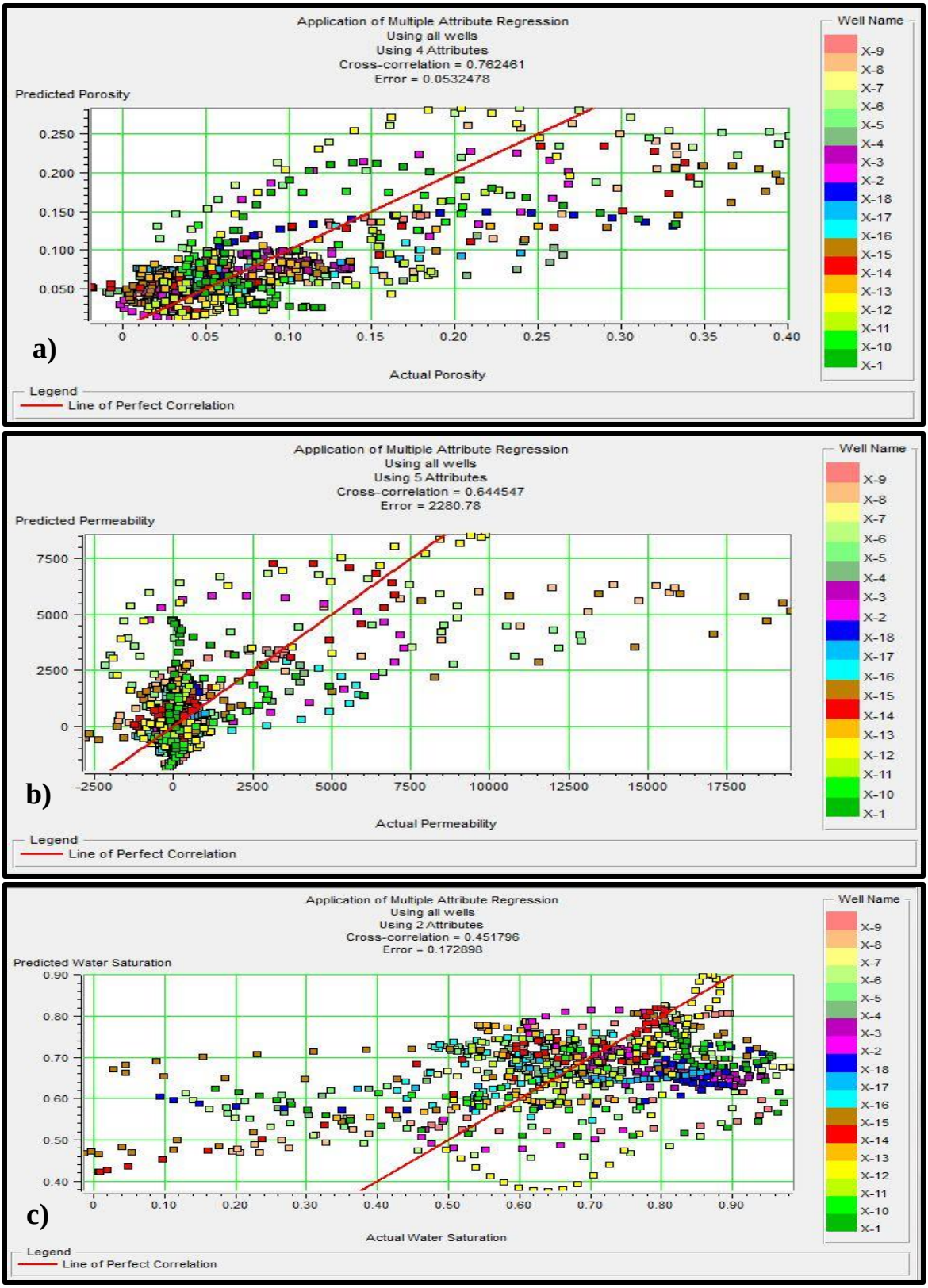

Figure 4.10 Cross-plots of actual target against predicted one, using points within the analysis window from all 18 wells computing the normalized cross-correlation for a) Porosity Model b) Permeability Model c) Water Saturation Model

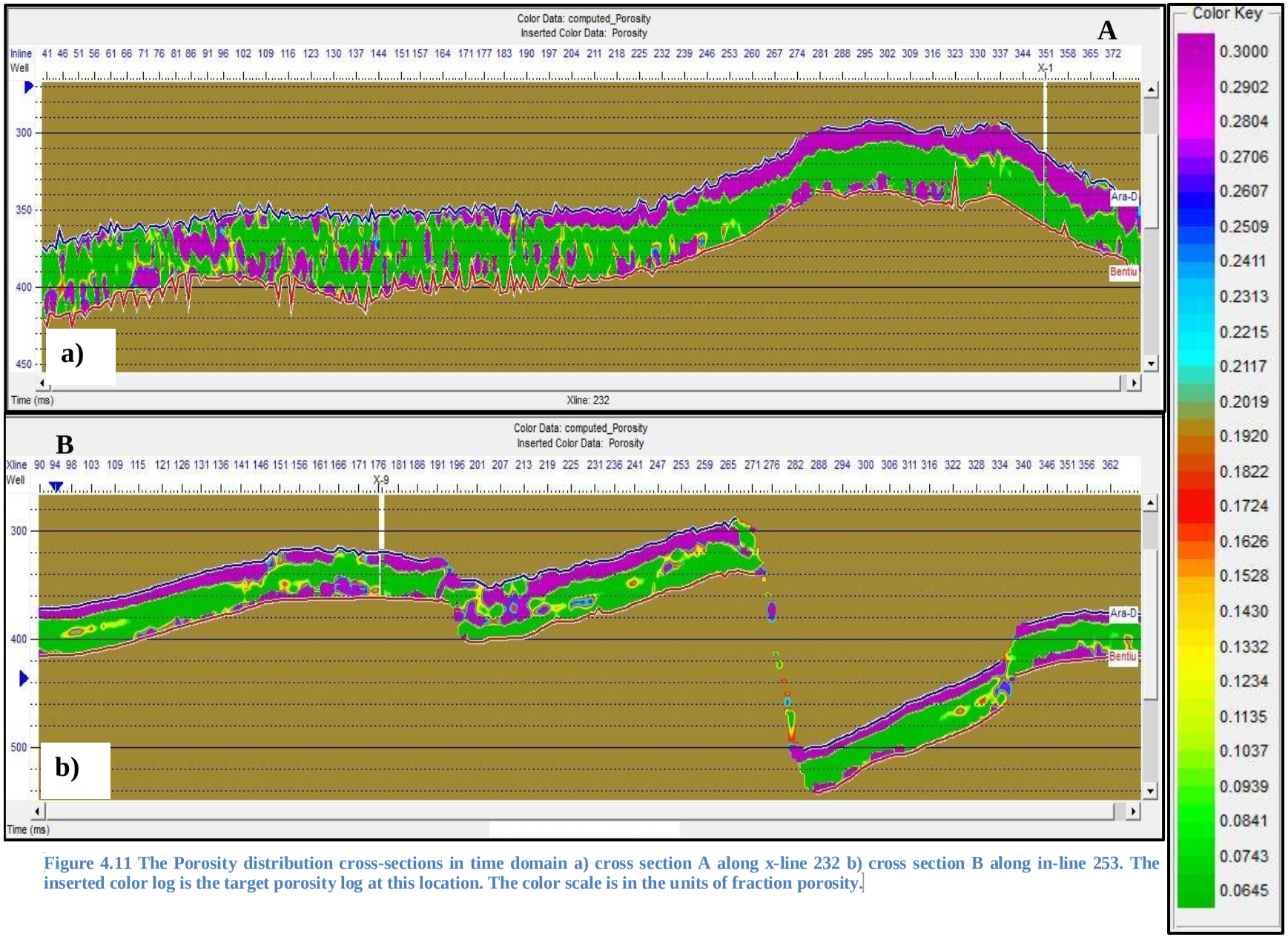

Figure 4.11 The Porosity distribution cross-sections in time domain a) cross section A along x-line 232 b) cross section B along in-line 253. The inserted color log is the target porosity log at this location. The color scale is in the units of fraction porosity.

4.3.3 Permeability Modeling

The attributes were visually examined to get better candidates for the multivariate regression exercise. Based on the stepwise linear regression and cross validation error analysis I used five attributes with one-point convolutional operator was used as shown in Figure 4.7-c.

These attributes are given in (Table 4.1), along with the associated application error (the average error using 18 wells with permeability logs that could be accurately tied to the seismic data) and validation error (the average error leaving out one well at a time) which are shown in Figure 4.8-c.

Then I generated a crossplot and calculated the correlation coefficient for the linear regression model with R^2 =0.64, Figure 4.10-b. The validation testing yielded a correlation coefficient of 0.58.

The derived transforms were then applied to the 3-D seismic volume. Figure 4.12, shows the in-line 253 and x-line 232 cross sections for the Aradeiba-D Member and indicates a poor correlation between the inserted wells and the model. The high-permeability zones are clearly identified and corresponds to sand bodies, the poor permeability to shales. The high permeability zones are continuous and have the same range of permeability and the other models have patches with a large scale of parameter values.

Finally, Figure 4.15-c shows a data slice through the computed permeability volume to enhance the linear features recognition. I created a predicted permeability map of the Aradeiba-D top. As expected, the northwest–southeast and north-south linear features are in the same trend, (Figure 4.14), with the highest values of porosity and permeability and they are randomly dispersed in the western and eastern regions.

No. of Attributes	Final Attribute	Training Error	Validation Error
Target = Facies			
1	Derivative Instantaneous Amplitude	0.774951	0.778124
2	Integrated Absolute Amplitude	0.766959	0.772808
3	Filter 35/40-45/50	0.759351	0.768891
4	Second Derivative	0.757553	0.768883
Target = Porosity			
1	Derivative Instantaneous Amplitude	0.061304	0.063004
2	Second Derivative	0.057205	0.061687
3	Instantaneous Frequency	0.055115	0.060146
4	Filter 5/10-15/20	0.053248	0.058534
Target = Permeability			
1	Derivative Instantaneous Amplitude	2590.8145	2662.5222
2	Integrate	2459.4893	2566.0158
3	Integrated Absolute Amplitude	2392.9773	2468.2213
4	Average Frequency	2333.3706	2468.2213
5	Filter 35/40-45/50	2280.7765	2436.5823
Target = Water Saturation			
1	Derivative Instantaneous Amplitude	0.182453	0.186154
2	Integrate	0.172898	0.178772

Table 4.1 The stepwise regression results, applied to the facies, porosity, permeability, and water saturation prediction problems.

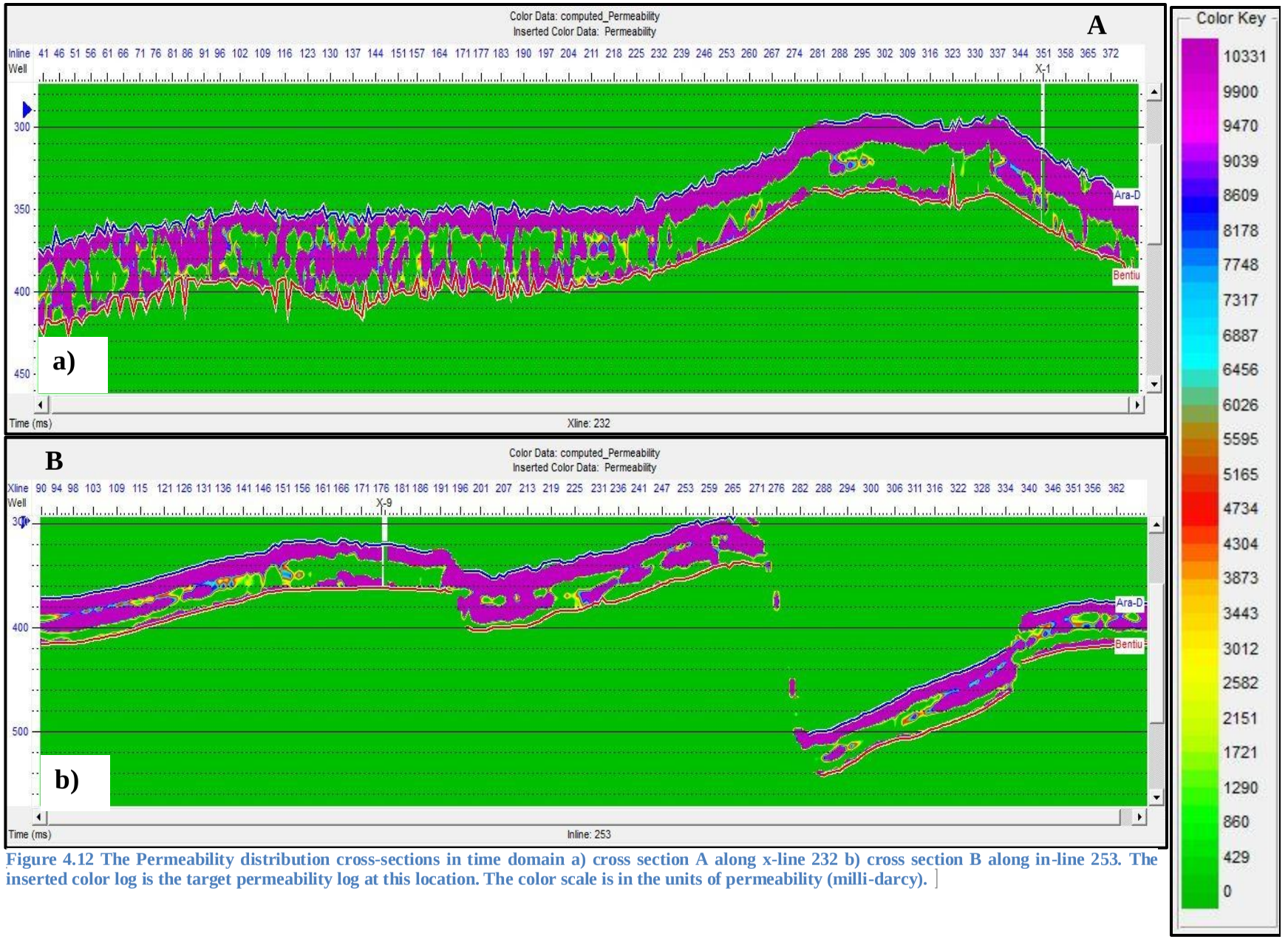

Figure 4.12 The Permeability distribution cross-sections in time domain a) cross section A along x-line 232 b) cross section B along in-line 253. The inserted color log is the target permeability log at this location. The color scale is in the units of permeability (milli-darcy).

4.3.4 Water Saturation Modeling

The same validation procedure as in the previous models was used to determine which and how many, seismic attributes to use for water saturation prediction exercise. Only two attributes with one-point convolutional operator as given and shown in (Table 4.1, Figures 4.7-d and 4.8-d) were used.

Then I generated a cross-plot and calculated the coefficient of determination for the linear regression model which is $R^2 = 0.45$, Figure 4.10-c. The validation testing yielded a correlation coefficient of 0.39. The derived transforms were then applied to the 3-D seismic volume. Figure 4.13, shows seismic in-line 253 and x-line 232 from the 3-D survey that intersects one of the 18 calibration wells. The color curve is the water saturation log for X-9 and X-1 wells respectively. The water saturation distribution well agreed with the previous models and identified sand bodies (low water saturation) and shales (high water saturation)

Finally, Figure 4.15-d shows the minimum water saturation values from a 10-ms window centered at the Aradeiba-D top in time domain. As expected, the northwest–southeast and north-south linear features are in the same trend as (Figure 4.14) with the highest values of porosity and permeability and they are randomly dispersed in the western and eastern regions.

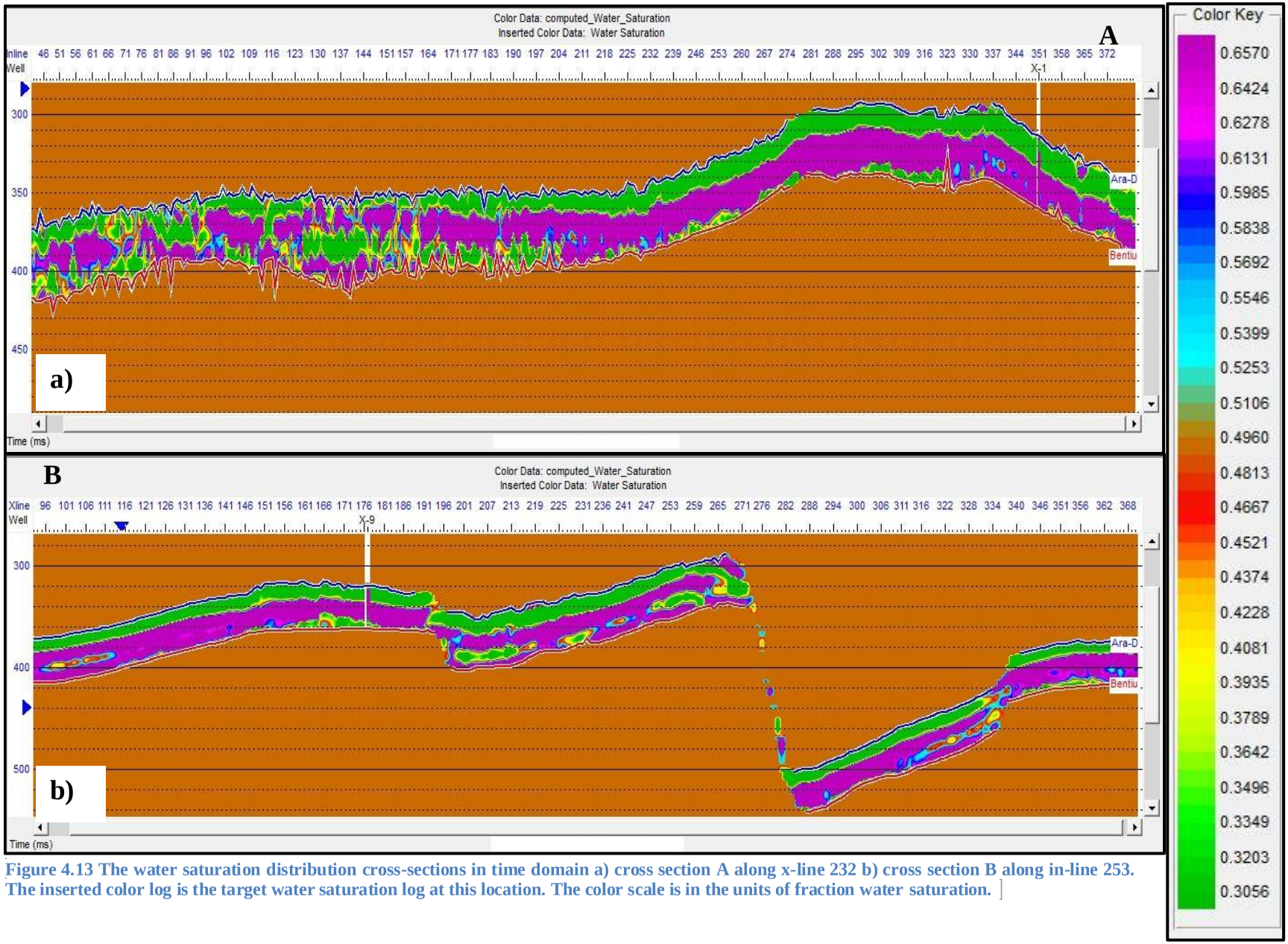

Figure 4.13 The water saturation distribution cross-sections in time domain a) cross section A along x-line 232 b) cross section B along in-line 253. The inserted color log is the target water saturation log at this location. The color scale is in the units of fraction water saturation.

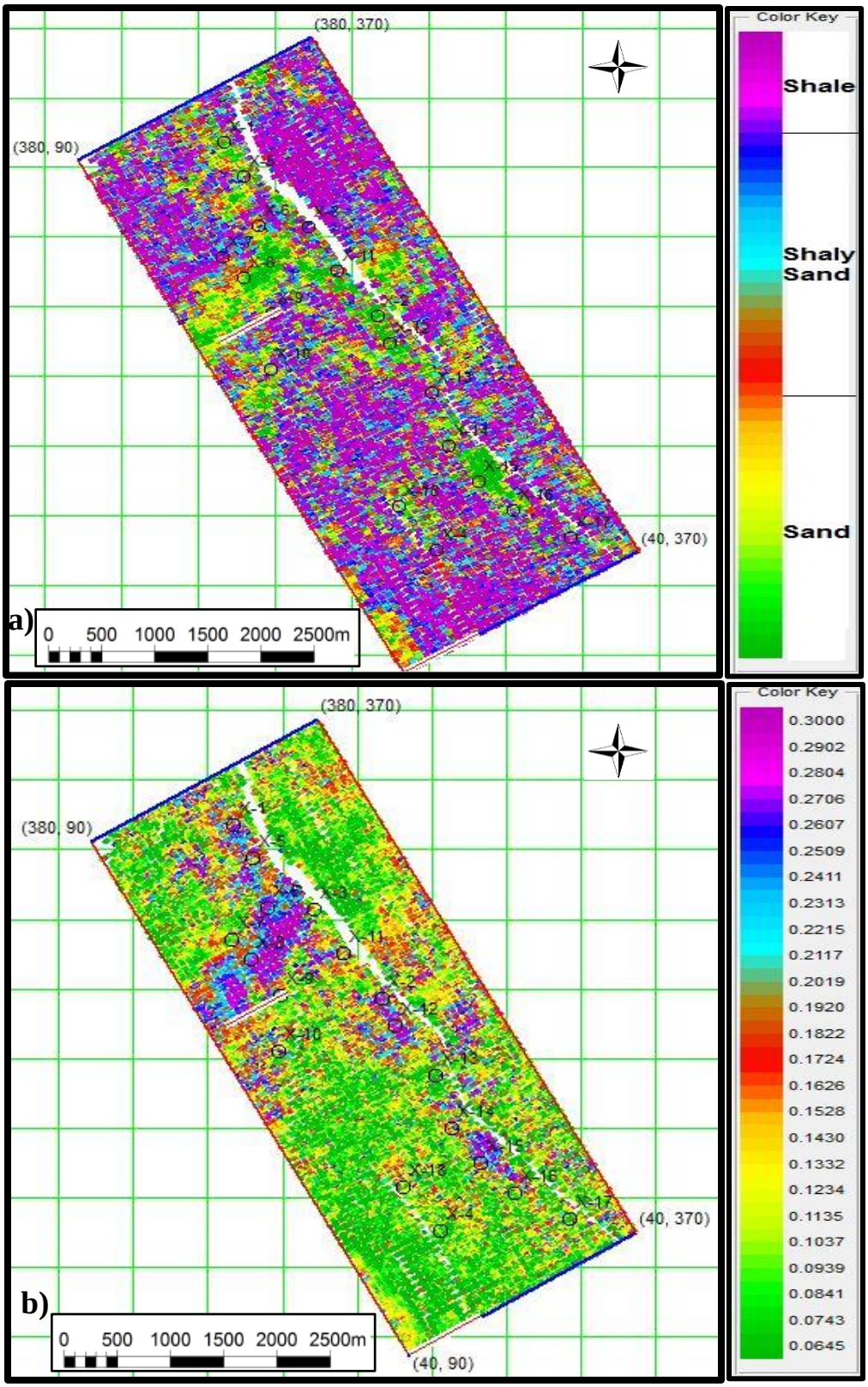

Figure 4.14 A time slice through the multivariate linear regression results at the Aradeiba-D top through a) Facies Model b) Porosity Model. The color scale is in the units of the target.

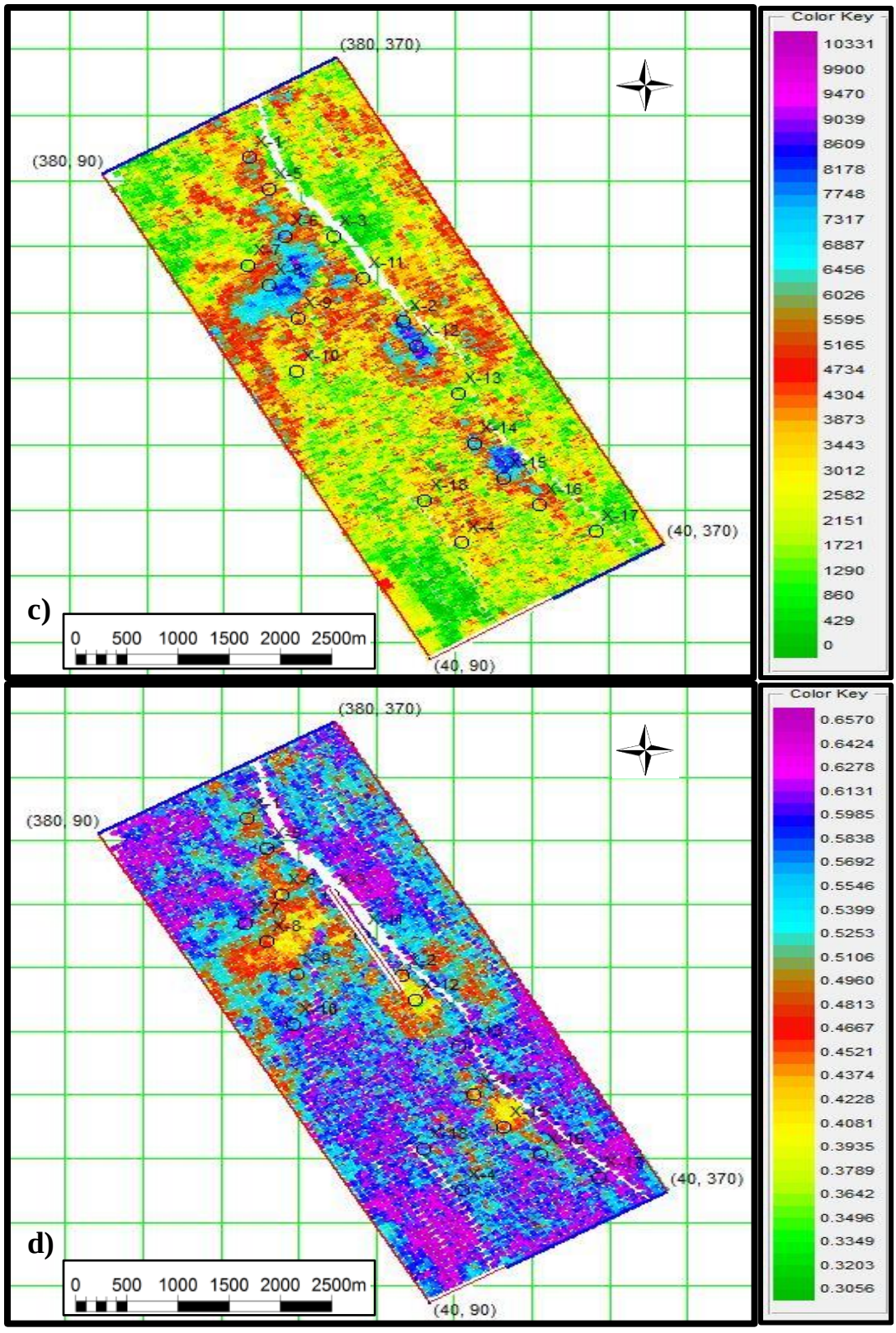

Figure 4.15 A time slice through the multivariate linear regression results at the Aradeiba-D top through c) Permeability Model d) Water Saturation Model. The color scale is in the units of the target.

CHAPTER 5

SUMMARY AND CONCLUSIONS

5.1 Summary

Based on the methods described in Chapter 3, I successfully estimated the petrophysical parameters (Shale Content (Vsh), porosity, Permeability, Fluid Saturation) for eighteen well logs (X-1 to X-18), which are located in the northeast part of Fula depression, Sudan. The analysis was carried out for the Aradeiba-D Member in the Upper Cretaceous sequence.

I did the petrophysical analysis using open-hole well-log data, namely resistivity logs (deep and shallow), porosity logs (density, neutron and sonic) and the gamma-ray log. I also made a qualitative interpretation (see Appendix) for the composite logs to get a preliminary idea about the lithology, porosity, permeability and water saturation of the Aradeiba-D unit.

According to the core analysis done by (CNPC, 2007), the main range of core porosity is 32% - 36% and the main range of core permeability is 100 – 5000mD, (Figure 5.1). Comparing the average interpretation results, (Table 5.1) with the core analysis results, (Figure 5.1), the computed shale volume, porosity, and water saturation values confirm the reliability of the integrated approach to evaluate shaly sand petrophysical parameters for this formation.

I constructed four distribution maps for the Aradeiba-D sand zone as shown in (Figure 5.2). The shale percentage map shows an increase of shale content along the eastern part and northwestern parts of the area which reaches its highest value of 44% at X-13 well in the central south east of the studied area while it decreases to 13% at X-18 well locality in the southwestern part.

Generally, the porosity distribution of the Aradeiba-D sand decreases gradually southeastern, northeastern, and northwestern-ward. The minimum porosity value (24%) is represented at the X-17 and X-11 wells in the southeast and northeast part, till it reaches its maximum value (38%) at X-5 well.

The permeability distribution of the Aradeiba-D sand follows the porosity trend. Its maximum value is 11Darcy at X-16 well and the minimum value 0.216 Darcy at X-7 well.

The water saturation map shows that the maximum value of water content is 51% at X-3 well and the minimum value of 5% is at the X-14 well.

Overall, it can be concluded from the petrophysical analysis that the reservoir quality increases in northwest-southeast direction. Also, the high porosity and permeability and low water saturation correspond to the sand facies while the opposite is true for shale.

I applied Artificial Neural Network trained on gamma ray (GR), sonic (DT), neutron porosity (NPHI), bulk density (RHOZ), and deep resistivity (RLA5) logs for facies classification. According to the lithological facies which were identified from well cuttings describtion, the neural network was used to classify the facies into three groups, shale, shaly sand, and sandstone. Comparing the results from the neural network with well cuttings, I found a very good correlation (see Appendix).

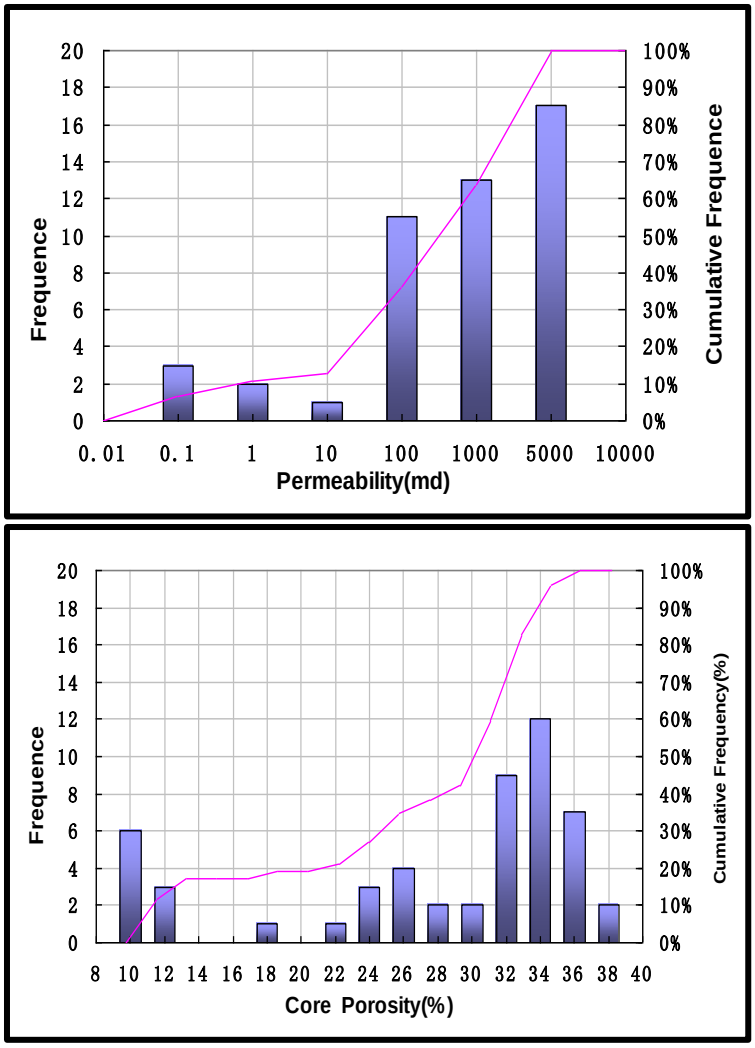

Figure 5.1 Core data analysis results for porosity and permeability from (CNPC, 2007)

Petrophysical Parameters	Average Range
Shale Volume (Vsh)	13% - 43 %
Porosity (Φ)	23% - 38 %
Permeability (K)	200 mD - 12000 mD
Water Saturation (Sw)	5% - 51 %

Table 5.1 Average Interpretation Results for the Aradeiba-D Sand zone.

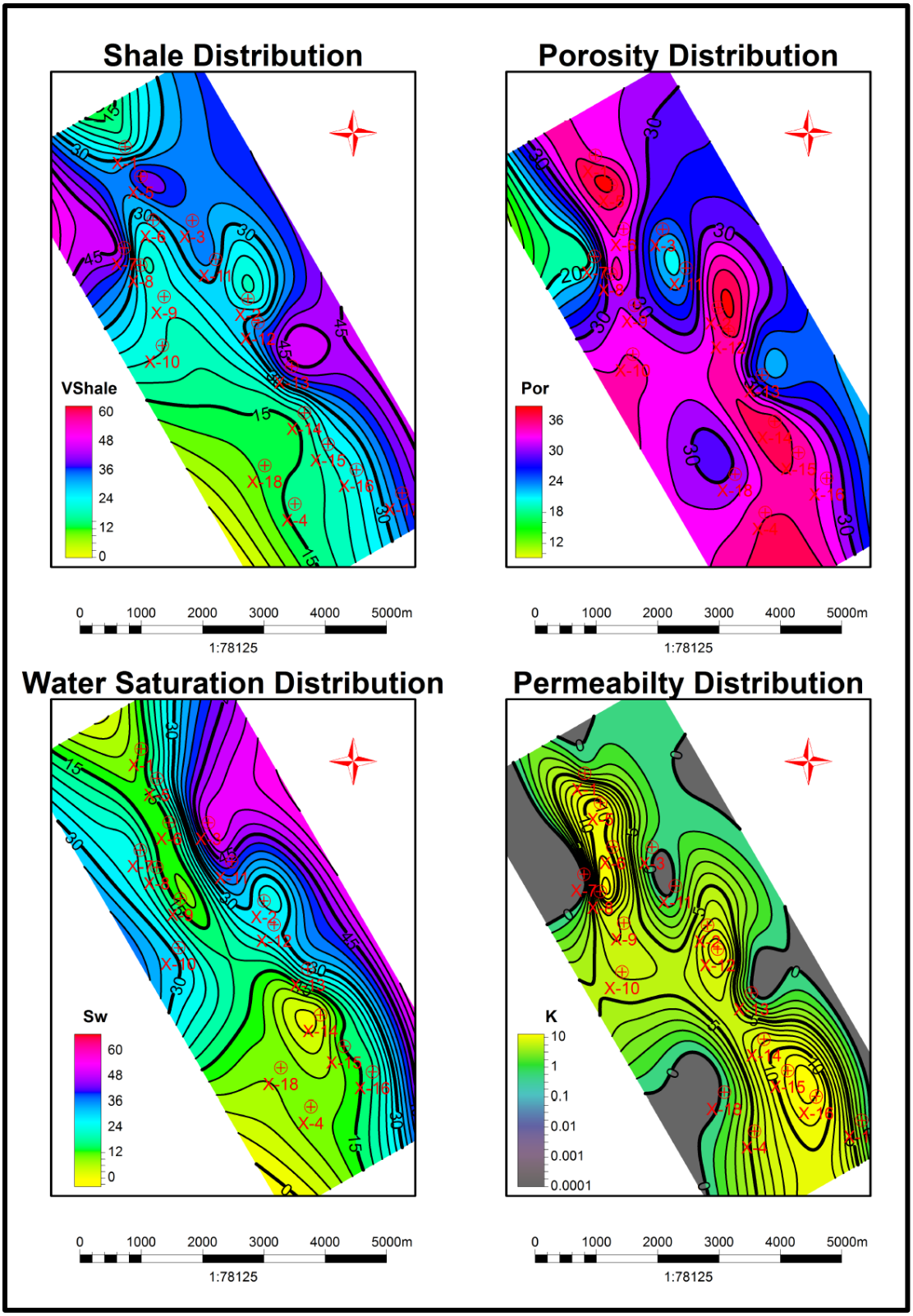

Figure 5.2 Average parameters (shale volume, porosity, permeability, and water saturation) distribution maps for the Aradeiba-D sand in the study area

In this study I have tried to predict lateral changes in reservoir properties (lithology, porosity, permeability, water saturation) within the Aradeiba-D Member. To do that, I first visually examined the seismic attributes to find the best candidates for the multivariate regression. Based on the stepwise linear regression and cross validation error analysis the optimal number of attributes and convolutional operator lengths were chosen. The entire process was applied to a targeted time window.

For any derived multi-attribute transform, the measure of performance has been cross-validation, which systematically removes wells from the analysis and measures the prediction error for these wells.

When I filtered the target logs (porosity, permeability, and water saturation) to match them with the seismic bandwidth, high-frequency and erratic values were removed and the results improved.

I calculated the correlation coefficient for training and validation results with an average error (the RMS difference between the target log values and the predicted values) for the four models. Table 5.2, summarizes the multi-attributes analysis parameters used and the final cross-correlation results.

Then I applied the derived transforms to the 3-D seismic volume. For each model from the four, I created two cross sections across the model corresponding to the in-line 253 and x-line 232 and intersecting the X-9 and X-1 wells. I found a good match between the facies and corresponding porosity, permeability, and water saturation. Thus the sand bodies are clearly identified laterally and vertically and differentiated from shales through their high porosities and permeabilities and low water saturations.

Finally, to display the aerial distribution of the sand bodies, I constructed a data slice through the computed facies, porosity, permeability, and water saturation as shown in (Figure 5.3), using a 10-ms window centered at the Aradeiba-D top in time domain. In this slice sand bodies' belts trending northwest–southeast and north-south can be recognized with the highest values of porosity and permeability and low water saturation, while they are randomly dispersed in the western and eastern regions.

The Model	No. of Attributes used	Operator Length	Training Correlation	Training Error	Validation Correlation	Validation Error
Facies	4	9	0.391	0.7458	0.291	0.7674
Porosity	4	9	0.762	0.0532	0.696	0.0585
Permeability	5	1	0.645	2280.78	0.582	2436.58
Water Saturation	2	1	0.452	0.1729	0.393	0.1788

Table 5.2 Multi-attribute analysis results summary

Facies Distribution **Porosity Distribution**

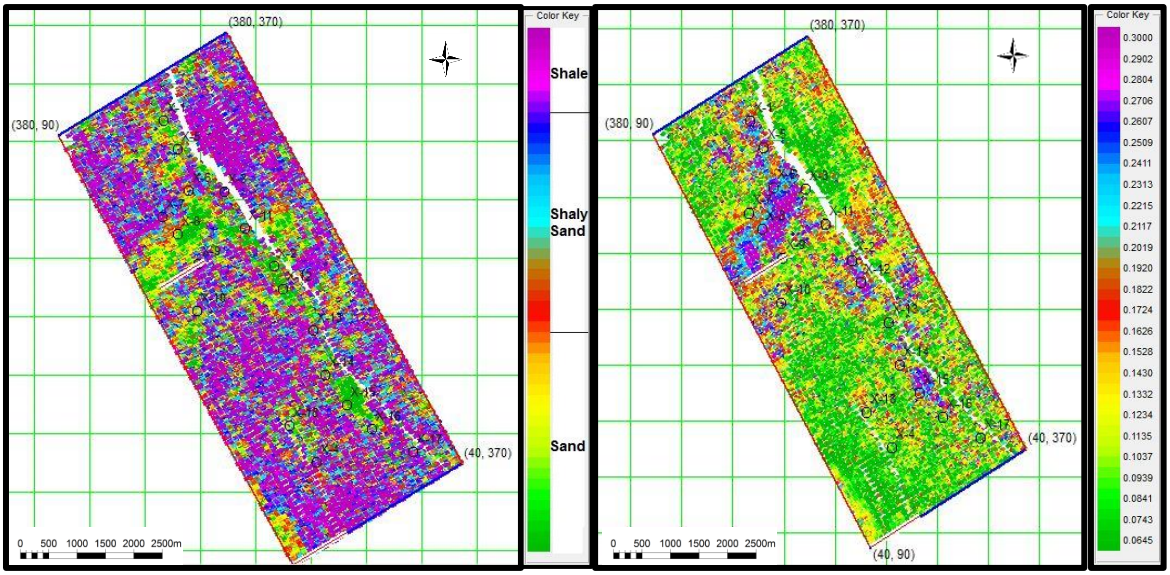

Permeability Distribution **Water Saturation Distribution**

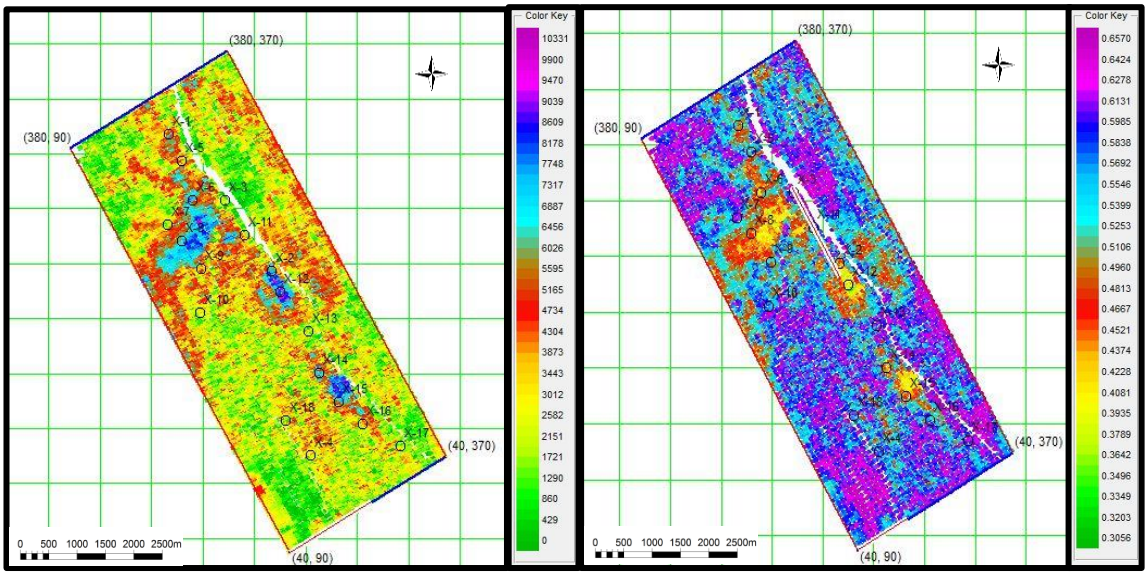

Figure 5.3 A time slice through the multivariate linear regression results at the Aradeiba-D top through Facies, Porosity, Permeability, and Water Saturation Models. The color scale is in the units of the target.

5.2 Conclusions

Shaly sands formation evaluation is a complex task. All logging responses and interpretation techniques are influenced by the shale. With this regard, shale volume is required for correcting the porosity as well as water saturation outcomes for that biased results associated with shale. It is considered as an indicator of reservoir quality, in which the lower shale content usually reveals a better reservoir. Thus, shale volume calculation is critical. Also, the integrated approach in petrophysical analysis can provide the most important and realistic petrophysical parameters such as shale volume, effective porosity, and water saturation.

Artificial neural networks are powerful tools for facies classification from the shale indicator logs (i.e. gamma ray, sonic, neutron porosity, bulk density, and deep resistivity logs). The ANN can be used as a quick solution for lithology prediction over a relatively large geographical area in basins with clastic sedimentation, if that the input data are of the adequate quality. Obtained lithology data can later be easily applied for further analyses, like in this case lithofacies mapping.

In order to get a better description of a reservoir, all available data such as geophysical, geological, and petrophysical data need to be integrated. Well log data has a very low spatial resolution and high vertical resolution, while seismic data has a high spatial resolution and low vertical resolution. Thus, combining these two types of information can lead to better understanding of the data and a more successful development of existing fields.

The difficulties in identifying and mapping sand and shale distribution in the Aradeiba-D Member in Muglad rift basin are related to two main factors: (1) very complex lateral and vertical sand distribution owing to the nature of the lacustrine and fluvio-deltaic depositional environment, and (2) complex tectonic structures. The multi-seismic attributes driven reservoir properties method proved to be useful in integrating seismic data and well information to predict reservoir properties. Well logs integration is a critical and essential part of the standard 3D seismic interpretation workflow. It contributes greatly in calibration, understanding/validation of seismic responses, and generating volumes of lithological/reservoir properties from seismic attributes.

This research implies that a multi-attribute seismic evaluation could be efficient in predicting sand as well as shale distributions when it is difficult to do so using standard usually means. The reason is being that the methodology creates statistical correlations to identify the seismic attributes necessary to determine pseudo logs which can differentiate sands from shales.

According to my analysis, the sand bodies of Aradeiba-D reservoir are of small size. The relation between sand bodies and delineation of their boundaries can be based on the result of (a very carefully carried out) multi-attribute analysis. The reservoir in this formation is mainly composite of single sand bodies, the total thickness is small, the thickest part achieves nearly 20 meters, average thickness is about 7 meters, it is distributed as belts from Northwest to Southeast.

The maps of predicted lithology and petrophysical parameters generated show good correlation with that observed in all wells in the study area, which may provide a confidence to drill in further locations.

5.3 Recommendations

This study can be extended using multi-attributes neural networks to increase the correlation match. The fluvio-deltaic depositional environment has thinly bedded sands and shales, so they do not usually respond to seismic analysis because the too thin beds are resolved by the seismic data and the acoustic properties of the sands and shales are very similar. Thus, multi-attribute neural network approach provides a possible means of lithology identification under these conditions.

One of the most controversial problems in formation evaluation is the shale effect in reservoir rocks. Thus, I recommend a thorough study to the clay minerals affect the reservoir quality which can be identified from cores or logs which will enhance the petrophysical parameters calculation.

References

[1] Abdullatif, O. M. (1999). The evolution of the Muglad rift basin of interior Sudan as revealed from sedimentological, mineralogical and chemical data. *Journal of African Earth Sciences, 28*(4), 2.

[2] Abdullatif O. M., (2002). Burial Diagenesis and Thermal Maturity Evaluation of The North West Muglad Rift Basin, Sudan, *AAPG conference*, Cairo 2002: Ancient Oil-New Energy.

[3] Ahmed, A., Hassan, M., Trivedi, K. B., & Elamahi, R. (2006, November). Application of Sequence Stratigraphy in Reservoir Characterization of a Fluvio-deltaic Succession: Aradeiba Formation, Muglad Basin, Sudan. *AAPG International Conference and Exhibition*, Perth, West Australia.

[4] Ayad M. I., and Abdullatif O. M., (2002). Depositional Environment and Reservoir Heterogeneity of Bentiu Formation (Albian-Cenomanian), Muglad Rift Basin. *AAPG conference Cairo*, 2002: Ancient Oil-New Energy.

[5] Browne, S.E. and Fairhead, J.D. (1983). Gravity Study of the Central African Rift System: a Model of Continental Disruption. 1. The Ngaoundere and Abu Gabra rifts. In: P. Morgan (Editor), Processes of Continental Rifting. *Tectonophysics, 94*: 187-203.

[6] Browne, S.E., Fairhead, J.D. and Mohamed, I.I., (1985). Gravity Study of the White Nile Rift, Sudan, and its Regional Tectonic Setting. *Tectonophysics, 113*: 123-137.

[7] Brown, A. R. (1996). Seismic attributes and their classification. *The leading edge, 15*(10), 1090-1090.

[8] Brown, A. R. (2001). Understanding seismic attributes. *Geophysics, 66*(1), 47-48.

[9] Chen, Q., & Sidney, S. (1997). Seismic attribute technology for reservoir forecasting and monitoring. *The Leading Edge, 16*(5), 445-448.

[10] Chopra, S., & Michelena, R. J. (2011). Introduction to this special section: Reservoir characterization. *The Leading Edge, 30*(1), 35-37.

[11] CNPC, (2007). G & G Milestone of FNE FDP Study, *Unpublished Report*.

[12] Doyen, P. M. (1988). Porosity from seismic data: A geostatistical approach. *Geophysics, 53*(10), 1263-1275.

[13] Draper, N. R., Smith, H., & Pownell, E. (1966). *Applied regression analysis* (Vol. 3). New York: Wiley.

[14] Dresser Atlas (1979): "Log Interpretation Charts": Houston, Dresser Industries, Inc.

[15] Eftekharifar, M., & Han, D. H. (2011, September). 3D Petrophysical modeling using complex seismic attributes and limited well log data. In *2011 SEG Annual Meeting*.

[16] Eltom, H. A. (2007). Sedimentology and Sequence Stratigraphy of fluvial-lacustrine, Mesozoic, Abu Gabra and Bentiu formations, Muglad rift basin, Sudan. M.Sc.Thesis, *King Fahd University of Petroleum and Minerals* (Saudi Arabia).

[17] Fairhead, J. D. (1988). Mesozoic Plate Tectonic Reconstructions of the Central South Atlantic Ocean: The Role of the West and Central African Rift System. *Tectonophysics, 155*(1), 181-191.

[18] Gastaldi, C., Biguenet, J., and de Pazzis, L. (1997). "Reservoir Characterization from Seismic Attributes: An example from the Peciko Field (Indonesia)." *The Leading Edge, 16*(3), 263–266.

[19] Gibbs, A. D. (1990). Linked fault families in basin formation. *Journal of Structural Geology, 12*(5), 795-803.

[20] Genik, G. J. (1993). Petroleum Geology of Cretaceous-Tertiary Rift Basins in Niger, Chad, and Central African Republic. *AAPG Bulletin, 77*(8), 1405-1434.

[21] Giedt, N. R., (1990). Unity Field, Muglad Rift Basin, Upper Nile Province. In: Beaumont, E.A., Foster, N.H. (ed), Structural Traps; III, Tectonic Fold and Fault Traps, American Association of Petroleum Geologists Treatise of Petroleum Geology, Atlas of Oil and Gas Fields, A-019, 177-197.

[22] GRAS (Geological Research Authority of the Sudan), (1981). Geological Map of the Sudan. *Unpublished*.

[23] Hampson, D. P., Schuelke, J. S., & Quirein, J. A. (2001). Use of multiattribute transforms to predict log properties from seismic data. *Geophysics, 66*(1), 220-236.

[24] Hilchie, D.W. (1978). “Applied Open Hole Interpretation”; Golden Colorado, D.W. Hilchie, Inc.

[25] Hwang, R. J., Ahmed, A. S., & Moldowan, J. M. (1994). Oil Composition Variation and Reservoir Continuity: Unity Field, Sudan. *Org. Geochem., 21*(2), 171-188.

[26] Ibrahim, A. S. M. (2003). Sedimentology and Reservoir Geology of the Middle-Upper Cretaceous Strata in Unity and Heglig Fields in SE Muglad Rift Basin, Sudan. *Unpublished Doctoral Dissertation*.

[27] Idris K. (2002). Lateral Seal- a Major Exploration Risk in the Faulted Traps of the Cretaceous Petroleum System - Central Muglad Basin, Sudan 2004. *AAPG International Conference and Exhibition.*

[28] Idris K. (2005). An Integrated Petroleum System Study for the Aradeiba and Bentiu Plays, Block 4 Central Muglad Basin, Sudan 2005. *AAPG International Conference and Exhibition.*

[29] Kalkomey, C. T. (1997). Potential risks when using seismic attributes as predictors of reservoir properties. *The Leading Edge, 16*(3), 247-251.

[30] Kaska, H. V. (1989). A spore and pollen zonation of Early Cretaceous to Tertiary non-marine sediments of central Sudan. *Palynology, 13*(1), 79-90.

[31] Kurniawan, F. (2005). Shaly Sand Interpretation Using CEC-Dependent Petrophysical Parameters (*Doctoral dissertation*).

[32] Mann, D. C. (1989). Thick-skin and thin-skin detachment faults in continental Sudanese rift basins. *Journal of African Earth Sciences (and the Middle East), 8*(2), 307-322.

[33] Mc Hargue T. R., Heidrick J. L., Livingstone J. E. (1993). Tectonostratigraphic development of the interior Sudan rifts, Central Africa. *Tectonophysics 213*, 187–202.

[34] Mohamed, A. Y., Ashcroft, W. A., & Whiteman, A. J. (2001). Structural development and crustal stretching in the Muglad Basin, southern Sudan. *Journal of African Earth Sciences, 32*(2), 179-191.

[35] Mohamed, A. Y., Pearson, M. J., Ashcroft, W. A., & Whiteman, A. J. (2002). Petroleum maturation modelling, Abu Gabra–Sharaf area, Muglad Basin, Sudan. *Journal of African Earth Sciences, 35*(2), 331-344.

[36] Mustafa, A. A., & Tyson, R. V. (2002). Organic Facies of Early Cretaceous Synrift Lacustrine Source Rocks from the Muglad Basin, Sudan. *Journal of Petroleum Geology, 25*(3), 351-366.

[37] Mohamed, A. Y., Pearson, M. J., Ashcroft, W. A., Iliffe, J. E., & Whiteman, A. J. (1999). Modeling Petroleum Generation in the Southern Muglad Rift Basin, Sudan. *AAPG Bulletin, 83*(12), 1943–1964.

[38] Mohamed, A. A., Iliffe, J. E., Ashcroft, W. A., & Whiteman, A. J. (2000). Burial and Maturation History of the Heglig area, Muglad Basin, Sudan. *Journal of Petroleum Geology, 23*(1), 107-128.

[39] Mohamed, O. I., & Mohamed, A. M. (2004, October). Biomarker Indications as Evidence for Organo-facies Variations within the Abu Gabra Source Rock of the Muglad Basin, Sudan. *6th AAPG International Conference*, Beijing.

[40] Mohammed, A. A. (2006, January). Enhancement of OIP through Reservoir Modeling of a Multilayered Siliciclastic Reservoir: A Case Study from Muglad Basin, Sudan. *Geo 2006 Conference*, Manama, Bahrain.

[41] Mohammed, A. A. (2008, October). The Reliability of 3D Geological Modeling in the Original Oil in Place (OOIP) Estimation: a Case Study from Muglad Basin, Sudan. *SIS Global Forum 2008*, Paris, France.

[42] Pavanel, E., Fervari, M., Corrao, A., Gallagher, M., & Ciurlo, B. (2009). Pay Sand Mapping using Seismic multi-attribute calibration proved to be effective from development to near field exploration stages: A case study from De Soto Canyon, Gulf Of Mexico. In *SEG Technical Program Expanded Abstracts 2009* (pp. 567-571). Society of Exploration Geophysicists.

[43] Poupon, A., Clavier, C., Dumanoir, J., Gaymard, R., & Misk, A. (1970). Log Analysis of Sand-Shale Sequences-A Systematic Approach. *Journal of Petroleum Technology, 22*(7), 867-881.

[44] Poupon, A., and Gaymard, R. (1970). The evaluation of clay content from logs. Trans., *SPWLA 11th Annu. Logging Symp*., Pap. G..

[45] Poupon, A., & Leveaux, J. (1971). Evaluation of water saturation in shaly formations. *The Log Analyst, 11*, 3-8.

[46] RRI (Robertson Research International PLC) (1991). Appraisal of the hydrocarbon bearing reservoirs. Unity Area, 1, Sudan. *Unpublished*.

[47] Saida O. Mohammed and Abdullatif O. M. (2002). Facies and Reservoir Quality of Zarqa Formation (Turonian-Late Senonian) in Heglig and Unity Fields, Muglad Rift Basin. *AAPG conference Cairo 2002*: Ancient Oil-New Energy.

[48] Sattar, N., Khan, F., Farid, A., Khan, A., Hasnain, K., and Shabih, M. (2010). ”Presenting Seismic Stratigraphy and Attribute Analysis as Pioneer Techniques for Delineation of Reservoir Quality Sand Bodies in the Indus Offshore Basin, Southwest Pakistan.” *The Leading Edge, 29*(5), 524–529.

[49] Schandelmeier, H., & Pudlo, D. (1990). The Central African Fault Zone (CAFZ) in Sudan—a possible continental transform fault. *Berl Geowiss Abh A, 120*(1), 31-44.

[50] Schandelmeier, H., Reynolds, P. O., & Küster, D. (1993). Spatial and temporal relationship between alkaline magmatism and early rifting in north/central Sudan. *Geoscientific Research in Northeast Africa*, 221-225.

[51] Schull, T. J. (1988). Rift basins of interior Sudan: Petroleum exploration and discovery. *AAPG Bulletin, 72*(10), 1128-1142.

[52] Schlumberger (1987). Log Interpretation Principle/ Application, New York.

[53] Schultz, P.S., Ronen, S., Hattori, M., and Corbett, C. (1994). Seismic Guided Estimation of Log Properties, parts 1, 2, and 3: *The Leading Edge, 13*(5), 305-310, 674-678, and 770-776.

[54] Sheriff, R. E. (1992). *Reservoir geophysics* (No. 7). Soc of Exploration Geophysicists.

[55] Sukmono, S. (2007). ”Application of Multi-attribute Analysis in Mapping Lithology and Porosity in the Pematang-Sihapas groups of Central Sumatra Basin, Indonesia.” *The Leading Edge, 26(*2), 126–131.

[56] Taner, M. T., Koehler, F., & Sheriff, R. E. (1979). Complex seismic trace analysis. *Geophysics, 44*(6), 1041-1063.

[57] Taner, M. T.; Schuelke, J. S.; O'Doherty, R.; Baysal, E. (1994). Seismic Attributes Revisited: *64th Annual Internat. Mtg*., Soc. Expl. Geophys., Expanded Abstracts, 1104-1106.

[58] Trappe, H., & Hellmich, C. (1998). Seismic characterization of Rotliegend reservoirs: from bright spots to stochastic simulation. *First break, 16*(3), 79-87.

[59] Vail, J. R. (1978). Outline of the Geology and Mineral Deposits of the Democratic Republic of the Sudan and Adjacent areas. Overseas Geol. Miner. Resour., IGS, London, v. 49, p. 68

[60] Vail, J. R. (1985). Alkaline ring complexes in Sudan. *Journal of African Earth Science, 3*(1-2), pp. 51-59.

[61] Walker, R., Wong, C., Malcotti, H., Pèrez, E., and Sierra, J. (2005). ”Seismic Multi-attribute Analysis for Lithology Discrimination in Ganso Field, Oficina Formation, Venezuela.” *The Leading Edge, 24*(11), 1160–1166.

[62] Wyllie, M.R.J. (1963). “The Fundamentals of Well Log Interpretation”; New York Academic Press.

[63] Yamin, Z., & Qin, G. (2011). Petroleum System of the Fula Depression at the Muglad Basin in the Central African Fault Zone. *Journal of Earth Science, 22*(3), 363–370.

[64] Zhang, Y. M. (2007). Structural Geometry of Muglad Basin, Central Africa. *Petroleum Exploration and Development, 34*(4): 502–507

Appendix

Well logs interpretation

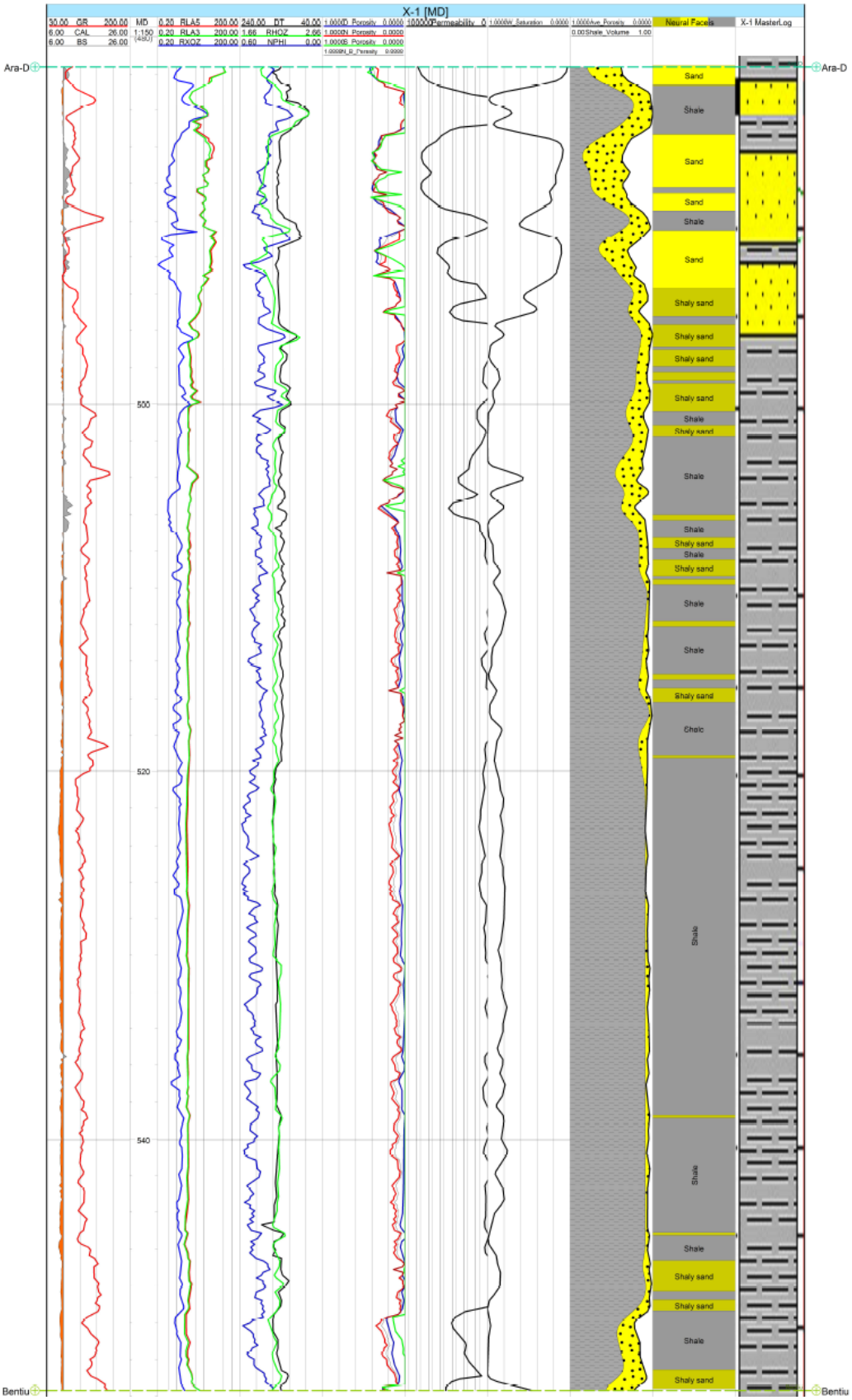
X-1 [MD]
Neural Facels
X-1 MasterLog
Ara-D
Bentiu
500
520
540
Sand
Shale
Shaly sand
Chalc

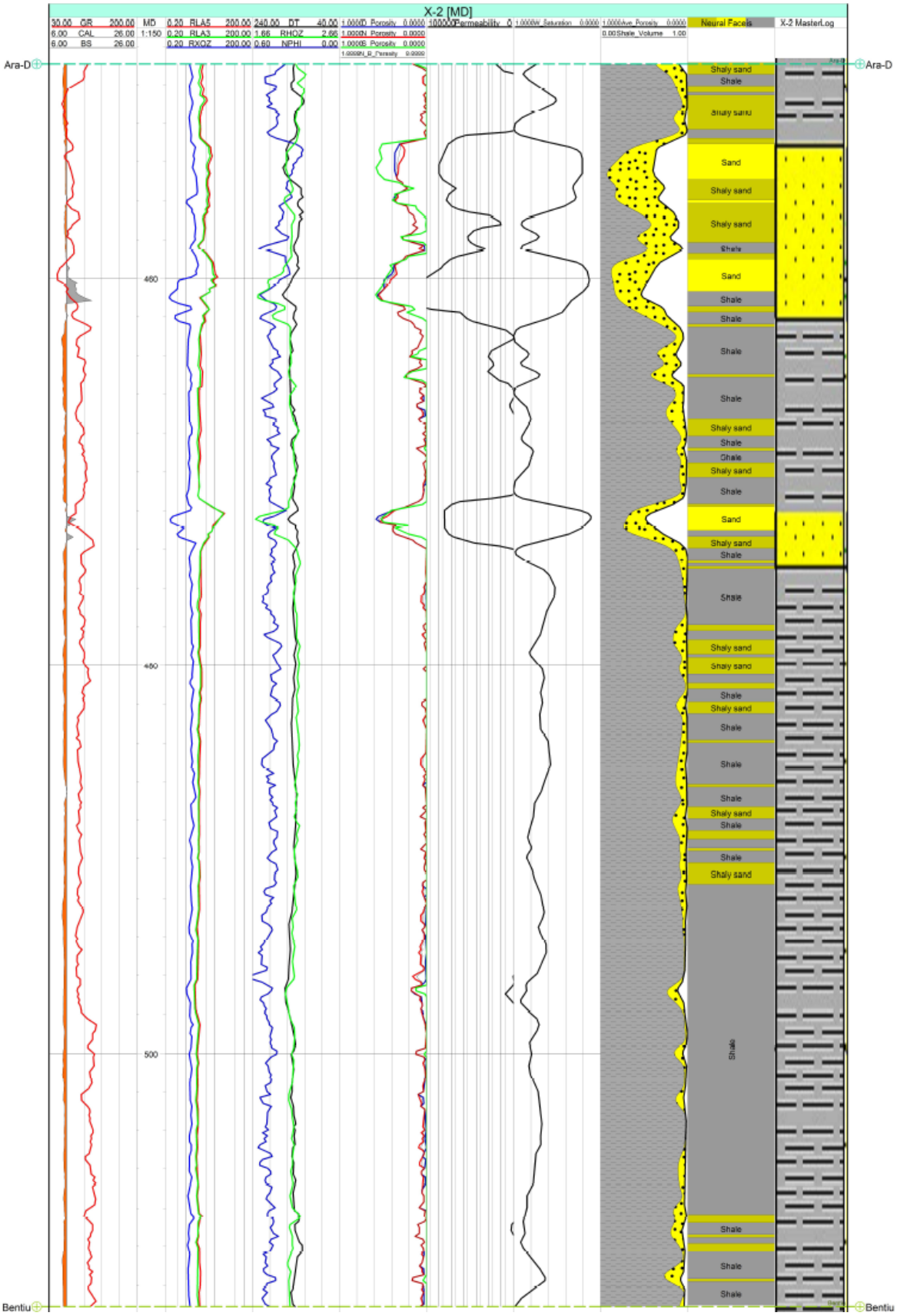
X-2 [MD]
Neural Facies
X-2 MasterLog
Ara-D
Ara-D
Bentiu
Bentiu
460
480
500
Shaly sand
Shale
Sand

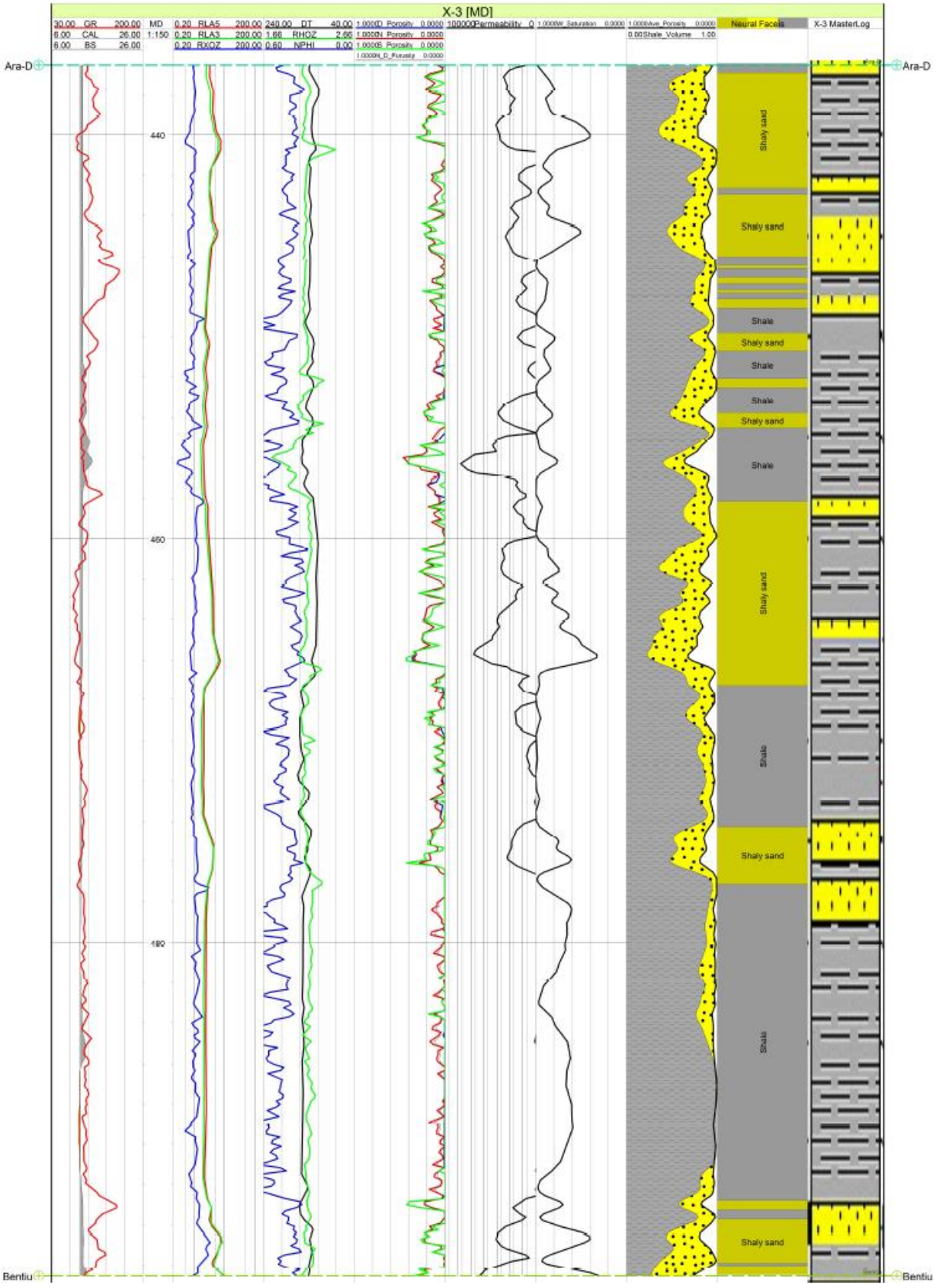
X-3 [MD]
30.00 GR 200.00
6.00 CAL 26.00
6.00 BS 26.00
MD
1:150
0.20 RLA5 200.00
0.20 RLA3 200.00
0.20 RXOZ 200.00
240.00 DT 40.00
1.66 RHOZ 2.66
0.60 NPHI 0.00
Permeability
Neural Facies
X-3 MasterLog
Ara-D
Ara-D
440
460
480
Shaly sand
Shaly sand
Shale
Shaly sand
Shale
Shale
Shaly sand
Shale
Shaly sand
Shale
Shaly sand
Bentiu
Bentiu

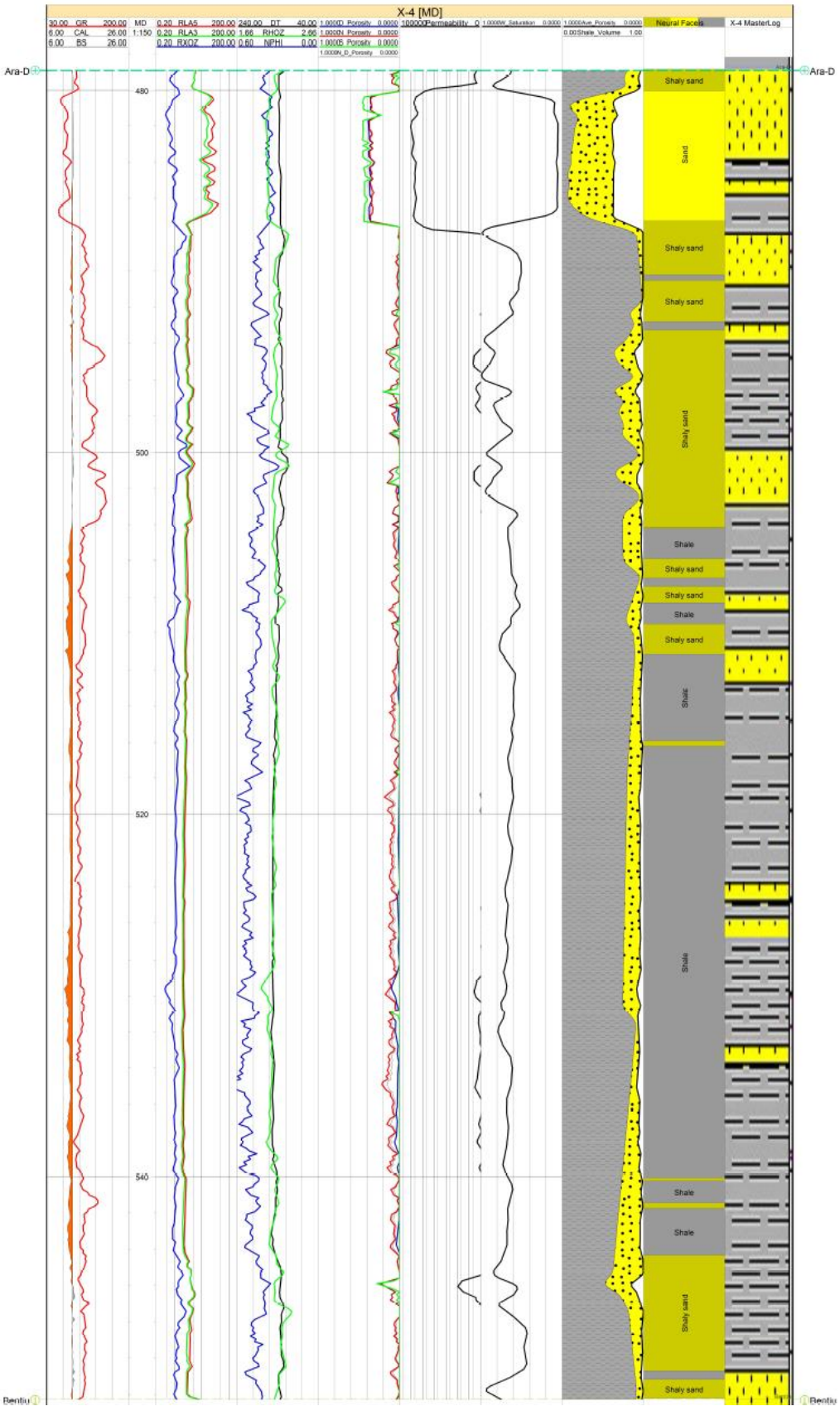
X-4 [MD]
Neural Facies
X-4 MasterLog
Ara-D
Ara-D
480
500
520
540
Shaly sand
Sand
Shaly sand
Shaly sand
Shaly sand
Shale
Shaly sand
Shaly sand
Shale
Shaly sand
Shale
Shale
Shale
Shale
Shaly sand
Shaly sand
Bentiu
Bentiu

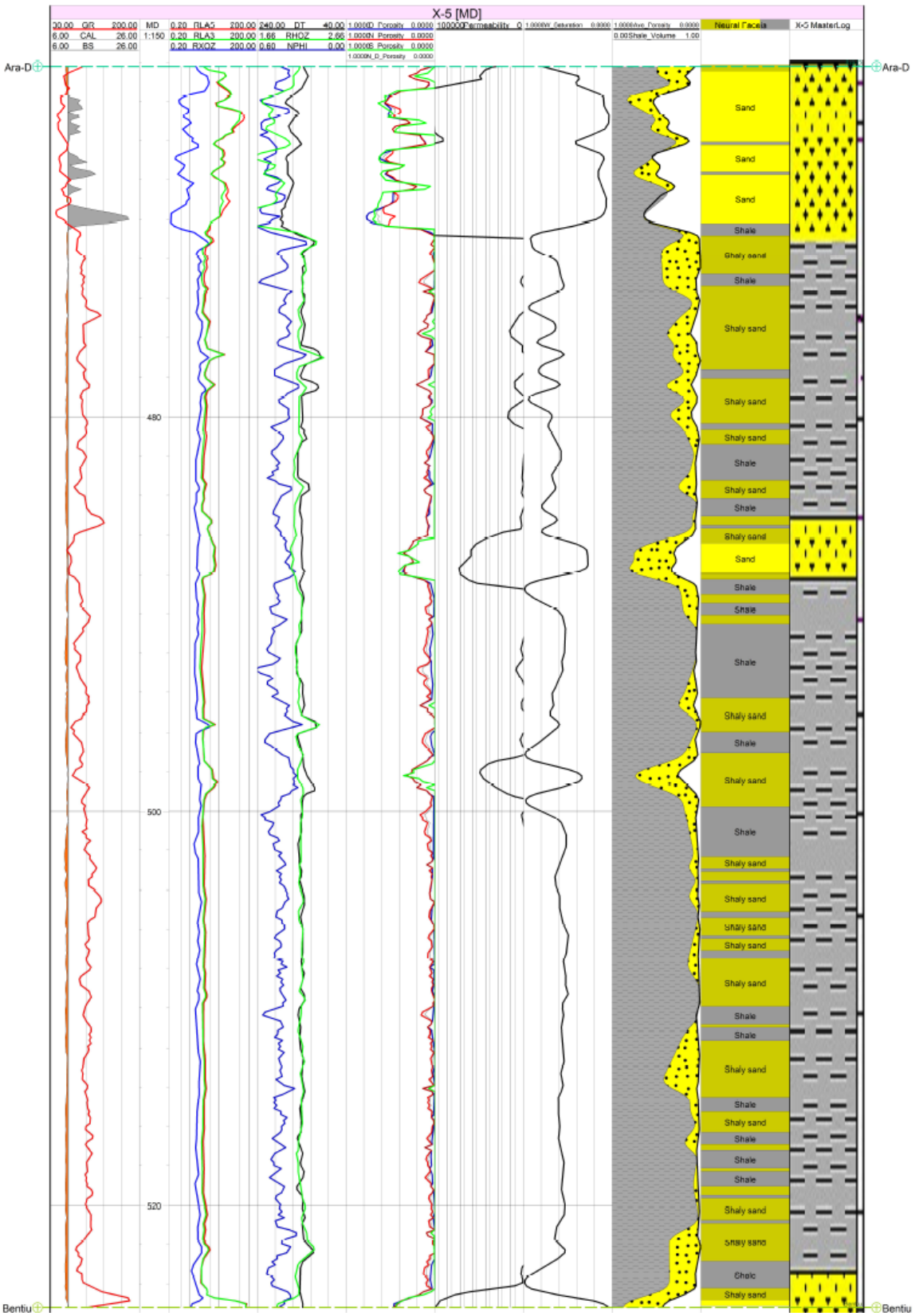
X-5 [MD]
30.00 GR 200.00
6.00 CAL 26.00
6.00 BS 26.00
MD
1:150
0.20 RLA3 200.00
0.20 RLA3 200.00
0.20 RXOZ 200.00
240.00 DT 40.00
1.66 RHOZ 2.66
0.60 NPHI 0.00
Neural Facies
X-5 MasterLog
Ara-D
Ara-D
480
500
520
Sand
Shaly sand
Shale
Chalc
Bentiu
Bentiu

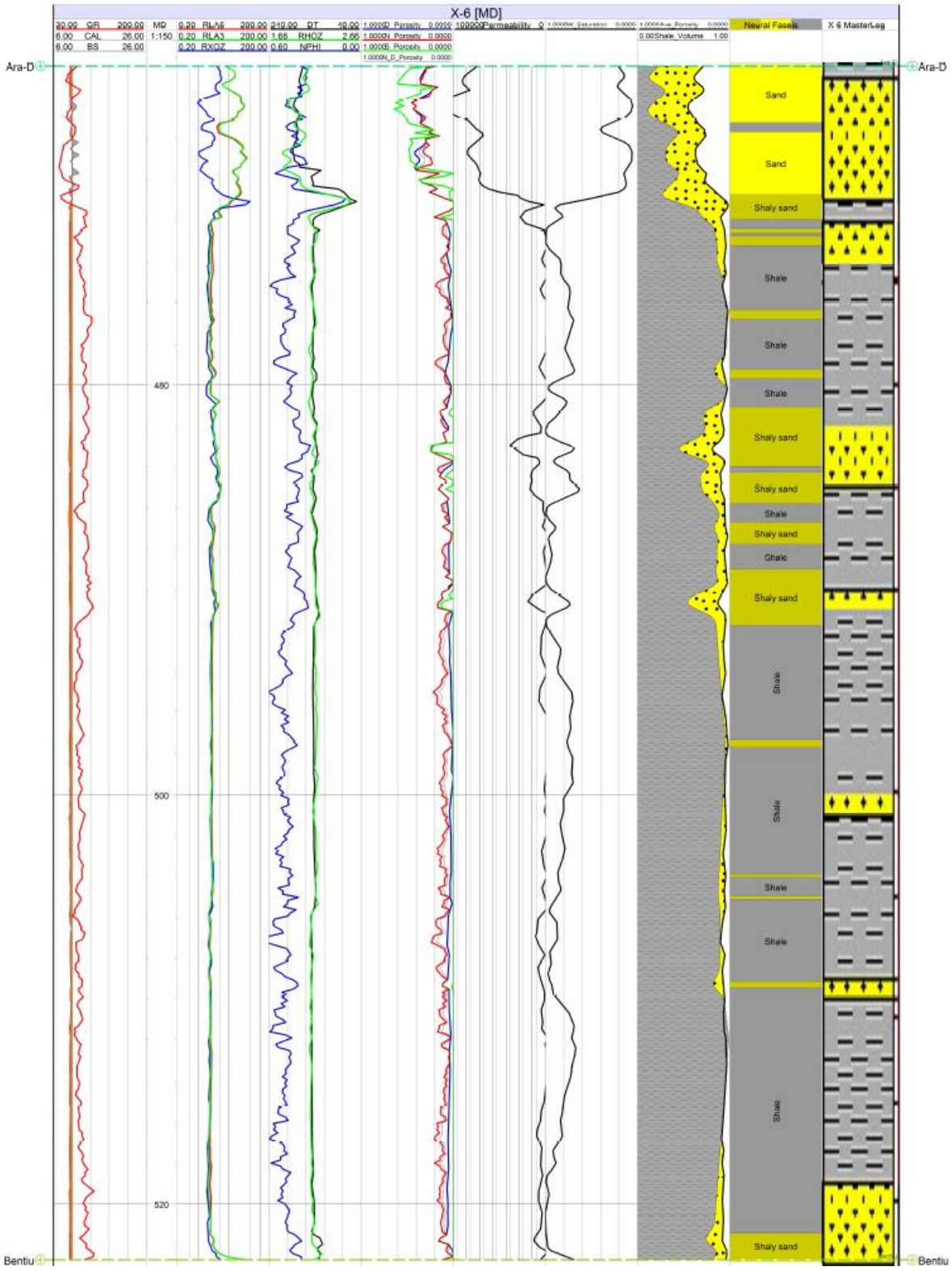
X-6 [MD]
GR 200.00
CAL 26.00
BS 26.00
MD
1:150
RLA5 200.00
RLA3 200.00
RXOZ 200.00
RT 10.00
RHOZ 2.65
NPHI 0.00
Permeability
Shale_Volume
Neural Facies
X 6 MasterLog
Ara-D
Bentiu
480
500
520
Sand
Sand
Shaly sand
Shale
Shale
Shale
Shaly sand
Shaly sand
Shale
Shaly sand
Shale
Shaly sand
Shale
Shale
Shale
Shaly sand

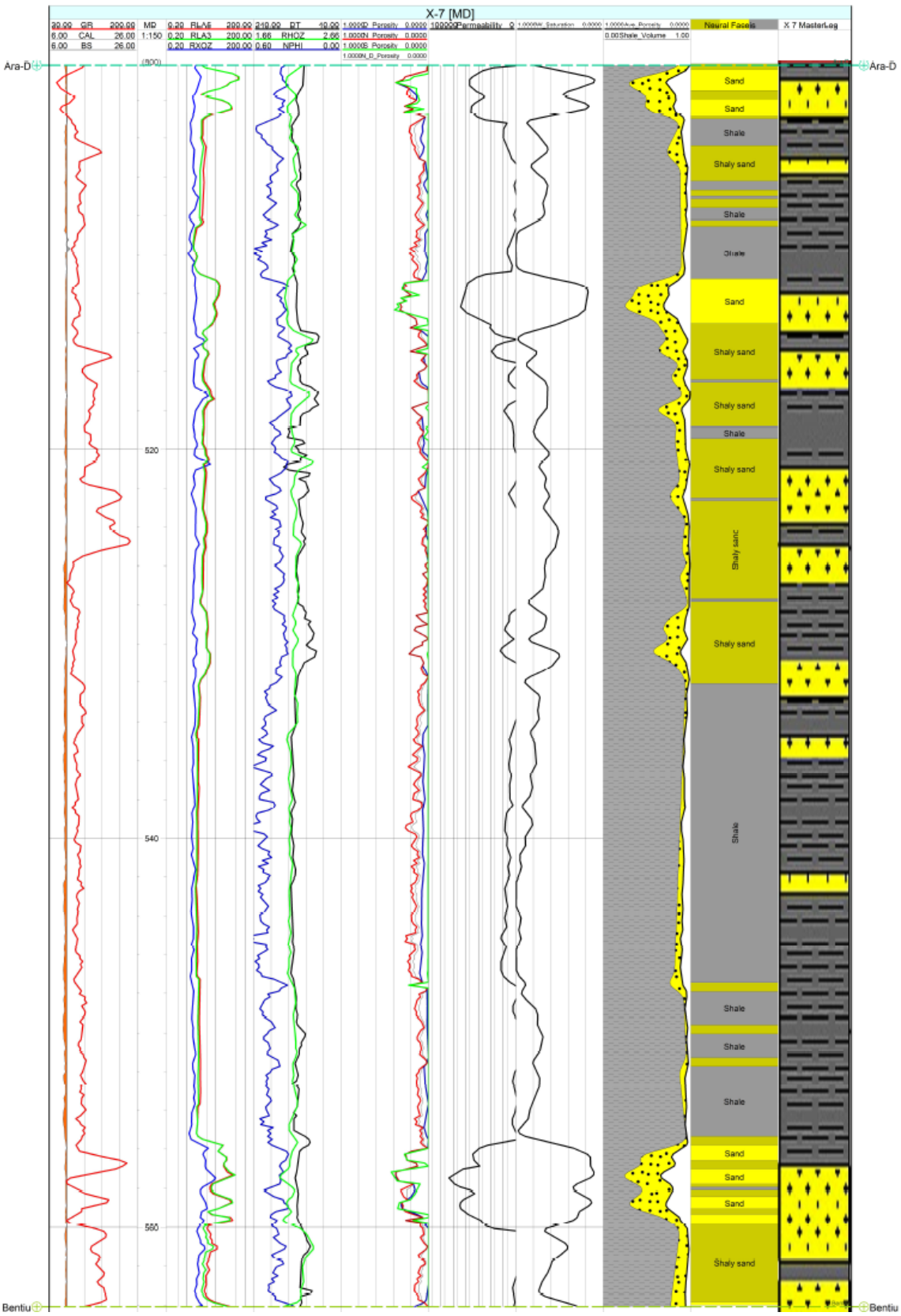
X-7 [MD]
Ara-D
Bentiu
Neural Facies
X 7 MasterLog
Sand
Shale
Shaly sand
Shaly sanc
520
540
550

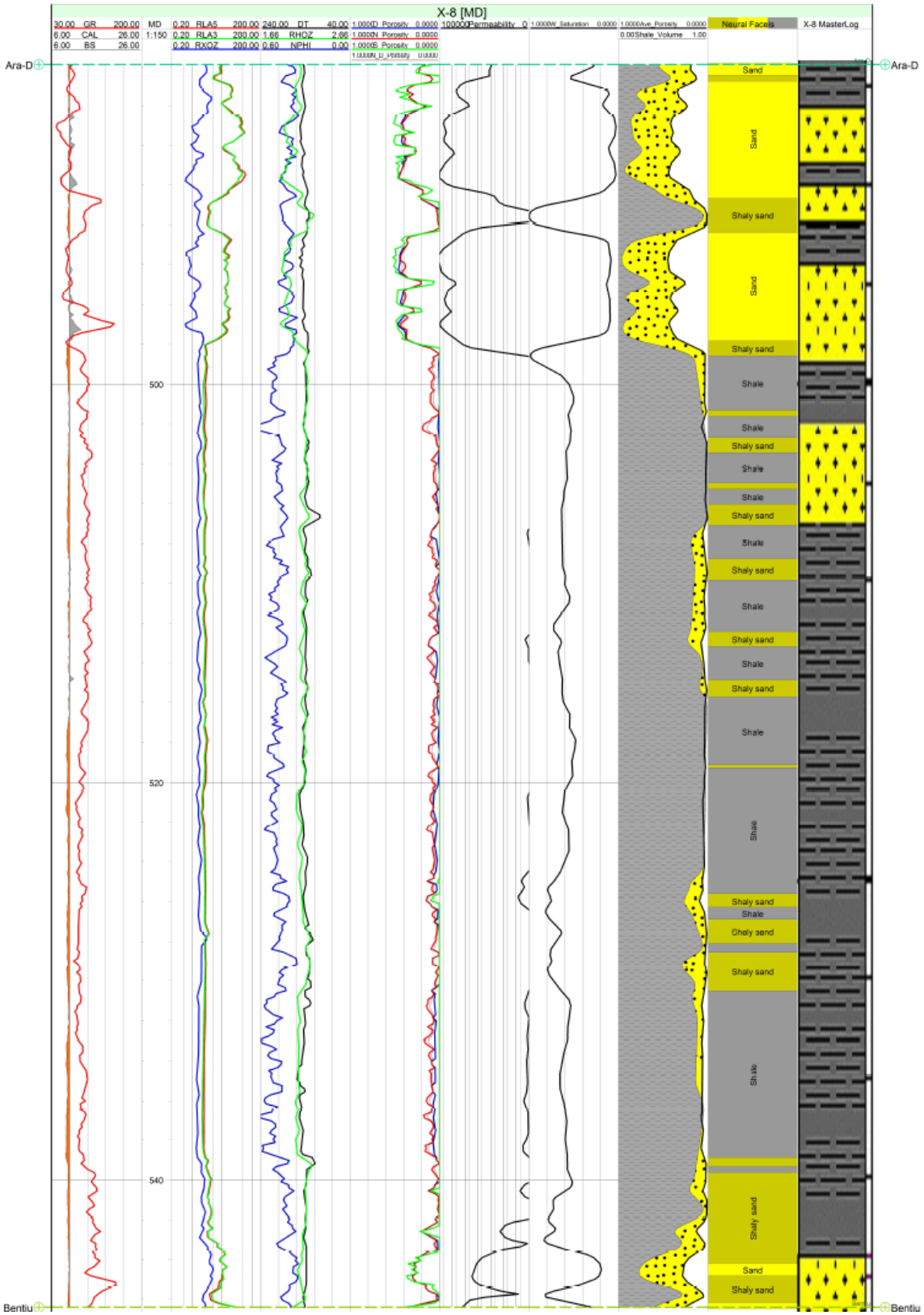
X-8 [MD]
30.00 GR 200.00
6.00 CAL 26.00
6.00 BS 26.00
MD
1:150
0.20 RLA5 200.00
0.20 RLA3 200.00
0.20 RXOZ 200.00
240.00 DT 40.00
1.66 RHOZ 2.66
0.60 NPHI 0.00
1.0000D_Porosity 0.0000
1.0000N_Porosity 0.0000
1.0000S_Porosity 0.0000
100000Permeability 0
1.0000W_Saturation 0.0000
1.0000Ave_Porosity 0.0000
0.00Shale_Volume 1.00
Neural Facies
X-8 MasterLog
Ara-D
Bentiu
500
520
540
Sand
Shaly sand
Shale
Ghaly sand

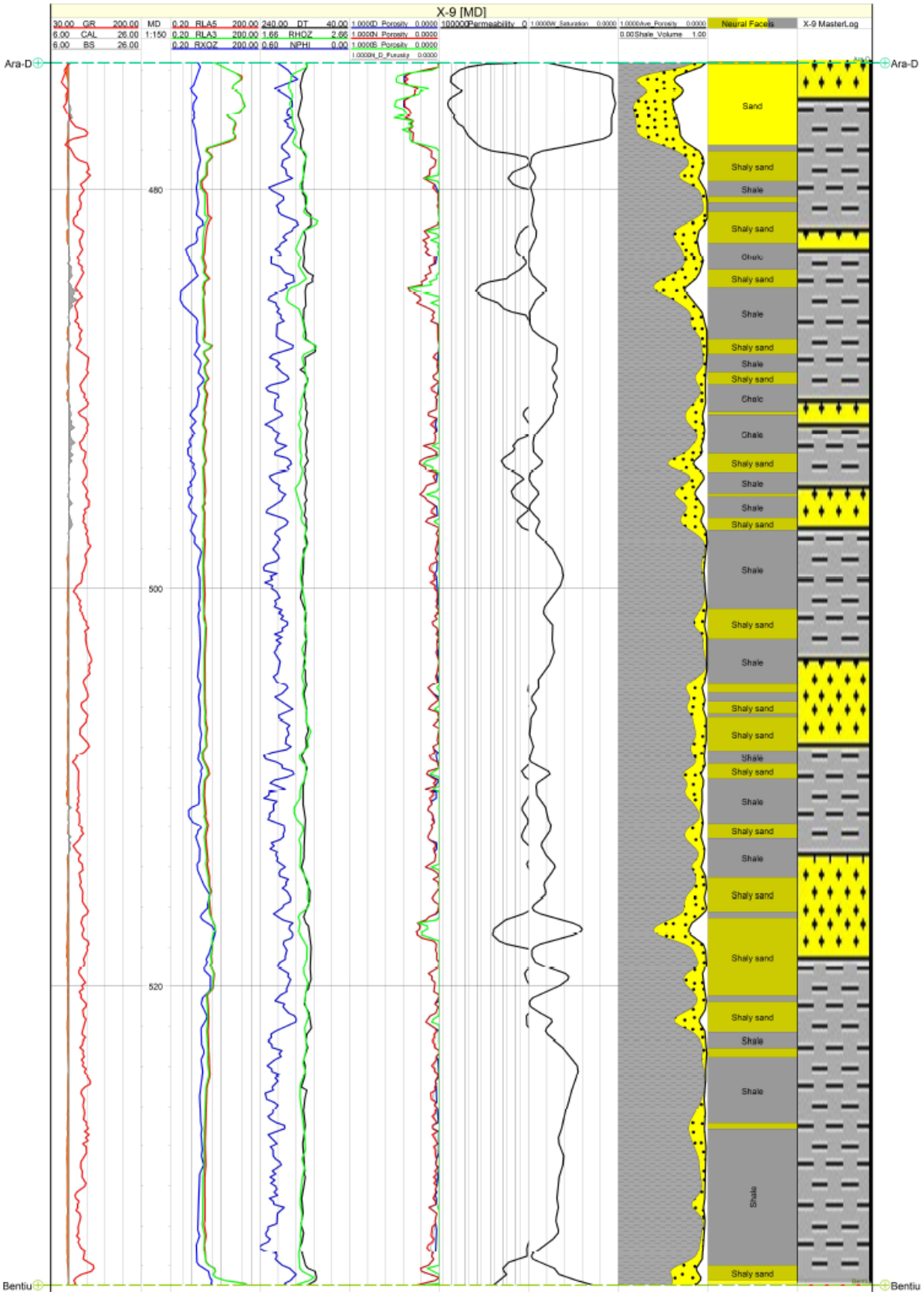
X-9 [MD]
30.00 GR 200.00
6.00 CAL 26.00
6.00 BS 26.00
MD
1:150
0.20 RLA5 200.00
0.20 RLA3 200.00
0.20 RXOZ 200.00
240.00 DT 40.00
1.66 RHOZ 2.66
0.60 NPHI 0.00
Neural Facies
X-9 MasterLog
Ara-D
Bentiu
480
500
520
Sand
Shaly sand
Shale
Chalc

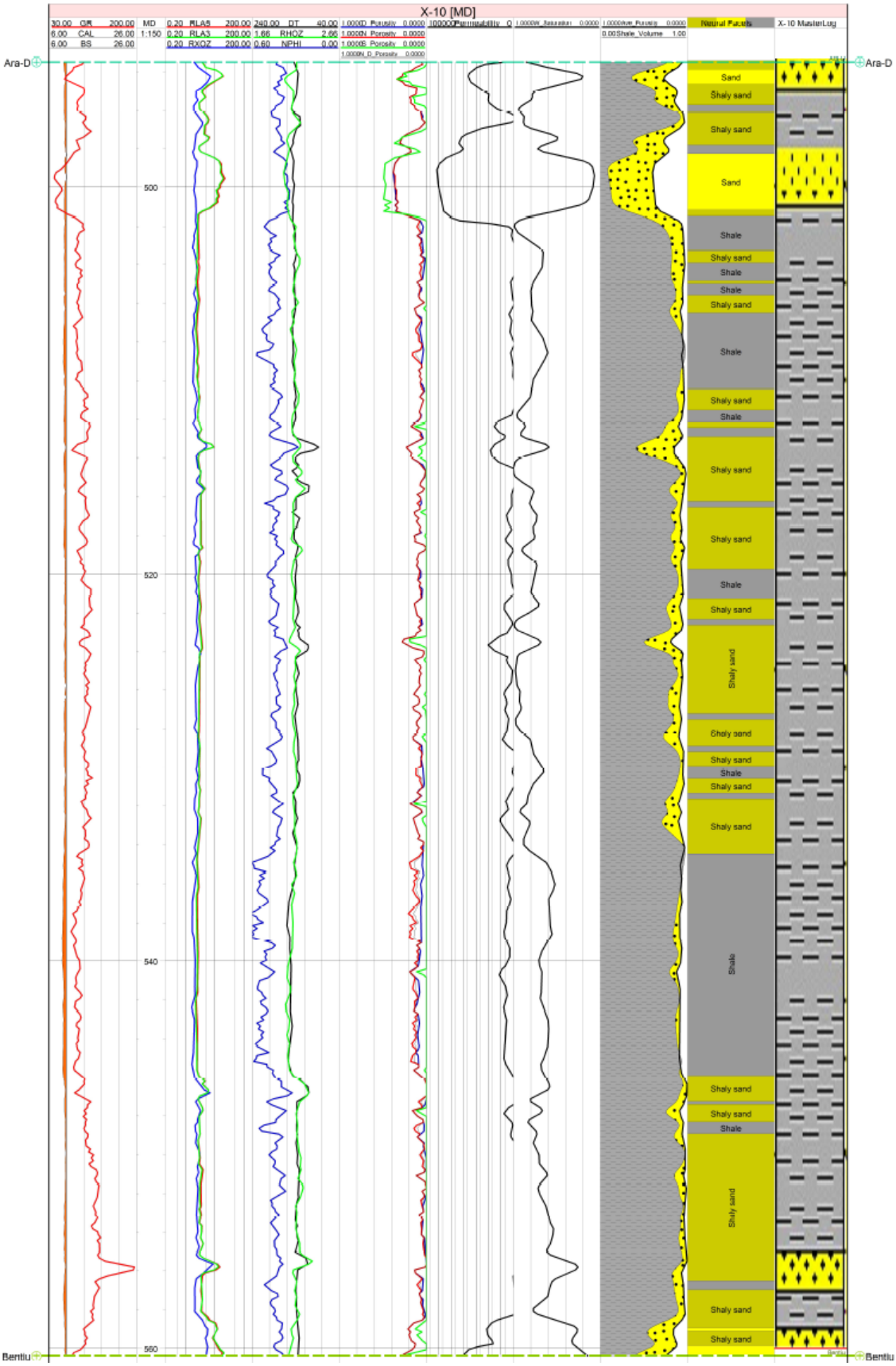
X-10 [MD]
GR
CAL
BS
MD
1:150
RLA5
RLA3
RXOZ
DT
RHOZ
NPHI
Natural Facies
X-10 MasterLog
Ara-D
Bentiu
500
520
540
560
Sand
Shaly sand
Shale

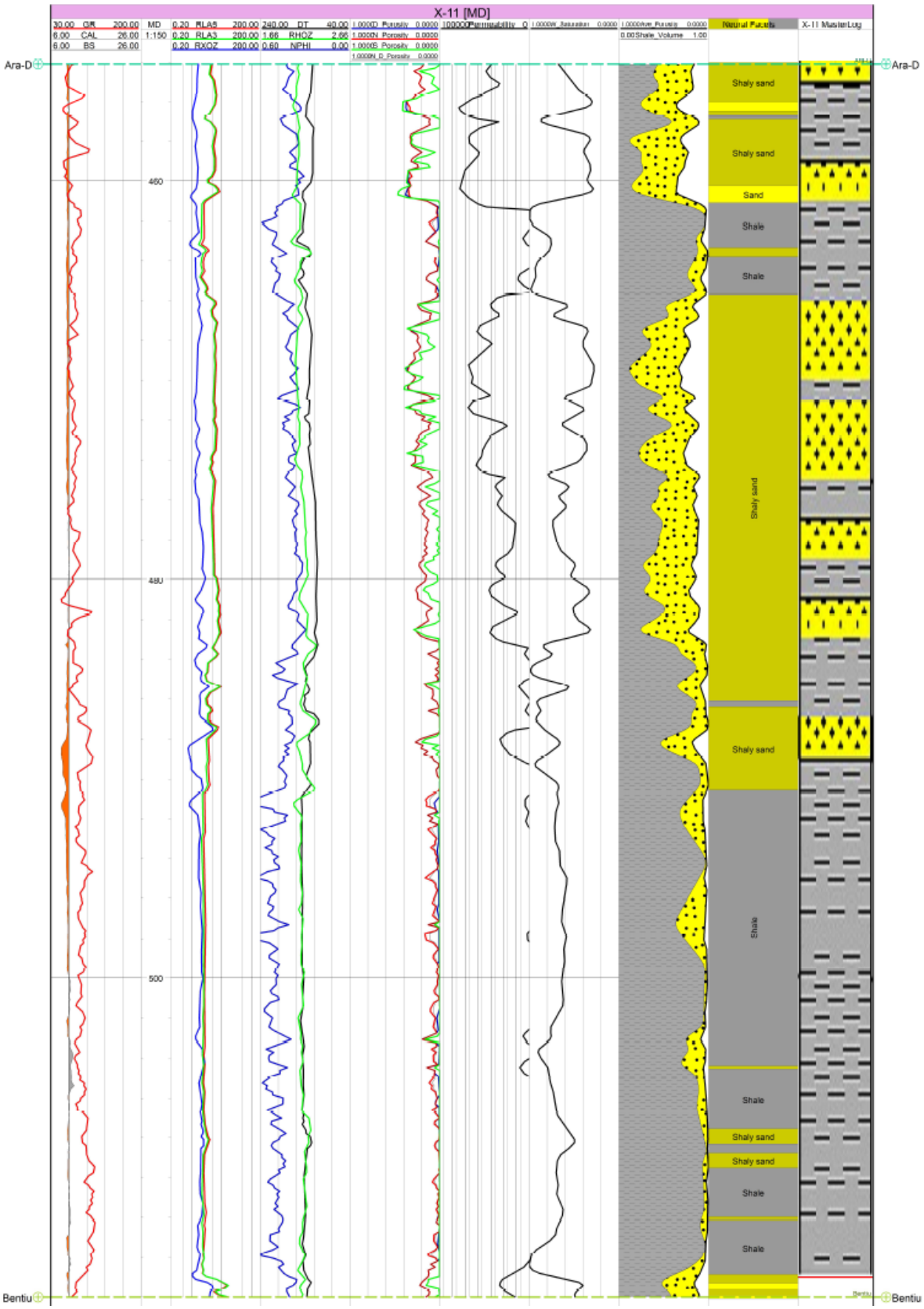
X-11 [MD]
GR
CAL
BS
MD
RLA5
RLA3
RXOZ
DT
RHOZ
NPHI
Natural Facies
X-11 MasterLog
Ara-D
Bentiu
460
480
500
Shaly sand
Shaly sand
Sand
Shale
Shale
Shaly sand
Shaly sand
Shale
Shaly sand
Shaly sand
Shale
Shale

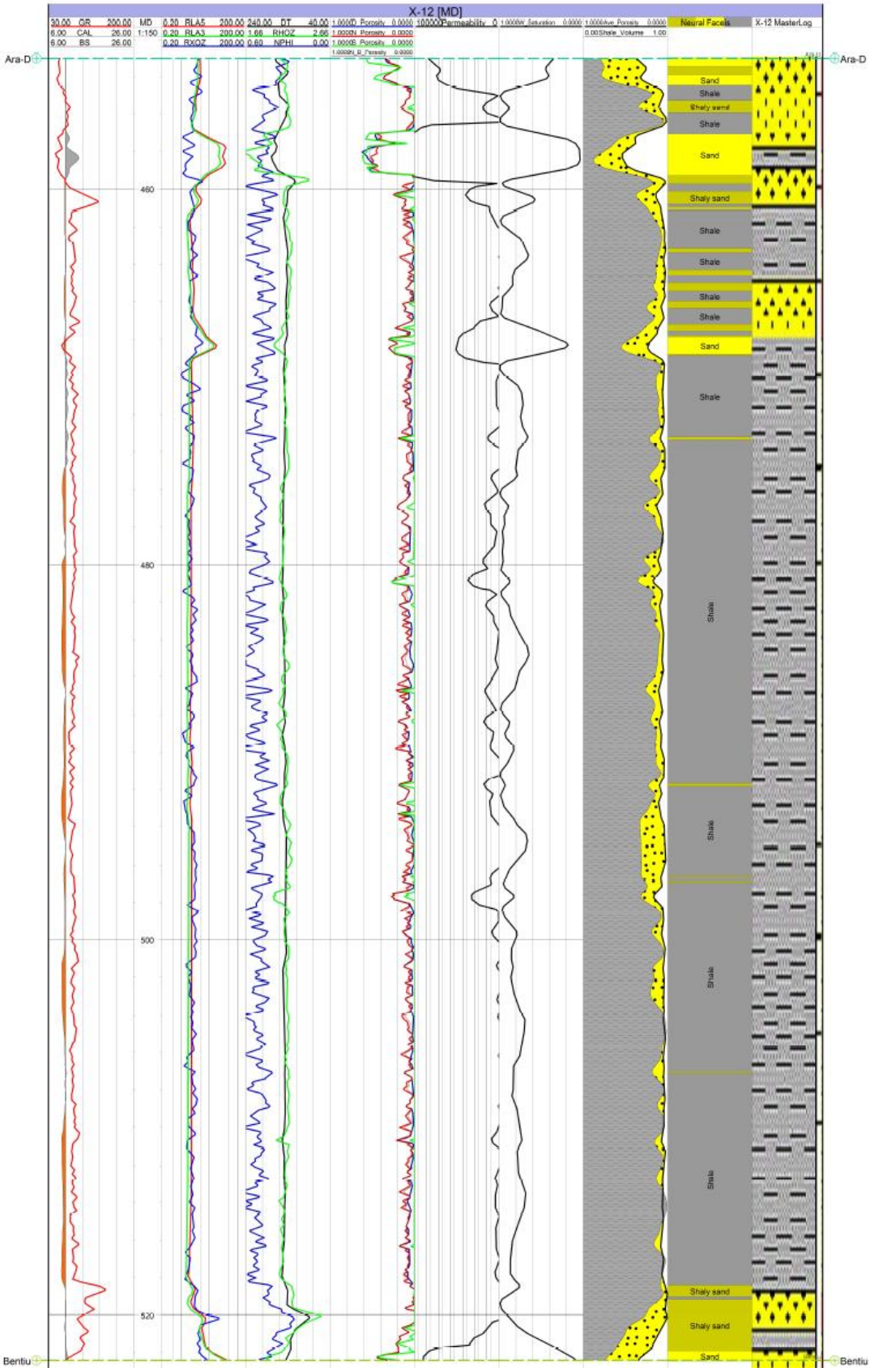
X-12 [MD]
Neural Facels
X-12 MasterLog
Ara-D
Ara-D
Bentiu
Bentiu
Sand
Shale
Shaly sand
Shale
Sand
Shaly sand
Shale
Shale
Shale
Shale
Sand
Shale
Shale
Shale
Shale
Shaly sand
Shaly sand
Sand
460
480
500
520

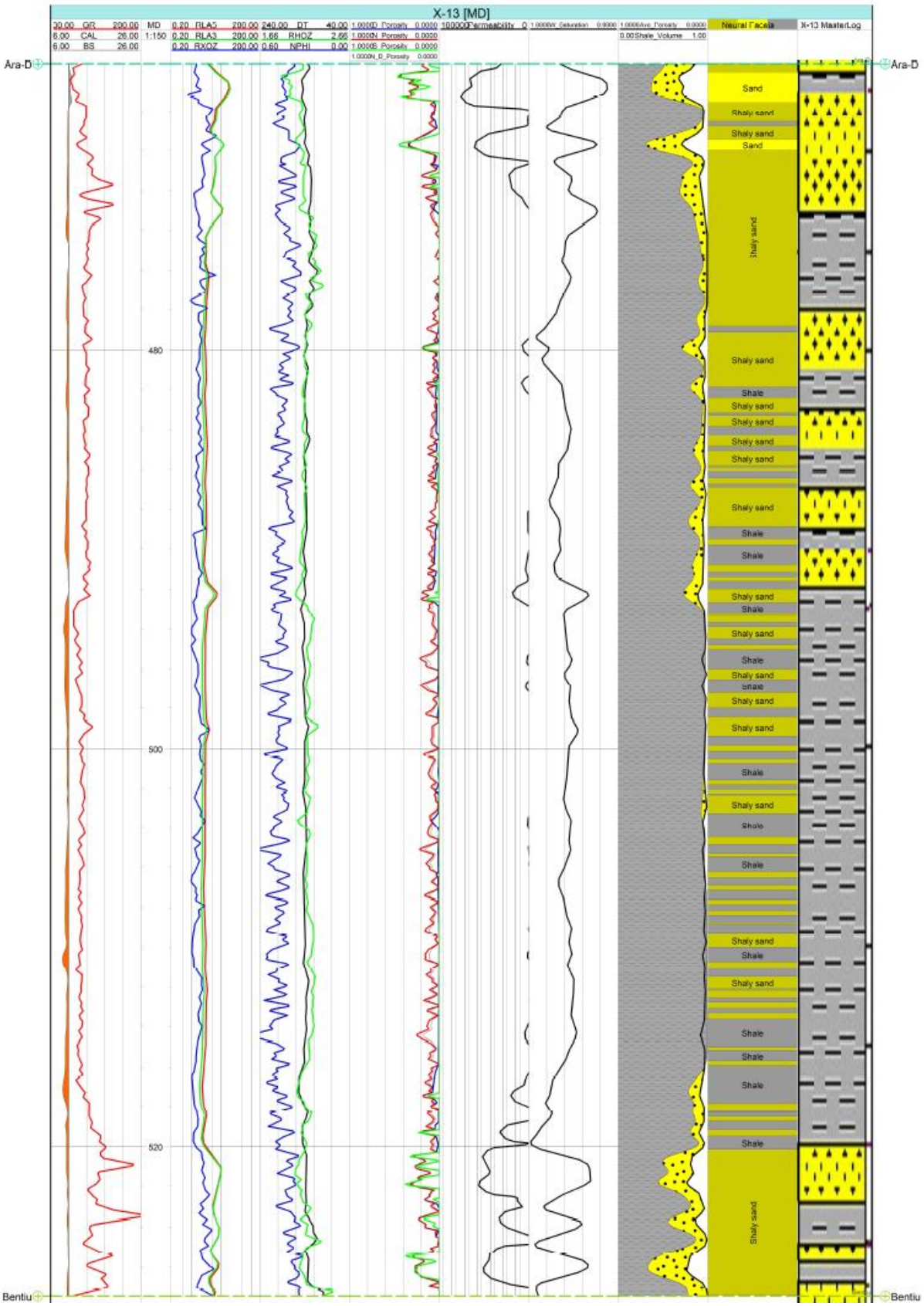
X-13 [MD]
GR 200.00
CAL 26.00
BS 26.00
MD
1:150
RLA5 200.00
RLA3 200.00
RXOZ 200.00
240.00 DT 40.00
1.66 RHOZ 2.66
0.60 NPHI 0.00
Neural Facies
X-13 MasterLog
Ara-D
Bentiu
480
500
520
Sand
Shaly sand
Shale

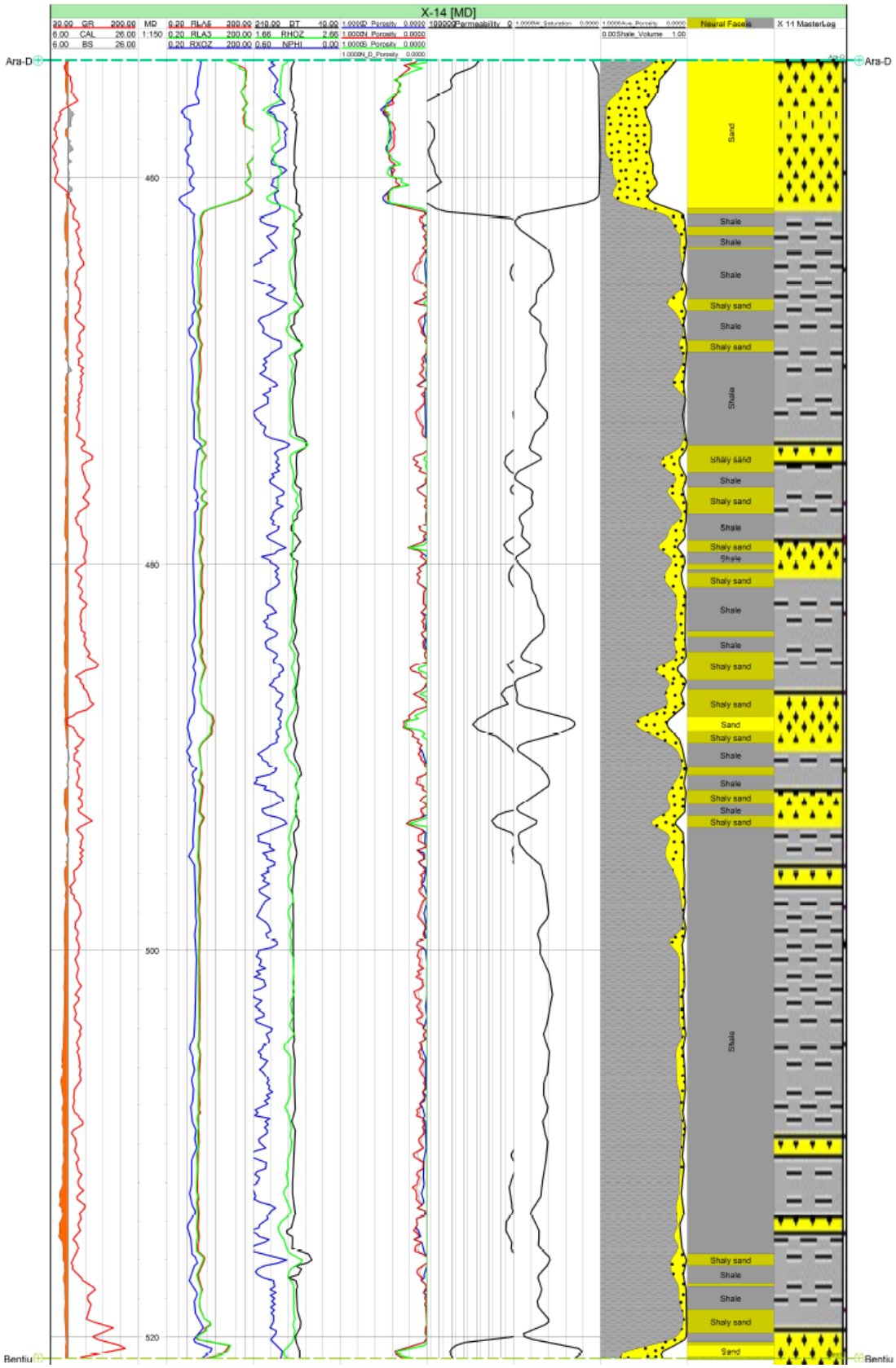
X-14 [MD]
GR
CAL
BS
MD
1:150
RLA5
RLA3
RXOZ
RT
RHOZ
NPHI
Permeability
Neural Facies
X 11 MasterLog
Ara-D
Bentiu
460
480
500
520
Sand
Shale
Shaly sand

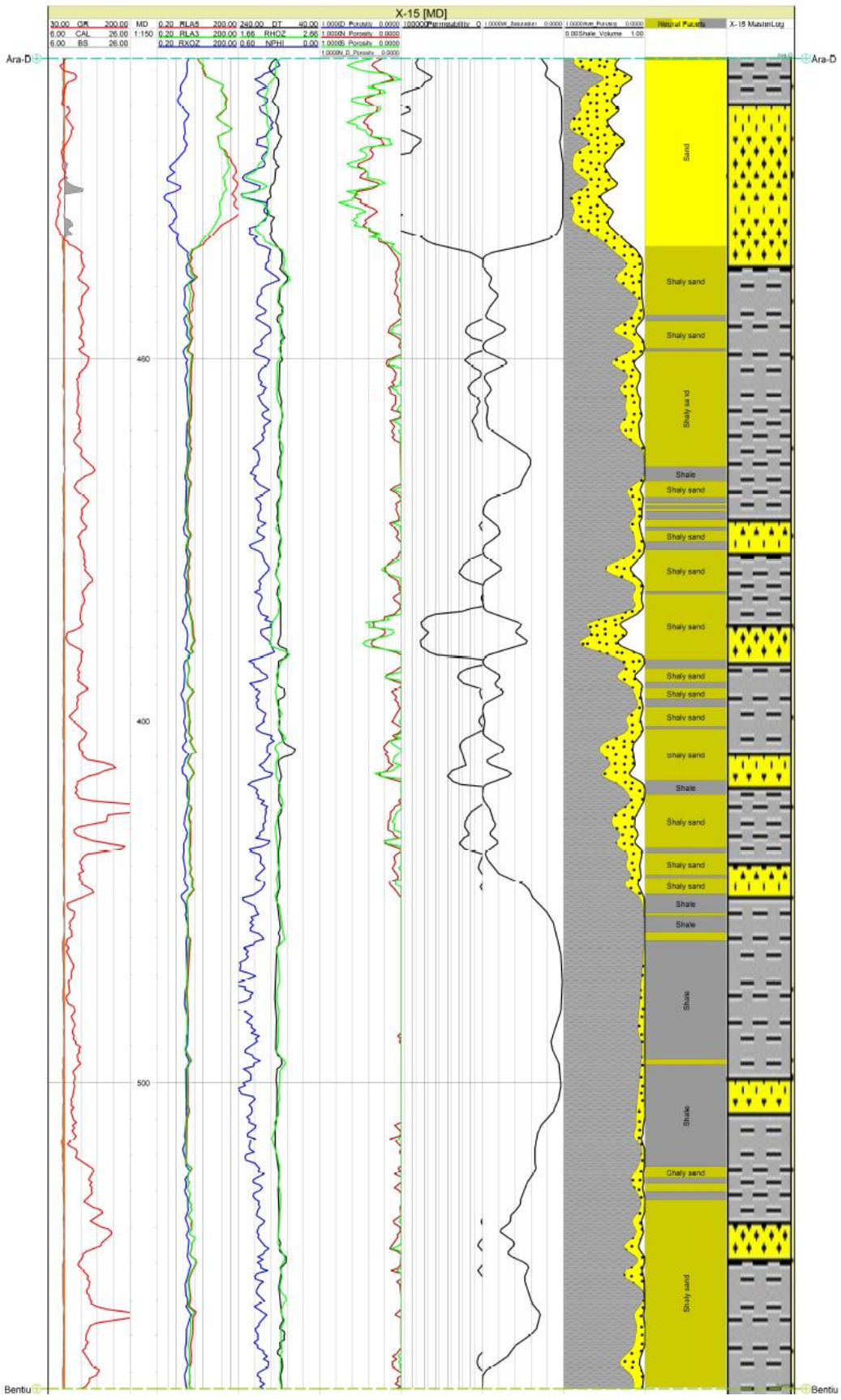
X-15 [MD]
Ara-D
Bentiu
460
400
500
Sand
Shaly sand
Shale
Ghaly sand

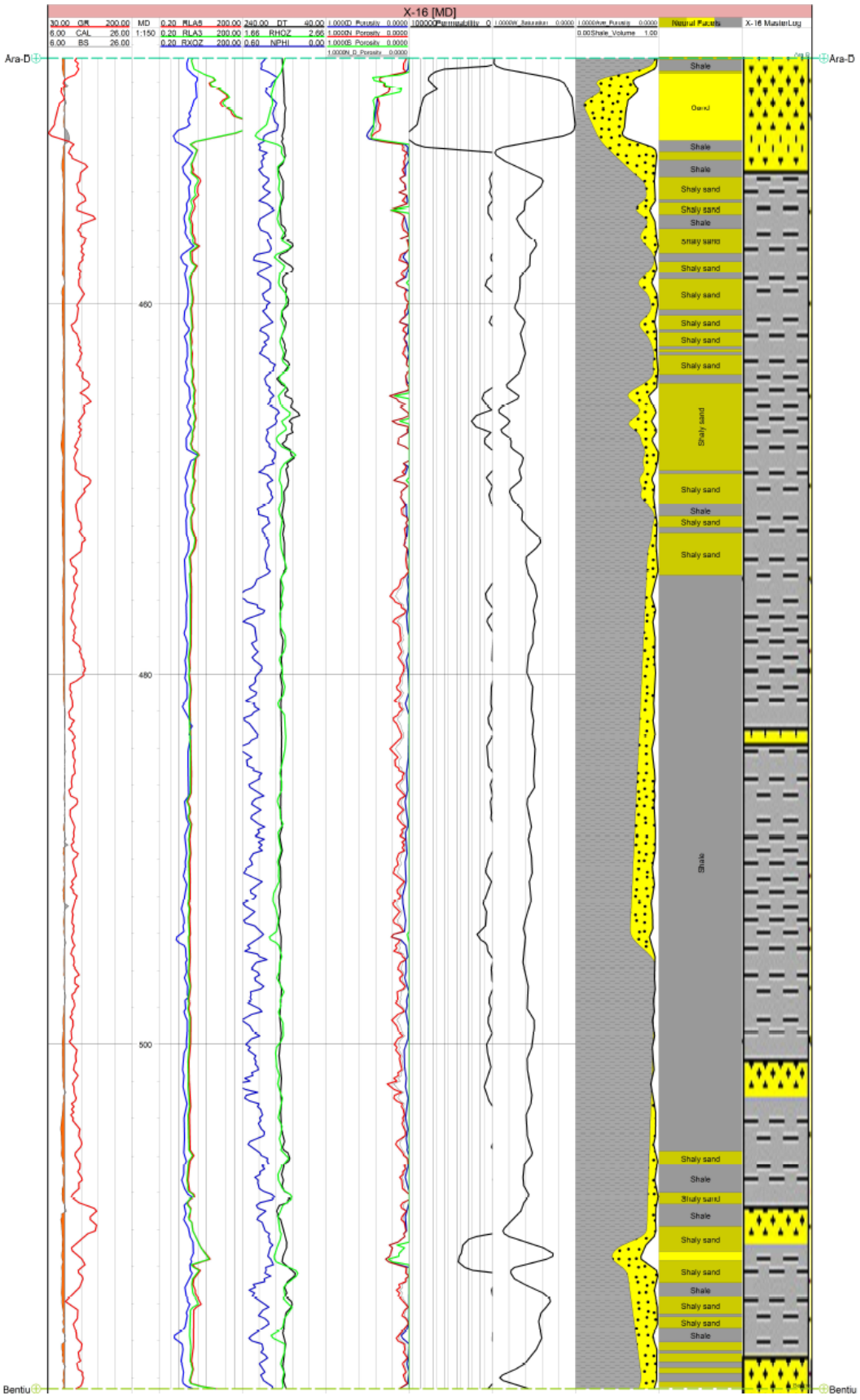
X-16 [MD]
GR
CAL
BS
MD
1:150
RLA5
RLA3
RXOZ
DT
RHOZ
NPHI
Natural Facies
X-16 MasterLog
Ara-D
Bentiu
460
480
500
Shale
Shaly sand
Gresul

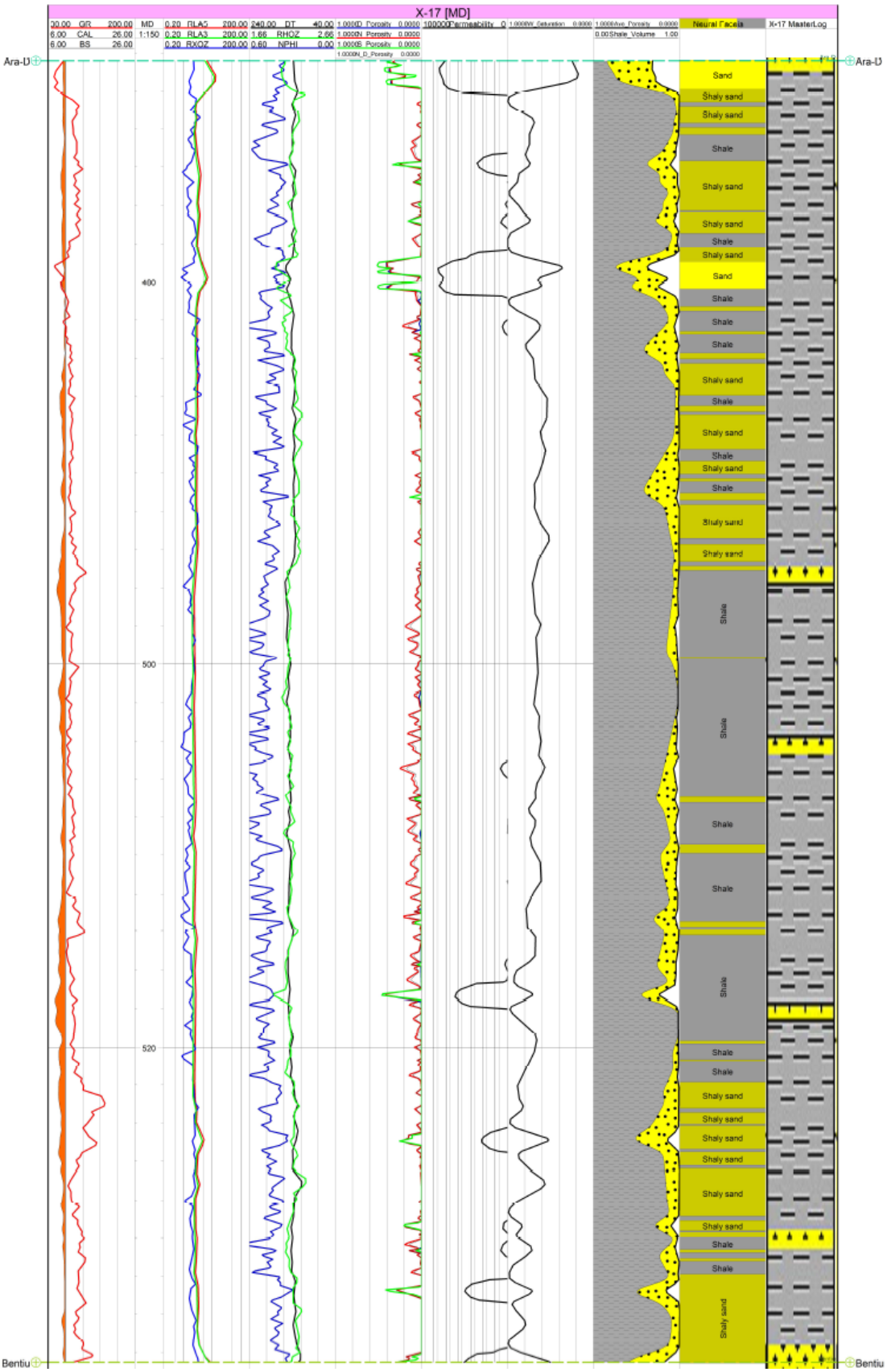
X-17 [MD]
GR 200.00
CAL 26.00
BS 26.00
MD
1:150
RLA5 200.00
RLA3 200.00
RXOZ 200.00
DT 40.00
RHOZ 2.66
NPHI 0.00
Neural Facies
X-17 MasterLog
Ara-U
Bentiu
400
500
520
Sand
Shaly sand
Shale

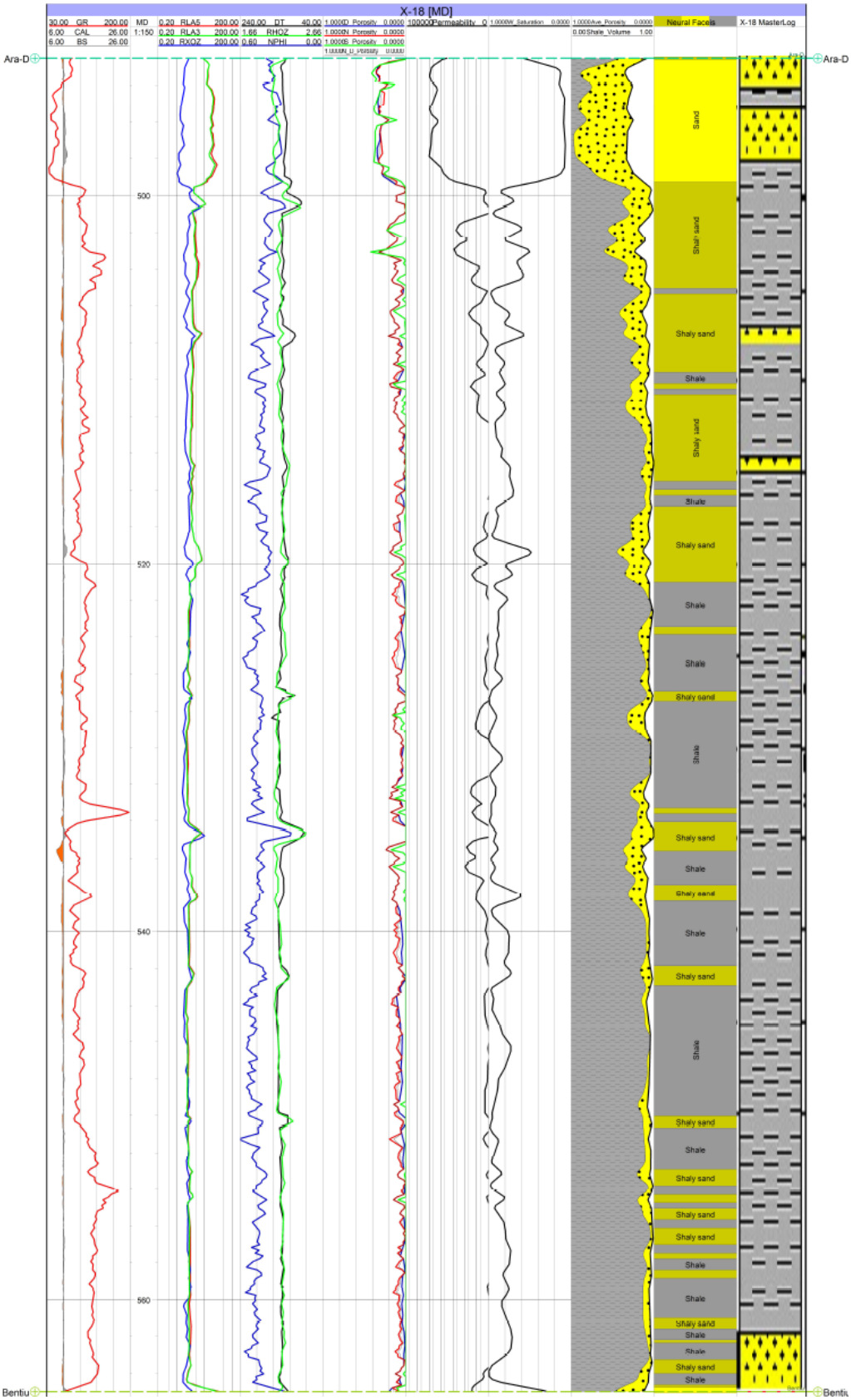
X-18 [MD]
GR
CAL
BS
MD
RLA5
RLA3
RXOZ
DT
RHOZ
NPHI
Permeability
Neural Facies
X-18 MasterLog
Ara-D
Bentiu
500
520
540
560
Sand
Shali sand
Shaly sand
Shale

Seismic and Log Properties Cross-plots

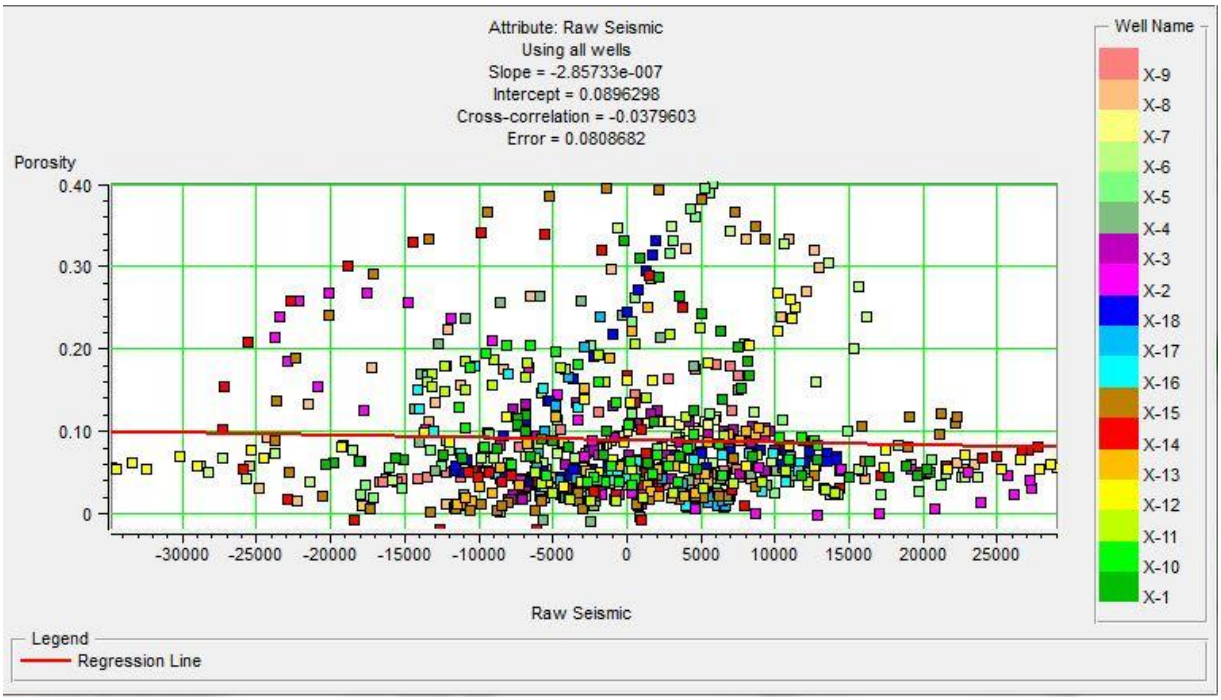
Attribute: Raw Seismic
Using all wells
Slope = -2.85733e-007
Intercept = 0.0896298
Cross-correlation = -0.0379603
Error = 0.0808682
Porosity
0.40
0.30
0.20
0.10
0
-30000 -25000 -20000 -15000 -10000 -5000 0 5000 10000 15000 20000 25000
Raw Seismic
Well Name
X-9
X-8
X-7
X-6
X-5
X-4
X-3
X-2
X-18
X-17
X-16
X-15
X-14
X-13
X-12
X-11
X-10
X-1
Legend
Regression Line

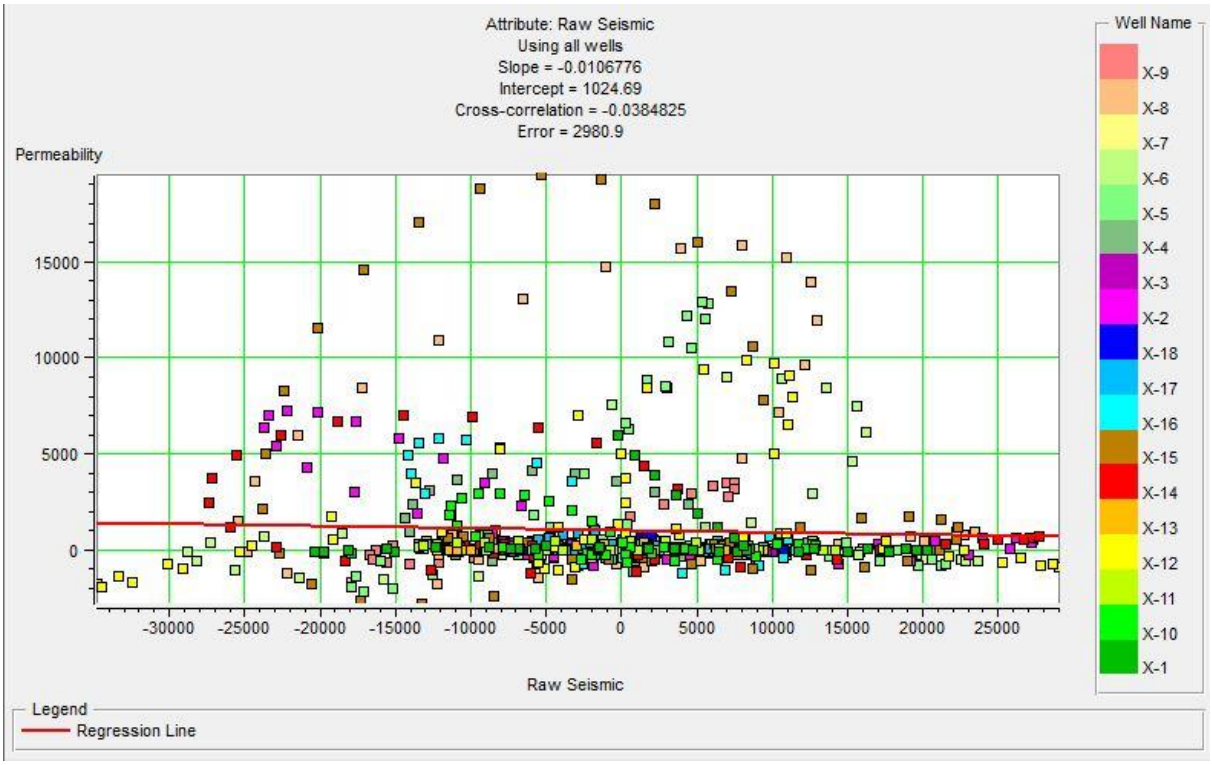
Attribute: Raw Seismic
Using all wells
Slope = -0.0106776
Intercept = 1024.69
Cross-correlation = -0.0384825
Error = 2980.9
Permeability
15000
10000
5000
0
-30000 -25000 -20000 -15000 -10000 -5000 0 5000 10000 15000 20000 25000
Raw Seismic
Well Name
X-9
X-8
X-7
X-6
X-5
X-4
X-3
X-2
X-18
X-17
X-16
X-15
X-14
X-13
X-12
X-11
X-10
X-1
Legend
Regression Line

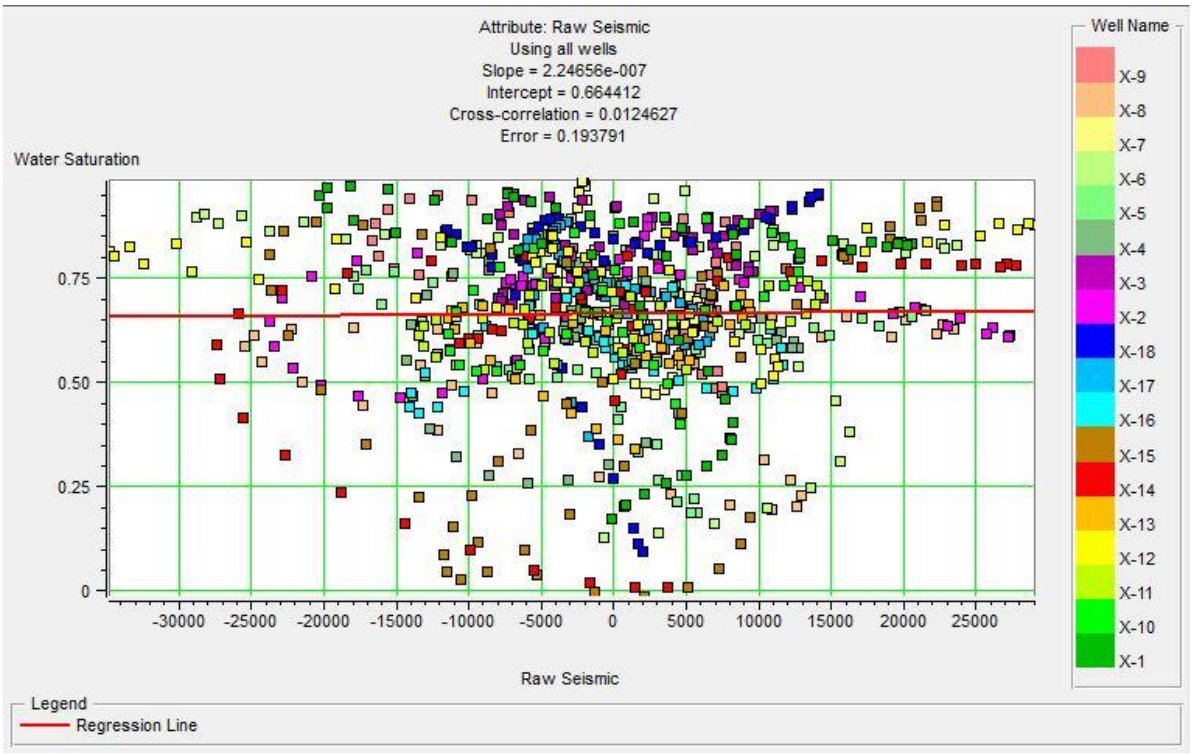
Attribute: Raw Seismic
Using all wells
Slope = 2.24656e-007
Intercept = 0.664412
Cross-correlation = 0.0124627
Error = 0.193791
Water Saturation
0.75
0.50
0.25
0
-30000
-25000
-20000
-15000
-10000
-5000
0
5000
10000
15000
20000
25000
Raw Seismic
Well Name
X-9
X-8
X-7
X-6
X-5
X-4
X-3
X-2
X-18
X-17
X-16
X-15
X-14
X-13
X-12
X-11
X-10
X-1
Legend
Regression Line

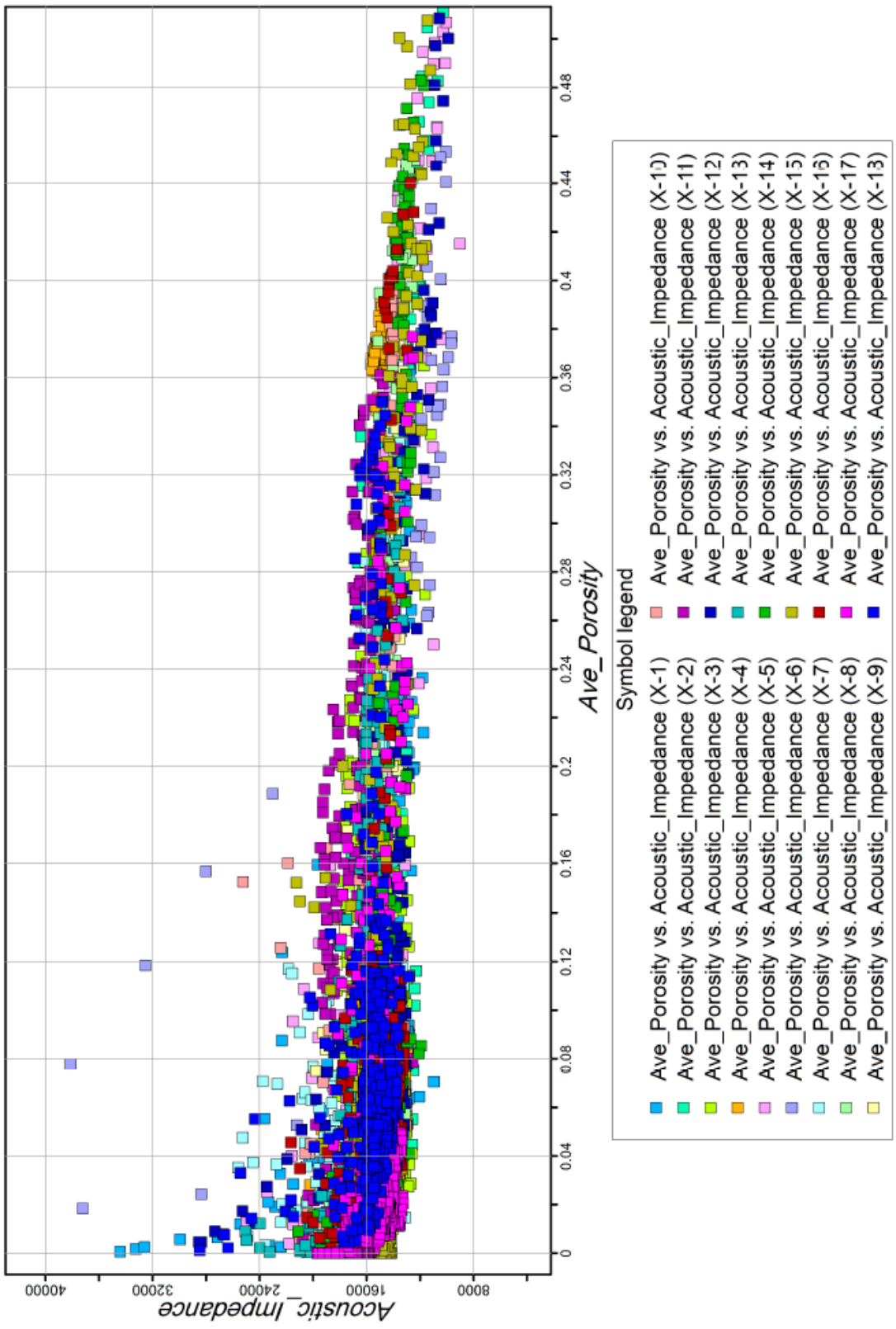
Acoustic_Impedance
8000
16000
24000
32000
40000
Ave_Porosity
0
0.04
0.08
0.12
0.16
0.2
0.24
0.28
0.32
0.36
0.4
0.44
0.48
Symbol legend
Ave_Porosity vs. Acoustic_Impedance (X-1)
Ave_Porosity vs. Acoustic_Impedance (X-2)
Ave_Porosity vs. Acoustic_Impedance (X-3)
Ave_Porosity vs. Acoustic_Impedance (X-4)
Ave_Porosity vs. Acoustic_Impedance (X-5)
Ave_Porosity vs. Acoustic_Impedance (X-6)
Ave_Porosity vs. Acoustic_Impedance (X-7)
Ave_Porosity vs. Acoustic_Impedance (X-8)
Ave_Porosity vs. Acoustic_Impedance (X-9)
Ave_Porosity vs. Acoustic_Impedance (X-10)
Ave_Porosity vs. Acoustic_Impedance (X-11)
Ave_Porosity vs. Acoustic_Impedance (X-12)
Ave_Porosity vs. Acoustic_Impedance (X-13)
Ave_Porosity vs. Acoustic_Impedance (X-14)
Ave_Porosity vs. Acoustic_Impedance (X-15)
Ave_Porosity vs. Acoustic_Impedance (X-16)
Ave_Porosity vs. Acoustic_Impedance (X-17)
Ave_Porosity vs. Acoustic_Impedance (X-18)

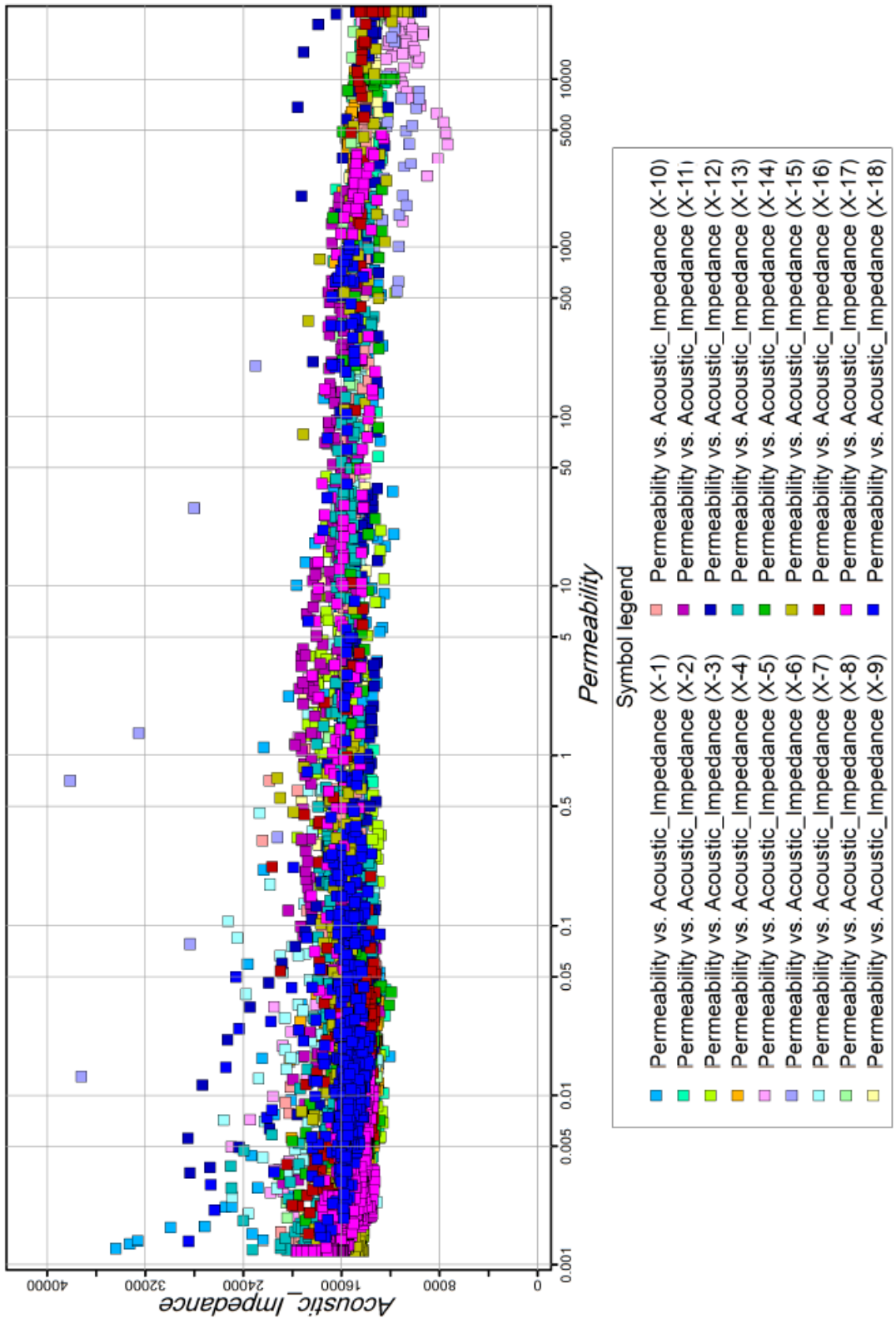
Acoustic_Impedance
0
8000
16000
24000
32000
40000
Permeability
0.001
0.005
0.01
0.05
0.1
0.5
1
5
10
50
100
500
1000
5000
10000
Symbol legend
Permeability vs. Acoustic_Impedance (X-1)
Permeability vs. Acoustic_Impedance (X-2)
Permeability vs. Acoustic_Impedance (X-3)
Permeability vs. Acoustic_Impedance (X-4)
Permeability vs. Acoustic_Impedance (X-5)
Permeability vs. Acoustic_Impedance (X-6)
Permeability vs. Acoustic_Impedance (X-7)
Permeability vs. Acoustic_Impedance (X-8)
Permeability vs. Acoustic_Impedance (X-9)
Permeability vs. Acoustic_Impedance (X-10)
Permeability vs. Acoustic_Impedance (X-11
Permeability vs. Acoustic_Impedance (X-12)
Permeability vs. Acoustic_Impedance (X-13)
Permeability vs. Acoustic_Impedance (X-14)
Permeability vs. Acoustic_Impedance (X-15)
Permeability vs. Acoustic_Impedance (X-16)
Permeability vs. Acoustic_Impedance (X-17)
Permeability vs. Acoustic_Impedance (X-18)

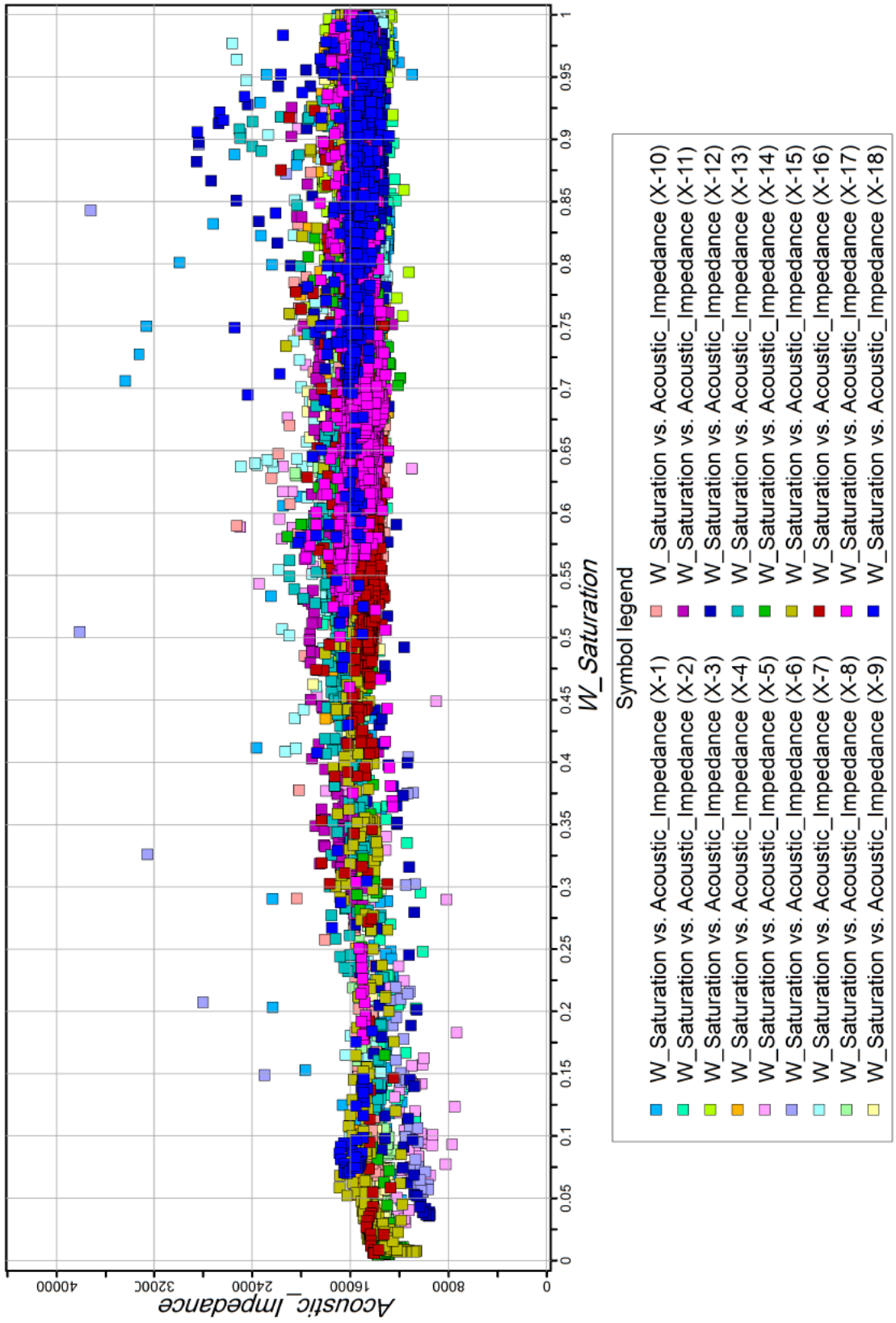
Acoustic_Impedance
W_Saturation
0
8000
16000
24000
32000
40000
0
0.05
0.1
0.15
0.2
0.25
0.3
0.35
0.4
0.45
0.5
0.55
0.6
0.65
0.7
0.75
0.8
0.85
0.9
0.95
1
Symbol legend
W_Saturation vs. Acoustic_Impedance (X-1)
W_Saturation vs. Acoustic_Impedance (X-2)
W_Saturation vs. Acoustic_Impedance (X-3)
W_Saturation vs. Acoustic_Impedance (X-4)
W_Saturation vs. Acoustic_Impedance (X-5)
W_Saturation vs. Acoustic_Impedance (X-6)
W_Saturation vs. Acoustic_Impedance (X-7)
W_Saturation vs. Acoustic_Impedance (X-8)
W_Saturation vs. Acoustic_Impedance (X-9)
W_Saturation vs. Acoustic_Impedance (X-10)
W_Saturation vs. Acoustic_Impedance (X-11)
W_Saturation vs. Acoustic_Impedance (X-12)
W_Saturation vs. Acoustic_Impedance (X-13)
W_Saturation vs. Acoustic_Impedance (X-14)
W_Saturation vs. Acoustic_Impedance (X-15)
W_Saturation vs. Acoustic_Impedance (X-16)
W_Saturation vs. Acoustic_Impedance (X-17)
W_Saturation vs. Acoustic_Impedance (X-18)

Vitae

Name : Migdad EL-Kheir Shuaib

Nationality : Sudanese

Date of Birth : September 1986

Email : migdadshuaib@yahoo.com

Address : University of Khartoum- Geology Department

P.O. Box 321 Khartoum- Sudan

Mobile: +249 9 12183139

Academic Background :

- B.Sc. (Honors- First Class) from University of Khartoum, Faculty of Science, Department of Geology (November, 2008).
- M.Sc. from King Fahd University of Petroleum and Minerals, College of Science, Earth Sciences Department (May, 2013).

Work Experience :

- Teaching Assistant - University of Khartoum, Khartoum-Sudan (January 2009 – February 2011)
- Research Assistant – King Fahd University of Petroleum and Minerals, Dhahran-Saudi Arabia (February 2011- May 2013)